

ASD TDR 63-754
Part II

AS
P2

AD612958

MOLECULAR FLOW AND THE EFFUSION PROCESS IN THE
MEASUREMENT OF VAPOR PRESSURES

TECHNICAL DOCUMENTARY REPORT NO. ASD TDR 63-754,
Part II. Additional Data and Details of Equipment

Robert D. Freeman
Oklahoma State University

January 1965

COPY	2	OF	3	116-5P
HARD COPY				\$ 4.00
MICROFILME				\$ 0.75

Air Force Materials Laboratory
Research and Technology Division
Air Force Systems Command
Wright-Patterson Air Force Base, Ohio

ARCHIVE COPY

20040702014

No DDC limits

ASD TDR 63-754
Part II

MOLECULAR FLOW AND THE EFFUSION PROCESS IN THE
MEASUREMENT OF VAPOR PRESSURES

TECHNICAL DOCUMENTARY REPORT NO. ASD TDR 63-754
Part II. Additional Data and Details of Equipment

Robert D. Freeman
Oklahoma State University

January 1965

Air Force Materials Laboratory
Research and Technology Division
Air Force Systems Command
Wright-Patterson Air Force Base, Ohio

4105050P006

NOTICES

When Government drawings, specifications, or other data are used for any purpose other than in connection with a definitely related Government procurement operation, the United States Government thereby incurs no responsibility nor any obligation whatsoever; and the fact that the Government may have formulated, furnished, or in any way supplied the said drawings, specifications, or other data, is not to be regarded by implication or otherwise as in any manner licensing the holder or any other person or corporation, or conveying any rights or permission to manufacture, use, or sell any patented invention that may in any way be related thereto.

Qualified requesters may obtain copies of this report from the Defense Documentation Center (DDC), (formerly ASTIA), Cameron Station, Bldg. 5, 1010 Duke Street, Alexandria 4, Virginia.

This report has been released to the Office of Technical Services, U. S. Department of Commerce, Washington 25, D. C., for sale to the general public.

Copies of this report should not be returned to the Research and Technology Division unless return is required by security considerations, contractual obligations, or notice on a specific document.

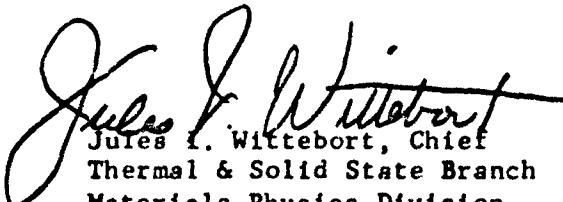
FOREWORD

This report was prepared by the Research Foundation and the Department of Chemistry, Oklahoma State University, Stillwater, Oklahoma, under USAF Contract AF33(657)-8767. This contract was initiated under Project No. 7360, "The Chemistry and Physics of Materials," Task No. 736004, "Physical Properties of Materials." The work was administered under the direction of the AF Materials Laboratory, Research and Technology Division, with Mr. Paul W. Dimiduk, MAYT, as project engineer.

This report is an account of the research accomplished between 1 June 1963 and 31 August 1964.

The author wishes to acknowledge the many contributions of the graduate students who have been associated with this research program, and who should be credited with co-authorship of the various sections. They are J. E. Bennett (section V), J. G. Edwards (sections II and III), and Ruth C. Erbar (sections III and IV). The excellent craftsmanship of the machinists and instrument makers in our departmental Machine and Instrument Shop has been invaluable and is gratefully acknowledged.

This technical documentary report has been reviewed and is approved.


Jules I. Wittebort, Chief
Thermal & Solid State Branch
Materials Physics Division
AF Materials Laboratory

ABSTRACT

Details are given for molecular beam apparatus for the measurement of the angular distribution of molecules effusing from non-ideal orifices. Some results obtained for a cylindrical orifice with length/radius = 2.42 are in fair agreement with the theoretical analysis.

The vacuum microbalance and furnace which are used in the microbalance-inverted Knudsen effusion-recoil (Miker) technique for determining vapor pressures and molecular weights are described in detail. Miker results for the vapor pressure of silver, gold, and calcium fluoride are in good agreement with values published by other workers. Some data on the diffusion of silver and gold vapors through graphite cell walls resulted as a by-product of these studies. Values obtained for the molecular weights of tin and calcium fluoride vapors are somewhat ambiguous, but do indicate that improvements in the technique are still possible and necessary.

An analysis of the rate of effusion from a cooling Knudsen effusion cell is given.

The complete details of an analysis and computation of transmission probabilities, angular distribution functions, and recoil force corrections for conical and cylindrical orifices are now available.

TABLE OF CONTENTS

Section	Page
I. INTRODUCTION	1
II. THEORETICAL ANALYSIS OF MOLECULAR FLOW THROUGH CONICAL ORIFICES	1
III. EXPERIMENTAL APPARATUS FOR MEASUREMENT OF ANGULAR DISTRIBUTION OF MOLECULAR FLOW THROUGH CONICAL ORIFICES	2
A. The Main Vacuum Chamber	3
B. The Gas Reservoir	8
C. The Buffer Chamber	9
D. The Detector Chamber	13
E. The Detector Electronics	18
IV. PRELIMINARY RESULTS OF MEASUREMENT OF ANGULAR DISTRIBUTION OF MOLECULAR FLOW THROUGH CONICAL ORIFICES	23
A. Results of Preliminary Tests	23
B. Preliminary Results for a Cylindrical Orifice	24
V. THE MULTICELL TECHNIQUE FOR EXPERIMENTAL DETERMINATION OF TRANSMISSION PROBABILITIES FOR MOLECULAR FLOW THROUGH CONICAL ORIFICES	30
VI. THE MIKER TECHNIQUE	31
A. Description of the Technique	31
B. Design and Construction of the Apparatus	34
C. Experimental Results	55
D. Rate of Effusion from a Cooling Knudsen Cell	87
REFERENCES	97

LIST OF TABLES

Table	Page
1. Experimental Data for Angular Distribution of Molecular Flow through a Cylindrical Orifice with $\underline{L/r} = 2.42$	25
2. Calibration Data For Microbalance	58
3. Parameters of Miker Cells	63
4. Permeation of Closed Graphite Cells by Gold and Silver Vapors	70
5. Experimental Cooling Data for A Typical Miker Cell	75
6. Vapor Pressure of Silver from Rate of Effusion	76
7. Vapor Pressure of Calcium Fluoride from Rate of Effusion	77
8. Vapor Pressure of Gold from Rate of Effusion	78
9. Heat of Sublimation of Silver from Rate of Effusion	82
10. Heat of Sublimation of Gold from Rate of Effusion	83
11. Vapor Pressure and Recoil Force Data for Tin	85
12. Vapor Pressure and Recoil Force Data for Calcium Fluoride	86
13. Identification of Major Commercial Components of Apparatus	94

LIST OF ILLUSTRATIONS

Figure	Page
1. Diagram of the Experimental Apparatus	4
2. The Rotating Cell	6
3. Orifice Plate Assembly	7
4. Tubulation Connector Between the Gas Reservoir and the Main Vacuum Chamber	10
5. The Chopper Assembly	12
6. The Second Collimating Orifice	15
7. The Molecular Beam Ionizer	16
8. Power Supply for Beam Ionizer	19
9. Schematic of Amplification System	19
10. The Preamplifier	21
11. Angular Distribution Data	26
12. Comparison of the Experimental Results of Adams and the Theoretical Results from This Work for the Angular Distribution of Molecules Effusing from a Conical Orifice with $\underline{T} = 15.93^{\circ}$ and $\underline{L/r_m} = 58.8$	28
13. Schematic Representation of Apparatus for Miker Technique	32
14. The Effect on the Recoil Mass of Effusion which Occurs During the Cooling Period	35
15. The Vacuum Microbalance, VMB-1	37
16. The Base Assembly for Supporting, Leveling, and Providing Kinematic Alignment of the Microbalance	39
17. Diagram Illustrating the Simple Theory of the Equal-Arm Balance	41

Figure	Page
18. Photopot in Unipolar Circuit	45
19. Photopot in Bipolar Circuit	46
20. Automatic Control System (Diagrammatic)	48
21. Schematic Diagram of Control System	49
22. The Miker Cell	50
23. The Heating Element	51
24. The Vacuum System	53
25. Prism Arrangement for Pyrometric Sightings into the Miker Cell Orifice	56
26. Microbalance Calibration Curve	59
27. Typical Experimental Data-Calcium Fluoride, Run 9	65
28. Rapid Effusion - Silver, Run 14	66
29. The Effect of Diminishing Sample-Surface-Area on the Rate of Effusion	68
30. Normal Effusion and Closed-Cell Permeation, Silver	72
31. Normal Effusion and Closed-Cell Permeation, Gold	73
32. Vapor Pressure of Silver	79
33. Vapor Pressure of Calcium Fluoride	80
34. Vapor Pressure of Gold	81

LIST OF SYMBOLS

A	constant.
a	area of orifice; see also figure 17.
a'	equivalent-area parameter in capillary effusion.
B	slope of Clausius-Clapeyron plot: $\ln P = C - (B/T)$.
b	arm-length of balance beam.
c	constant.
$dN_{\theta}(L)$	number of molecules which flow, per second, from an orifice into the incremental solid angle between θ and $\theta + d\theta$.
dN_{ω}	number of molecules which pass per second from an orifice into the incremental solid angle $d\omega$ located at angle θ from the orifice axis.
$d\omega$	incremental solid angle.
F	Gibbs free energy; recoil force.
f	recoil-force correction factor.
f_{ef}	free energy function, $(F_T^0 - H_{298}^0)/T$.
$f(T)$	function of temperature.
G	transmission probability of orifice; mass of balance beam.
g	gravitational acceleration.
$g(t)$	function of time.
H	enthalpy.
I	electrical current.
I_B	moment of inertia of balance beam.
$I(\theta)$	experimental angular intensity of molecular beam, proportional to N_d .
k_r, k_c	cooling constants: radiation, conduction.
L	axial length of orifice.
M_K	molar mass of effusing vapor.
M_K^*	average molar mass of effusing vapor.
m	actual recoil mass; mass of calibrating weights.
m_c	mass which effuses from a Miker cell during cooling.
m_i	ideal recoil mass.
N_d	number of molecules which enter the molecular beam detector orifice per second.
P	actual pressure within effusion cell.

P_K	pressure measured by Knudsen method.
P_R	pressure determined by recoil force measurement.
$P(\theta)$	fraction of effusing molecules, per steradian, which strike detector at angle θ .
Q	balance load; also used to represent a group of terms in Section VI. D.
Q_N	complicated function of orifice parameters; discussed and derived in Part I ¹⁴ .
R	gas constant.
r	radius of orifice; r_m , minimum radius.
s	see Figure 17.
T	absolute temperature.
t	time, usually seconds.
u	parameter in Section VI.D.; $u = (2B/T)^{1/2}$.
W	transmission probability of orifice.
w	mass of vapor which effuses.
\dot{w}	rate of effusion (mass/sec).
x	coordinate; incremental load on balance.
θ	angle measured from the axis of an orifice; angular deflection of balance beam.
$\theta(v)$	$(2\pi)^{-1/2} e^{-v^2/2}$.
μ	micron.
μ_0	incident molecular density (molecules per cm^2 per sec) in reservoir from which effusion occurs.
μg	microgram.
ρ	density.
τ	period of oscillation of balance.
$\phi(v)$	$(2/\pi)^{1/2} \varphi(v)$.
$\varphi(v)$	represents the normal probability function (equation 22).
w	mass fraction.

SECTION I

INTRODUCTION

The Knudsen effusion technique^{27,28} is widely used, in varied guises, to obtain vapor and/or dissociation pressure data, especially at high temperatures. In actual laboratory operation the conditions under which effusion occurs are rarely, if ever, the ideal conditions assumed in the derivation of the simple Knudsen equation. This report summarizes work on several approaches designed to clarify the understanding of the effusion process under non-ideal conditions. More detailed introductory paragraphs are included in each of the following sections.

SECTION II

THEORETICAL ANALYSIS OF MOLECULAR FLOW THROUGH CONICAL ORIFICES

In Part I of this report¹⁴ we discussed in some detail our analysis of molecular flow through the completely general conical orifice. An even more detailed discussion (including computer program) of the analysis and of the implications of the results is now available in Edwards' thesis¹¹ which is incorporated by reference in this report.

Manuscript released by author August 1964 for publication as an ASD
Technical Documentary Report.

SECTION III

EXPERIMENTAL APPARATUS FOR MEASUREMENT OF ANGULAR DISTRIBUTION OF MOLECULAR FLOW THROUGH CONICAL ORIFICES

Of the various quantities which are derived in the theoretical analysis (see Section II) and which are amenable to experimental study, the most critical is the angular distribution of molecules effusing from an orifice, i. e., the variation with θ of the number dN_ω of molecules which pass per second from the orifice into the incremental solid angle $d\omega$ located at angle θ from the orifice axis. The theoretical analysis predicts that dN_ω is proportional to $Q_N \cos \theta$; Q_N is the complicated function of orifice parameters which arises from the non-ideality of the orifice (for the ideal orifice, Q_N is always unity). Measurement of dN_ω or an equivalent quantity would provide experimental data which could be compared directly with theoretical values for $Q_N \cos \theta$.

To accomplish these measurements the apparatus described in this section (and briefly in Part I¹⁴) has been constructed. It is designed to allow a study of the effusion of a permanent gas (e.g., N_2 , He, CO_2) at any suitable pressure from any orifice with a geometry which can be machined into a small circular plate. Permanent gases are used as effusants so that the apparatus can be operated at room temperature; concern that the reservoir-orifice system may not be isothermal is thereby minimized. For this advantage the ability to study the effusion process as a function of temperature is sacrificed.

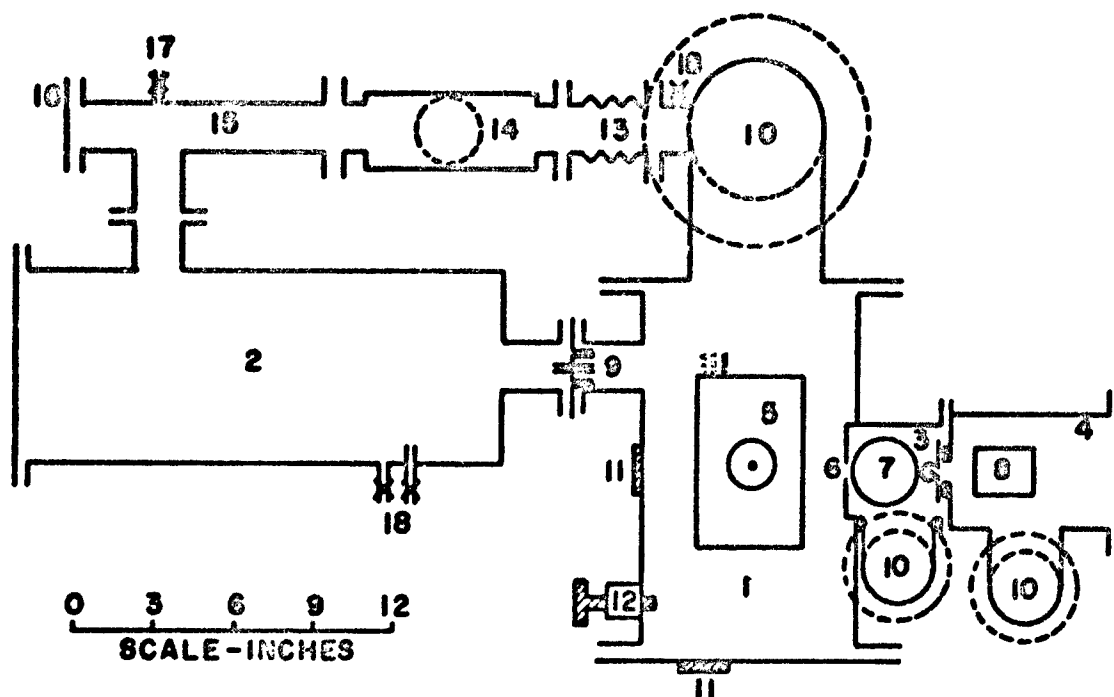
The angular distribution of effusing molecules is determined by a molecular beam method³³ incorporating a modulated beam technique¹³. The reservoir from which the molecules effuse can be rotated on an axis which passes through, and is parallel to, the outer face of the orifice under study. Two stationary collimating orifices and the effusion orifice under study define a molecular beam, the beam is modulated by a mechanical chopper, and its intensity is determined by a neutral-beam detector.

The apparatus, a diagrammatic horizontal cross-section of which is shown in Figure 1, consists of five principal components: (A) The Main Vacuum Chamber, which can be maintained at a pressure very low with respect to the pressure in the gas reservoir, and which contains the rotating effusion cell; (B) The Gas Reservoir, a large chamber from which gas flows to the effusion cell and in which the pressure can be kept constant; (C) The Buffer Chamber, a small independently-pumped chamber which is separated from the main chamber by a plate containing the first collimating orifice, and which contains a chopper capable of interrupting the beam about one hundred times per second; (D) The Detector Chamber, an independently-pumped volume which is separated from the buffer chamber by a plate containing the second collimating orifice, and which contains an electron-impact molecular beam detector; (E) The Detector Electronics, which consists of a power supply for the beam ionizer and a system to amplify the ion current from the ion collector.

A. THE MAIN VACUUM CHAMBER

1. The Vacuum Envelope: The vacuum envelope is constructed from a cold-rolled seamless steel pipe, 12 in. long, with 7.5-in. i.d. and 0.25-in. wall thickness. On each end of the pipe is a 0.25-in. steel flange; matching steel endplates cover these flanges; the vacuum seal is made with the usual neoprene O-rings. Two Condulet vacuum ports are provided for introducing vacuum-gauge tubes into the system. This chamber is supported with the longitudinal axis of the pipe in the horizontal plane.

2. The Pumping System: To one endplate of the main chamber is welded a 5-in.-i.d. steel tee. A PMC-720 diffusion pump is connected to the lower end of this tee by an appropriate flange; an identical flange at the top of the tee accommodates either a blank-off plate or a liquid nitrogen trap. The PMC-720 pump is backed by a MB-100 diffusion pump; this booster pump is necessary to handle the large gas through-put which occurs during an effusion experiment. Both pumps are charged with Octoil pump fluid.



1. The Main Vacuum Chamber
2. The Gas Reservoir
3. The Buffer Chamber
4. The Detector Chamber
5. The Rotating Effusion Cell
6. The Beam Collimating Orifices
7. The Beam Chopper
8. The Beam Ionizer
9. Connectors for Tygon Tubulation Which Carries Gas from the Reservoir to the Rotating Cell
10. Pumping "T"s Which Accommodate Liquid Nitrogen Traps
11. Glass Windowe
12. Rotary Vacuum Seal Through Which the Cell is Rotated
13. Brass Bellows
14. Globe Valve
15. Copper Pipe, $1\frac{1}{2}$ -in. Diameter
16. Port for Attaching 45-Liter Stainless Steel Tank
17. Valve for Introducing Effusant Gas
18. Connections to the Equibar Pressure Meter

Figure 1. Diagram of the Experimental Apparatus

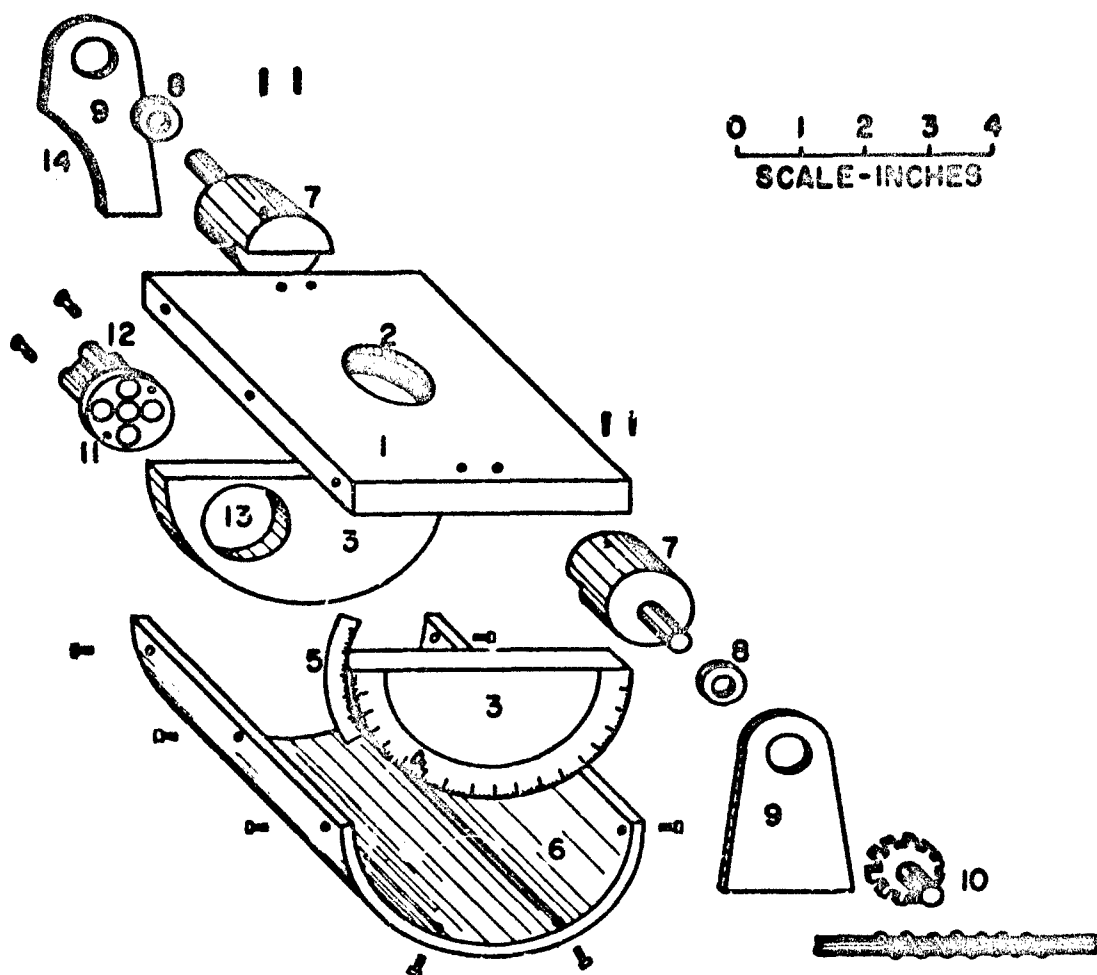
The two pumps are connected by a "U" made from 2.5-in. copper pipe fittings and appropriate flanges. The MB-100 pump also provides fore-vacuum for other diffusion pumps in the system through connections soldered into the "U". The pressure in the "U" is monitored with a DV-6 thermocouple vacuum gauge.

The MB-100 pump is connected by a short section of rubber vacuum hose to a Welch 1402-B mechanical pump.

The vacuum envelope and the buffer chamber (described subsequently) which is welded to it, the pumping tee, and both main chamber endplates are nickel-plated.

3. The Effusion Cell: An exploded view of the effusion cell is given in Figure 2. The cell is a hemicylinder with 2-in. radius and 4-in. length. The ends of the hemicylinder are two brass semi-circles, the flat face is a 4 x 4 x 0.5-in. steel plate, and the curved portion of the hemicylinder is from a Plexiglas pipe with 4-in. o.d. and 0.25-in. wall thickness. The brass ends are attached to the steel face with epoxy adhesive. The Plexiglas and metal sections are held together by screws; a gas-tight seal is provided by a gasket made of lengths of Scotch plastic electrical tape. The gasket is lubricated with Celvacene "heavy" grease; an extra-thick layer is applied at the joints between two strips of tape.

A 1.0-in.-diameter hole is bored in the center of the flat steel plate (Figure 3). From the bottom (inside), this hole is enlarged to 1.25-in. diameter to leave a shoulder 0.125 in. wide and 0.0675 in. high at the top, and the enlarged portion is threaded. The orifice to be studied is machined (or drilled) in the top of a hat-shaped orifice plate which fits into the hole in the steel plate; the rim of the orifice plate seats against an O-ring in the wall of the hole. The orifice plate is held in place by a ring nut which runs in the threads of the 1.25-in.-diameter portion of the hole in the steel face-plate. This nut can be long enough to simulate the dimensions of an ordinary Knudsen cell.



1. Steel Face-Plate
2. Hole for Orifice-Plate
3. Brass End-Plates
4. Calibrated Dial
5. Vernier Scale
6. Plexiglass Hemicylinder
7. Brass Axles
8. Ball Bearings
9. Steel Supports
10. Worm Gear
11. Brass Plate
12. Connectors for Tygon Tubes
13. Port for Introduction of Effusant Gas
14. Cutaway to Increase Range of Rotation

Figure 2. The Rotating Cell

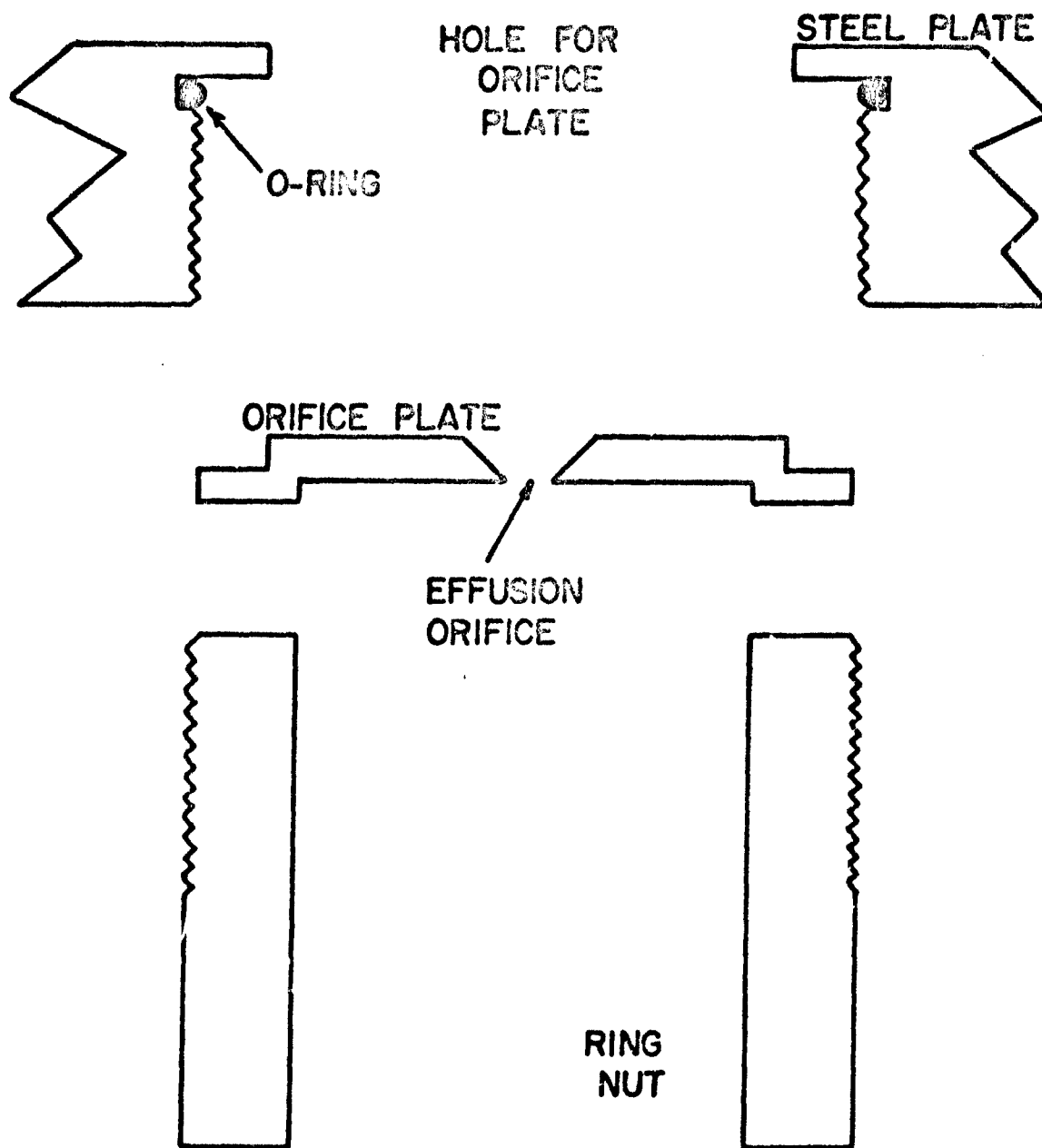


Figure 3. Orifice Plate Assembly

Two brass axles attached to the steel plate permit rotation of the assembled effusion cell about an axis which lies precisely in the plane of the outer face of the orifice. The axles rotate in ball bearings mounted on two steel supports which are attached to a steel base plate. This base plate is part of a simple x,y-table which provides adjustment of the orifice in the horizontal plane; the x,y-table may be raised or lowered by set screws. These adjustments make it possible to align the effusion orifice with the collimating orifices to be described subsequently.

The orifice alignment is facilitated by a glass window in the wall of the main vacuum chamber behind the Plexiglas portion of the cell. This window also makes it possible to check the orifice alignment during the course of a run.

The axis of rotation of the cell is approximately on the longitudinal axis of the main chamber. The cell may be rotated through 180° by a worm gear which is attached to one of the axles and is driven by manual rotation of the mating gear through a vacuum seal. The angle of rotation is measured to ± 0.1 degree with a calibrated dial and vernier which are attached to the end of the cell most distant from the pumping tee of the main chamber. The dial and vernier are read through a glass window in the adjacent vacuum chamber endplate.

To the end of the rotating cell opposite the dial are attached five 0.25-in.-diameter metal tubes, each about 1.0 in. long. To these are attached Tygon tubes through which gas is delivered to the cell from the gas reservoir, and the pressure in the cell is measured.

B. THE GAS RESERVOIR

Gas (e.g., N_2 , CO_2 , He) from a high-pressure cylinder passes in turn through the cylinder regulator, a Lexington Type 10 pressure regulator ($\pm 0.1\%$ regulation), and a Granville-Phillips variable leak into a large low-pressure gas reservoir. This reservoir is a nickel-plated steel cylinder 6 in. in diameter and 18 in. long; its volume is approximately 10

liters. Total reservoir volume may be increased to about 45 liters by attaching another stainless steel tank through an appropriate flange.

The gas reservoir is attached mechanically to the main vacuum chamber by mating flanges, but the two volumes are separated by a plate (Figure 4) which has an O-ring groove on one side and is polished on the other, and which fits between the flanges of the reservoir and the chamber ports. A plate with five short 0.25-in. copper tubes is screwed to the separating plate; to these copper tubes are attached the Tygon tubes from the rotating cell. Four of these tubes carry gas from the reservoir to the cell; the fifth is extended, by means of Tygon tubing, to a vacuum-tight, brass-to-brass coupling in the wall of the reservoir. On the outside of the reservoir this coupling is connected to copper tubulation which leads to an Equibar differential, static pressure meter; hence, the pressure in the cell may be monitored directly.

Another coupling in the wall of the reservoir allows measurement of the pressure in the reservoir, and one in the tee on the main vacuum chamber provides a high vacuum for the reference side of the differential pressure meter. A simple valving system is used to connect the desired chamber to the pressure meter.

The reservoir can be evacuated through a 1.5-in. copper line in which is a 1.5-in. bellows valve and which is connected to the tee on the main vacuum chamber. In operation the reservoir is first evacuated to 10^{-5} torr; then the valve is closed and gas flow is started.

C. THE BUFFER CHAMBER

From the molecular flux which emanates from the effusion orifice a molecular beam is defined by two collimating orifices. During the course of an experiment the high effusion rate from the orifice may cause the pressure in the main chamber to rise to an undesirably high level, and an appreciable number of background molecules may pass through the first collimating orifice. To minimize the number of these stray molecules which pass through the second collimating orifice to the detector chamber, an independently-pumped buffer chamber is situated between the two collimating orifices.

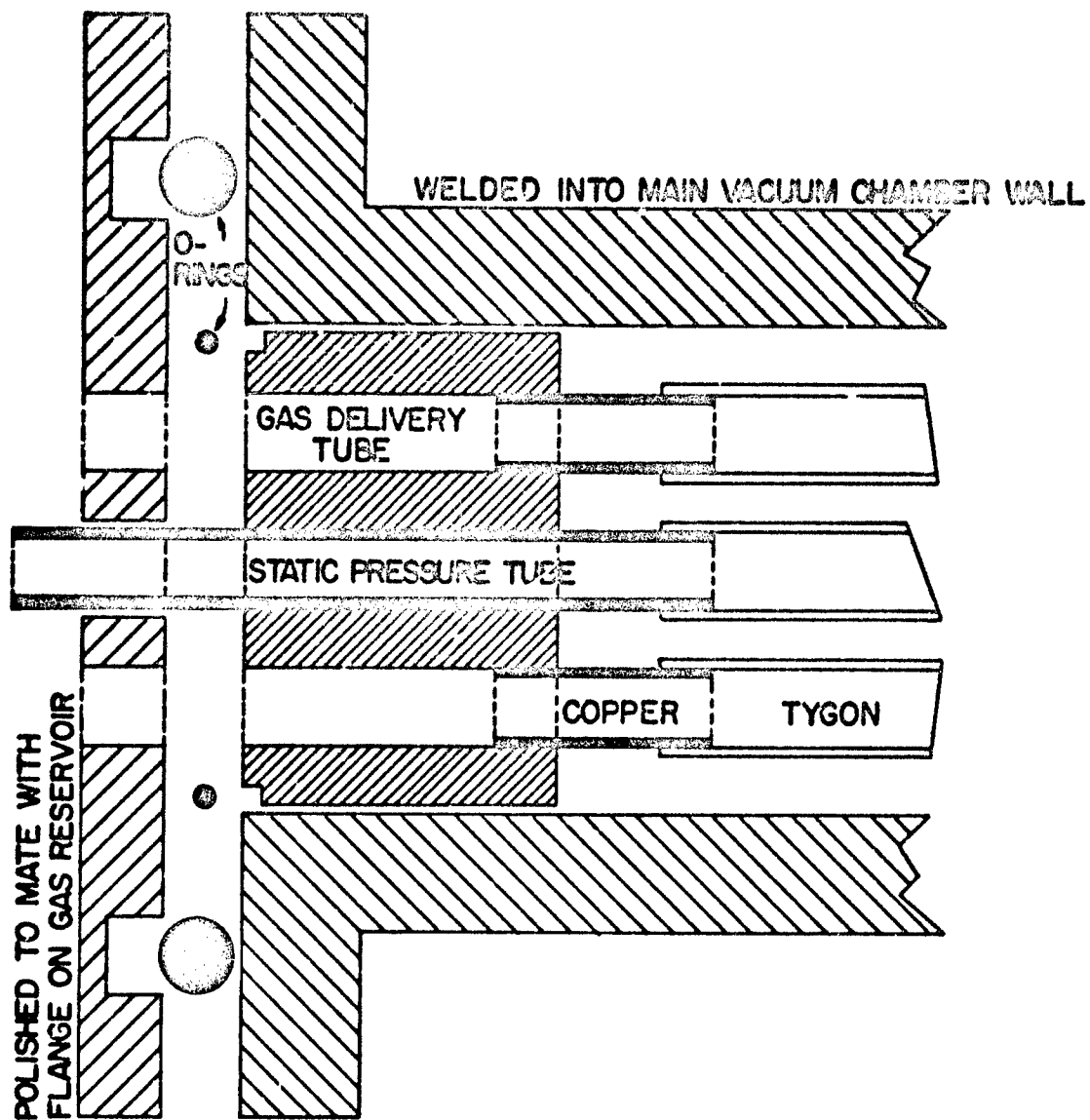


Figure 4. Tubulation Connector Between the Gas Reservoir and the Main Vacuum Chamber.

It is also desirable that the beam molecules which are eliminated by the beam chopper have a minimal chance to reach the detector; therefore the chopper is also located in the buffer chamber.

1. The Vacuum Envelope: A 3.75-in. length of 4-in.-o.d. steel pipe is welded into a 4-in. hole in the side of the main vacuum chamber. One end of this piece protrudes into the main chamber far enough so a flat plate can be placed over the end. Into the side of the small buffer chamber is welded a 2-in.-i.d. steel tee, which provides location for a liquid nitrogen trap and through which the chamber is evacuated by a PMC-100 diffusion pump. A Condulet fitting in the small chamber wall accommodates a vacuum-gauge tube. The PMC-100 pump contains Octoil pump fluid and is backed by the MB-100 pump through the "U"-shaped vacuum chamber described earlier.

To the end of the beam chamber, which is welded into the main vacuum chamber, is attached a 0.125-in. steel plate containing the first collimating orifice. This plate is held in place by four screws which fit into threaded holes in the end of the beam chamber; a gasket of Scotch plastic electrical tape provides a gas-tight seal. The other end of the beam chamber is flanged to mate with a plate on which is mounted the second collimating orifice.

The first collimating orifice has the shape of a truncated, right circular cone with a 90° apex angle. The smaller end of the orifice is oriented toward the effusion orifice so that no effusing molecule can collide with the wall of the collimating orifice and subsequently enter the detector. This orifice is fixed in position and the other orifices are aligned with it. Its size and the size of the second collimating orifice are determined by the size of the effusion orifice; all of the effusion orifice, but a minimum of the rest of the rotating cell, must be visible from the location of the detector.

2. The Beam Chopper: The chopper wheel (Figure 5) is a disc with equally-spaced rectangular teeth on its circumference, each making an angle of 78° with the plane of the disc. In the center of the disc and on the side opposite the teeth is a collar which fits over the driving shaft, or axle, and is secured to it by a set screw.

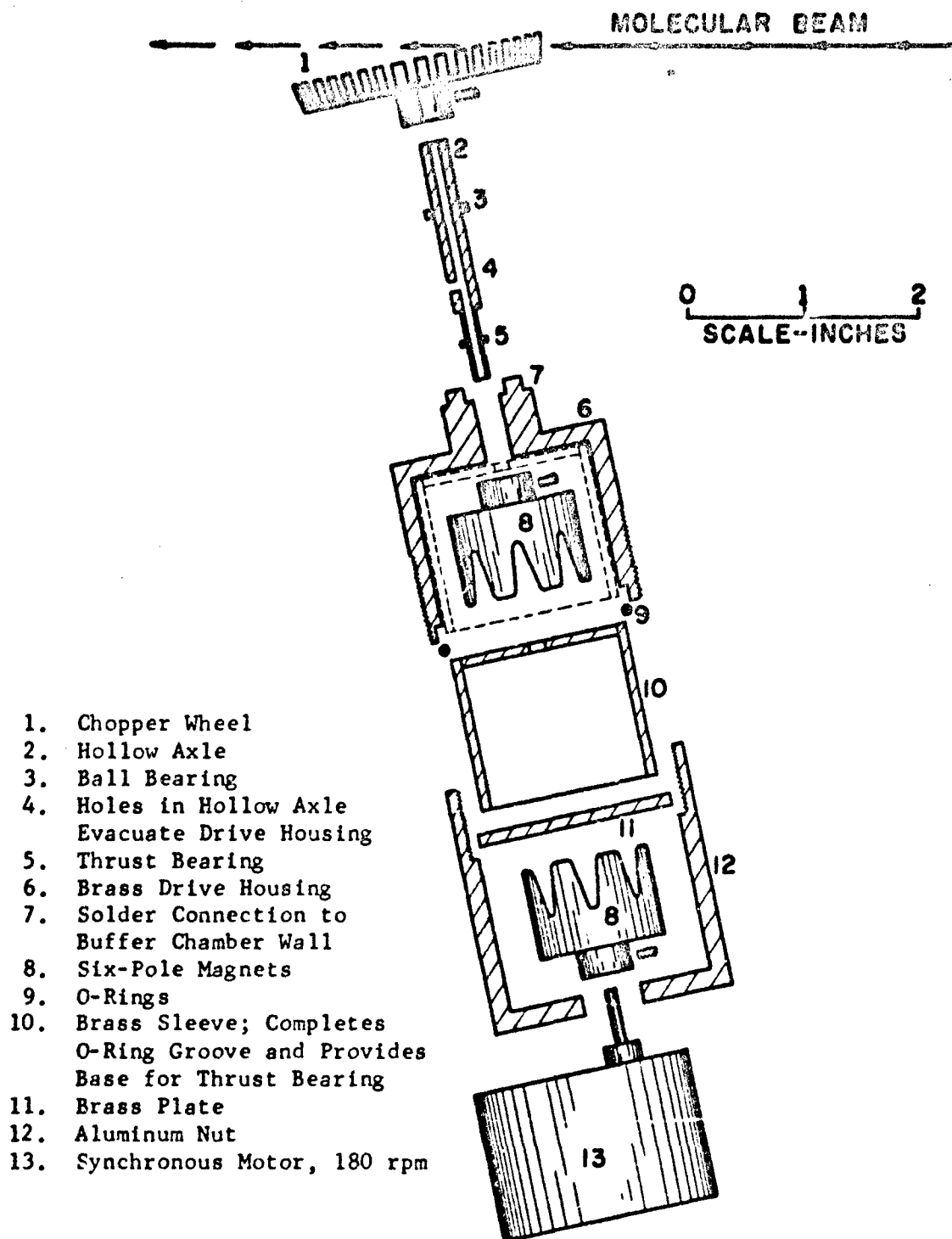


Figure 5. The Chopper Assembly

The brass drive-housing is soldered into a hole in the bottom of the buffer chamber at an angle of 12° from the vertical. The chopper axle passes through a ball bearing and a thrust bearing set in the drive-housing. With these provisions the chopper wheel sets at an angle of 12° with respect to the molecular beam, and as it turns, each tooth is nearly perpendicular to the beam at the point of interception. The chopper axle is hollow to provide for evacuation of the drive-housing.

The chopper is rotated by a coupled magnetic drive similar to the one described by Coenraads and Lavelle¹⁰. At the lower end of the chopper axle is attached, by a set screw, a six-pole magnet. After assembly, the lower end of the housing is sealed with a flat brass plate which seats against an O-ring in the housing and which is secured by a large aluminum nut screwed onto threads cut into the outside surface of the housing. The inside of this nut is hollow and accommodates the external six-pole magnet; the magnet is attached by a set screw to an axle which is driven by a 180 rpm synchronous motor mounted on the nut. A slot in the side of the nut allows adjustment of the external magnet on the axle. As the synchronous motor rotates the external magnet, the internal magnet follows and turns the chopper wheel at the same rate.

A signal generator, which provides for the lock-in amplifier a reference signal synchronous with the pulsed beam, is located in the buffer chamber and associated with the chopper; it is described in the section on the detector electronics.

D. THE DETECTOR CHAMBER

This chamber accommodates the beam ionizer and ion collector. It is independently pumped to provide the high-vacuum environment required by the type of ionizer used and to remove un-ionized beam molecules.

1. The Vacuum Envelope: The vacuum envelope consists of a 6-in. length of 4-in.-i.d. steel tubing with 0.25-in. wall thickness. In the middle of this length is welded a 2-in.-i.d. steel tee, which accommodates a cold trap and a PMC-100 diffusion pump. This pump

is backed by the MB-100 pump through the copper "U"-shaped chamber. Octoil pump fluid is used. A Condulet port is provided for a vacuum gauge.

To one end of the chamber is welded a steel plate (Figure 6) which mates with the flange on the buffer chamber. On this plate is mounted the second collimating orifice; the plate completely separates the buffer chamber from the detector chamber except for the orifice and four holes for adjusting screws. In the center of the plate is a hole 0.75 in. in diameter; a brass plate approximately 2 in. in diameter and 0.38 in. thick with a 0.5-in. hole in the center is soldered on the side of the steel plate which fits against the buffer chamber; the two holes are concentric. In the brass plate is machined an O-ring groove; a 2-in. square steel plate containing the orifice sets on the O-ring. The square plate is held in place by four screws which pass through holes in the plate; the holes are drilled oversize to allow limited two-dimensional movement of the plate. Four screws with tapered ends fit into threaded holes in the chamber endplate; the tapered portions contact the edges of the orifice plate. The square orifice plate is adjusted by retracting and advancing these screws.

To the other end of the chamber is welded a steel flange with an O-ring groove; the end is closed by a flat steel plate. The entire assembly is nickel plated.

2. The Molecular Beam Ionizer: The beam ionizer used in this work is nearly identical with the one described by Aberth¹. The electron gun assembly (Figure 7) is supported by a 1.50 x 0.625 x 0.625-in. molybdenum block. Longitudinally in this block is machined a slot 0.43 in. wide and 0.30 in. deep. The electron source, a Philips type B (barium-aluminate-impregnated) tungsten cathode held in a molybdenum "U"-shaped channel, is supported in this slot by two alumina supports affixed to the end of the block. The holes in the supports, within which the cathode assembly fits, are slightly undersize; the ends of the "U"-shaped channel are ground down slightly, so that the cathode assembly is held firmly in place by the resulting shoulders. The cathode is heated by a six-loop,

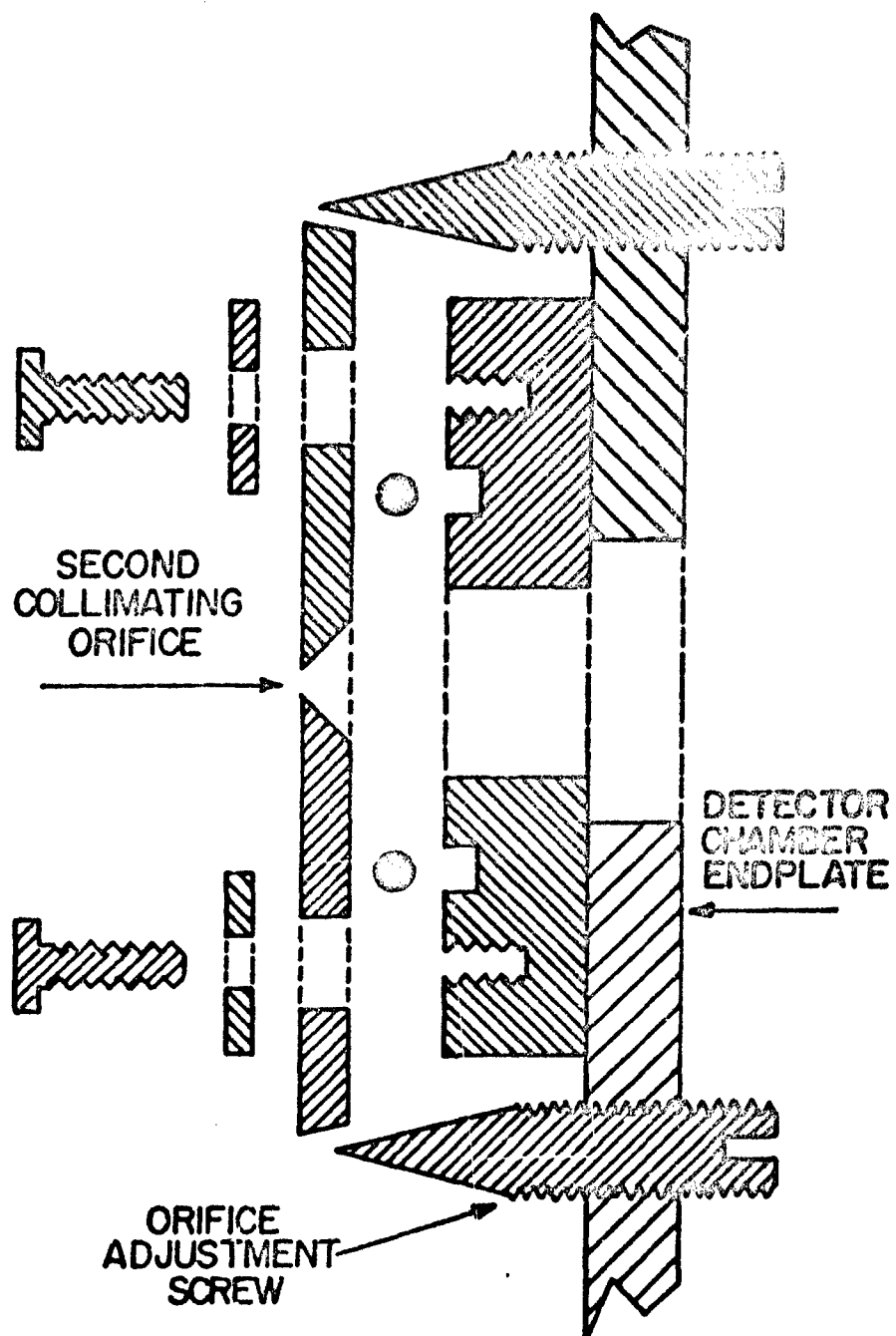
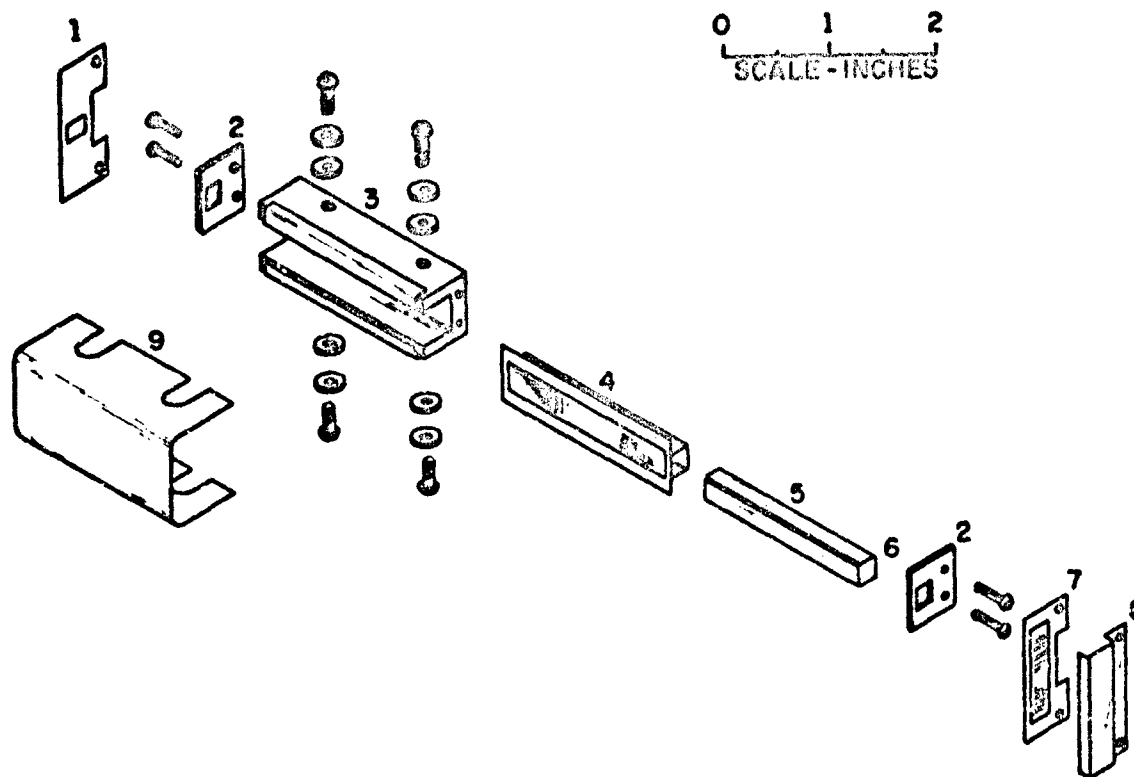


Figure 6. The Second Collimating Orifice



1. Ion-Repression Plate
2. Alumina Support
3. Molybdenum Block
4. Grid and Heat Shield
5. Cathode
6. Slots in Alumina Supports
Accommodate Cathode
7. Ion-Extraction Grid
8. Ion Collector
9. Anode

Figure 7. The Molecular Beam Ionizer.

insulated tungsten heater which slips into the "U"-shaped channel.

Surrounding the cathode assembly on the three sides away from the cathode is a 0.010-in.-thick tantalum heat shield. Atop this heat shield is spotwelded a tantalum frame upon which the grid is wound. The grid is 0.020 in. from the cathode surface, is wound from 0.0015-in. tungsten wire spaced 0.040 in. apart, and has a 0.030 x 1.38-in. rectangular area. The grid-heat shield assembly is held in place by two tantalum clips which are secured to the molybdenum block with molybdenum screws.

A 0.020-in.-thick molybdenum anode is screwed to the molybdenum block; thermal insulation between the anode and the block is provided by boron nitride washers. The distance and tilt of the anode with respect to the grid and cathode is adjustable.

The anode is clamped by set screws into a slot in a water-cooled copper plate which in turn sets in a slot in another copper plate. The latter plate is mounted horizontally on, but is electrically insulated from, a brass plate and can be raised and lowered by three screws. By adjusting the water-cooled plate in its slot and by raising or lowering the second plate, the ionizer may be aligned with the molecular beam.

Along each side of the ionizer is mounted an alumina tube which is approximately 0.13 in. o.d. and 2 in. long. Upon these, at the beam entrance end of the ionizer, is mounted a 0.10-in.-thick, rectangular tantalum plate with a vertical slot in its center; mounting is accomplished with pins inserted into the ends of the alumina tubes. The beam enters through the slot; during a run the plate carries a positive potential to repress back-migration of ions. At the other end of the alumina tubes is mounted the extraction grid and the ion collector. The extraction grid is wound on a 0.10-in.-thick tantalum frame with 0.0015-in. tungsten wire spaced 0.040 in. apart. The ion collector is a shallow, rectangular tantalum cup mounted behind the extraction grid.

The brass plate, upon which the beam ionizer is mounted, is attached perpendicularly to the steel plate which closes the flanged end of the chamber; all electrical connections are made through

this plate, as are water connections for the water-cooled anode. Thus the entire ionizer assembly is conveniently removable with the endplate from the vacuum envelope. Aside from the obvious advantages which accrue from ease of access, this arrangement allows the detector assembly to be placed in a dessicator while the vacuum system is not in operation; exposure of the aluminate-treated cathode to moisture in the atmosphere is thereby minimized. Also the four screws with which the second collimating orifice is adjusted are easily reached with the ionizer assembly removed.

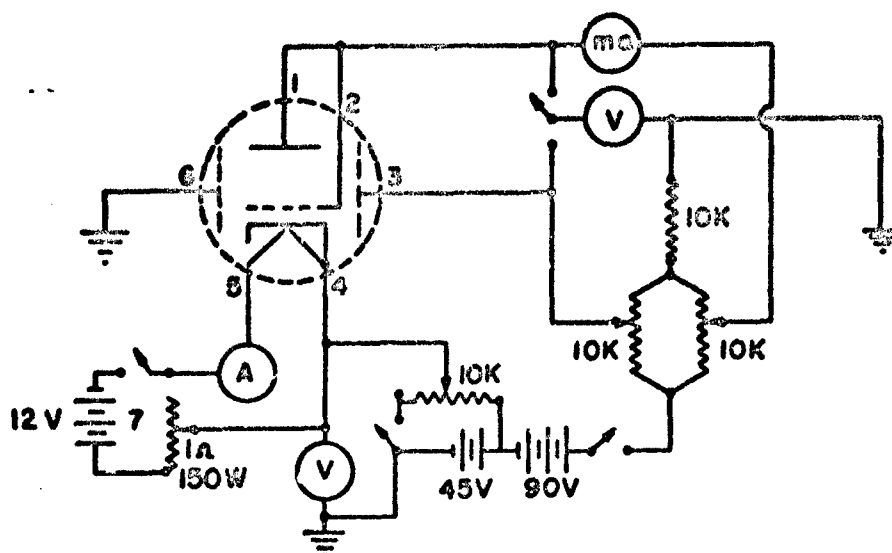
The orientation of the ionizer with respect to the beam is checked by removing the ion collector, replacing the endplate with attached ionizer assembly, and sighting through a small, threaded hole in the center of the endplate. The endplate must be removed again to replace the collector or to make orientation adjustments; reproduceable positioning of the ionizer during these operations is assured by two dowel pins which fit tightly into corresponding holes in the endplate and in the mating flange. After all components are in place and satisfactorily aligned, the sighting hole is closed by a screw with a rubber O-ring in its head.

Also in the detector chamber, mounted on the bottom side of the brass plate to which the ionizer assembly is attached, is the ion-current preamplifier; it is described in the next section.

E. THE DETECTOR ELECTRONICS

1. The Ionizer Power Supply: The relative potentials at which the various components of the ionizer operate are adjustable as shown in Figure 8. The cathode heater current is supplied by a 12-volt automobile battery; all other dc voltages are supplied by Burgess type 5308, 45 volt, "B" batteries.

2. The Current Amplifier: The ion current arriving at the collector consists of an ac component due to ions from the chopped beam, and a dc component due to ions from the background gas in



1. Anode
2. Electron Grid
3. Repression Plate
4. - 5. Cathode and Heater
6. Extraction Grid
7. Heater Power Supply

Figure 8. Power Supply for Beam Ionizer

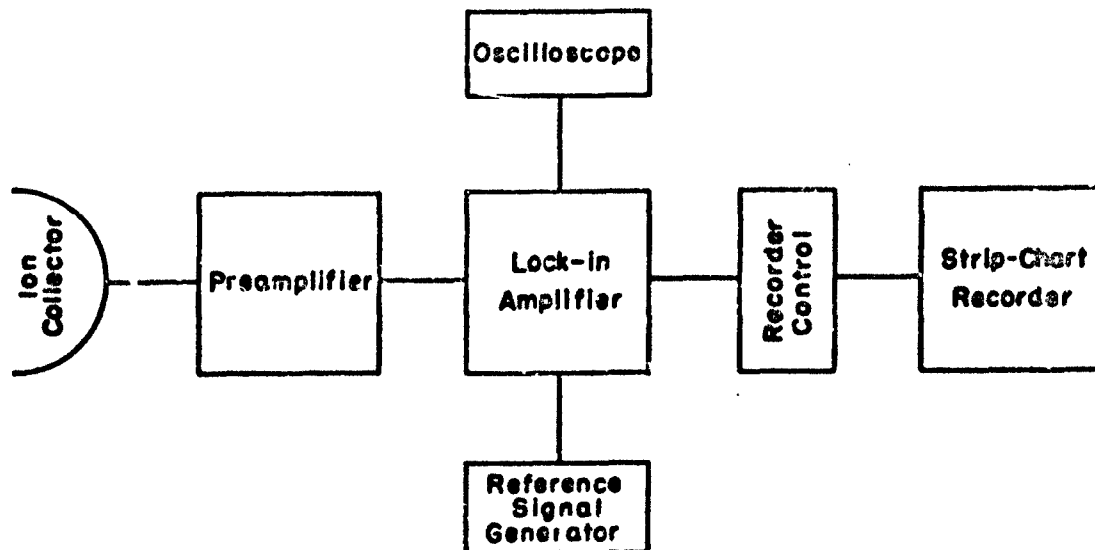


Figure 9. Schematic of Amplification System

the detector chamber*. It is desired to amplify the ac component from the beam, while eliminating the contribution from background ions. The scheme illustrated in Figure 9 accomplishes this. The current from the ion collector passes through a very high (e.g., 10^{10} ohm) resistance, the voltage across which is impressed on the control grid of a CK5702WA subminiature electrometer pentode which is in a plate-follower circuit¹³ (Figure 10). To prevent alteration of the control-grid bias by changes in the dc component of the ion current, which changes could result from fluctuations in background pressure in the detector chamber, a variable dc potential is provided between the plate and the end of the large resistance not connected to the grid; the variable voltage is adjusted to maintain constant plate current¹³. The connection from the plate through the 10^{10} -ohm resistor to the grid also has the effect of a feedback loop; it renders negligible any amplification by the impedance-matching stage, but improves the time constant for passing the ac signal. The dc voltages for the current preamplifier are provided by Eveready No. 457, 67½ volt "B" batteries.

Because very low ion currents are involved ($< 10^{-10}$ amperes) in neutral beam detection, great caution must be exercised in processing the signal. Both the electrometer tube and the 10^{10} -ohm resistor are placed in a shielded container within the detector chamber; the lead from the ion collector to the resistor and control grid of the pentode is made as short as possible to minimize capacitance losses. Shielded cable is used throughout the preamplifier circuit which is grounded at one point only and that point is inside the detector chamber.

Final signal amplification is accomplished by a PAR JB-5 lock-in amplifier. This instrument amplifies only the part of

* The background also contains ac components due to beam molecules which have traversed the ionizer, dispersed, undergone a few wall collisions, and reentered the ionizer. This contribution is small and out of phase with the beam signal; the phase-sensitive amplifier should minimize its effects on the amplified signal.

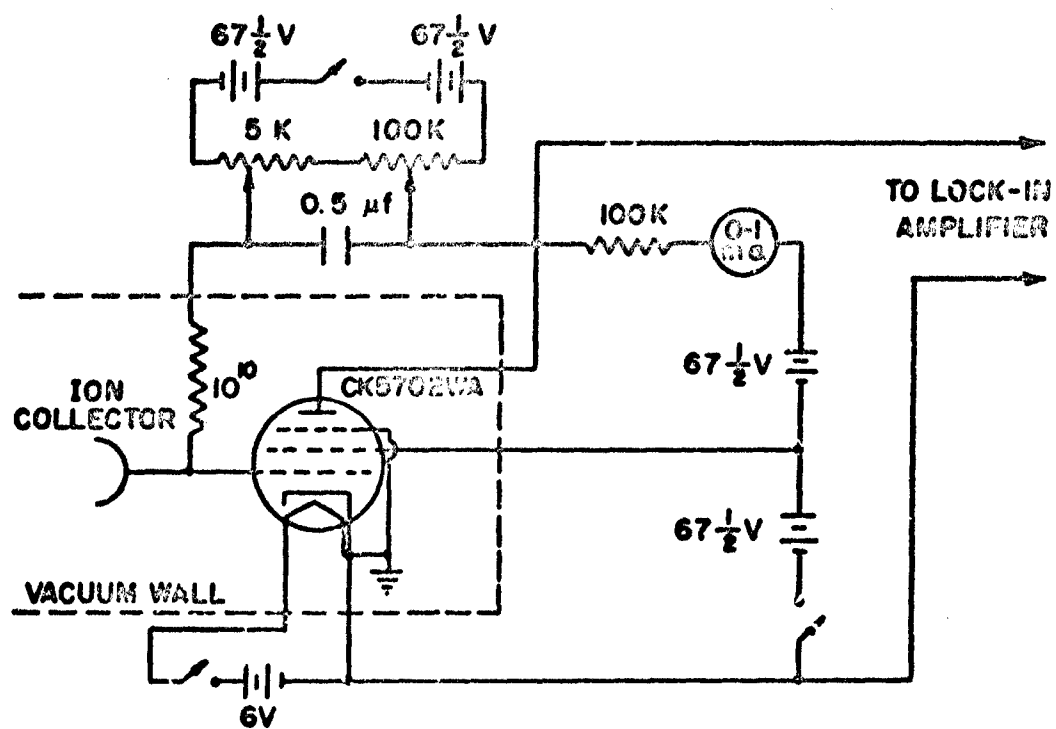


Figure 10. The Preamplifier

the signal which has the same frequency as, and is in phase with, a reference signal which is produced by a photocell, located within the buffer chamber, upon which falls a light beam that is interrupted by the teeth of the beam chopper.

The lock-in amplifier has a gain which is adjustable in seven steps between approximately 10 and 10^4 . With this instrument operating at highest gain and with a 10^{10} -ohm resistor in the pre-amplification stage, an ion current of 10^{-14} amperes, peak to peak, results in an output signal from the lock-in amplifier of approximately one volt, peak to peak. The output signal is continuously monitored with a Brown 10-mv strip chart recorder equipped with a Cahn 1491 recorder control.

SECTION IV

PRELIMINARY RESULTS OF MEASUREMENT OF ANGULAR DISTRIBUTION OF MOLECULAR FLOW THROUGH CONICAL ORIFICES

The performance of the Angular Distribution Apparatus (Section III) in various preliminary tests and the results obtained with the apparatus for a cylindrical orifice ($L/r = 2.42$) are discussed below.

A. RESULTS OF PRELIMINARY TESTS

The accuracy of rotation of the hemicylindrical effusion cell was checked to determine that the axis of rotation passes near the point of intersection of the orifice axis with the outer face of the orifice. With a precision indicator gauge it was determined that, over the angle through which the cell can be rotated, the axis of rotation is never more than 0.002 in. from the desired point. Further, with the cell and effusion orifice in place in the beam apparatus, it was observed that the center of the effusion orifice did not move with respect to the collimating orifices throughout a full rotation.

The performance of the vacuum envelopes and pumping system was tested with the apparatus assembled. Observed ultimate pressures in the various chambers were: gas reservoir, $5-8 \times 10^{-6}$ torr; main chamber, $5-10 \times 10^{-7}$ torr with or without a liquid nitrogen trap; buffer chamber, $1-3 \times 10^{-7}$ torr with a liquid nitrogen trap; detector chamber, $1-3 \times 10^{-7}$ torr with a liquid nitrogen trap. The pressure in the main chamber was not affected by operation of the rotary vacuum seal through which the cell is rotated.

A cylindrical effusion orifice with L/r of 2.42 and diameter of 0.0625 in. was used in several experiments to test the efficiency of the pumping system with air effusing from the orifice. These tests

showed a nearly linear dependence of the pressure in the main chamber on the pressure in the effusion cell; 0.025 torr in the cell resulted in 5×10^{-6} torr in the main chamber, 0.050 torr resulted in 1×10^{-4} torr, 0.250 torr resulted in 5×10^{-4} torr. The pressure in the chopper chamber was monotonically dependent on the pressure in the cell but the dependence was slight; the pressure in the chopper chamber was always less than 5×10^{-6} torr. The pressure in the detector chamber was less than 5×10^{-7} torr and was independent of the pressure in the cell.

The pressure in the "U"-shaped fore-vacuum line was not affected by cell pressures less than 0.08 - 0.1 torr. When the cell pressure increased above 0.1 torr, the fore-pressure increased until, at a cell pressure of about 0.25 torr, gas throughput exceeded the pumping speed of the MB-100 diffusion pump whereupon it ceased to pump efficiently and the fore-pressure rose drastically. This upper limit on throughput does not affect molecular flow effusion experiments which may be done with cell pressures less than 0.25 torr.

The rotation of the beam chopper was checked with a stroboscopic light. Rotation was generally smooth but occasionally a slight rotary oscillation of the wheel was observed. This oscillation resulted from relative vibration of the two coupled magnets in the magnetic drive, probably due to rough spots on the bearings. However, it should not affect the amplification of the signal from the beam detector because the lock-in amplifier is tuned to a signal which is also generated by the chopper and upon which the same vibration is impressed.

B. PRELIMINARY RESULTS FOR A CYLINDRICAL ORIFICE

Angular distribution data have been obtained for nitrogen and for helium, at two pressures each, flowing through a cylindrical orifice with $L/r = 2.42$. The data are presented in Table 1 and are depicted graphically in Figure 11. Most of the symbols used have been defined and discussed in detail^{11,14}; briefly, θ is the angle, measured from the orifice axis, at which the molecule(s) of interest leave the orifice, Q_N is a complicated function of various orifice parameters, and $Q_N \cos \theta$ is proportional to the fraction of effusing molecules

TABLE 1

EXPERIMENTAL DATA FOR ANGULAR DISTRIBUTION
OF MOLECULAR FLOW THROUGH A CYLINDRICAL
ORIFICE WITH $L/r = 2.42$

Angular Intensity, $I(\theta)$

θ	Nitrogen		Helium		
	Pressure in Effusion Cell, dyne/cm ²				
deg.	11.9	93.3	44.0		60.7
0	100	100	100	100	100
10	91.5	91.1	92	90.5	92.7
20	78.0	75.7	68.6	74.8	77.3
30	59.3	56.3	54.5	58.0	58.2
40	41.5	39.1	39.1	40.7	42.7
50	28.8	27.5	27.2	31.0	29.6
60	20.3	17.5	16.9	21.5	19.6
70	14.4	9.2	9.6	9.2	11.5
80	5.9	3.1	3.9	3.3	5.1
90	0	0	0	0	0

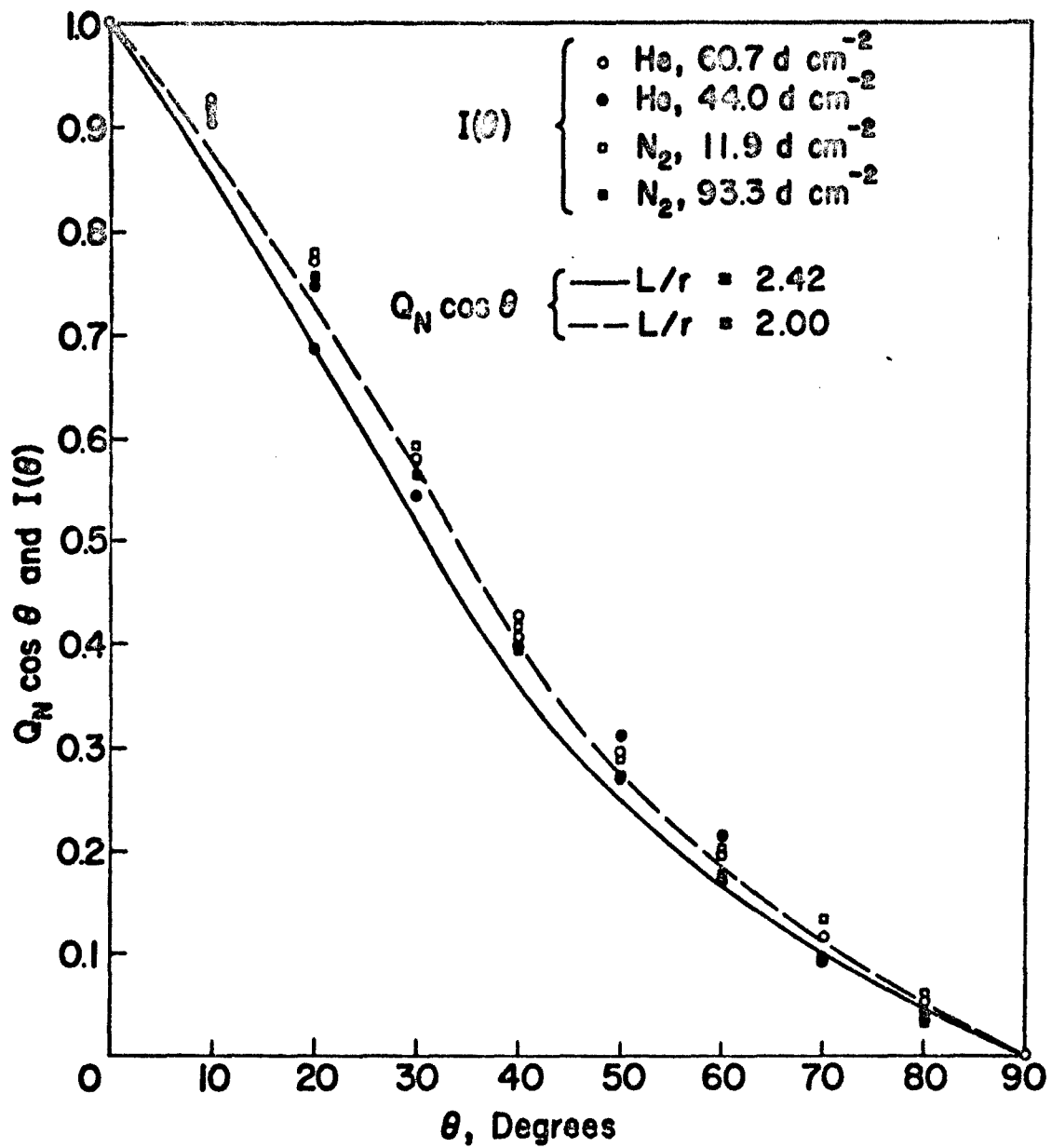


Figure 11. Experimental $[I(\theta)]$ and Theoretical $[Q_N \cos \theta]$ Angular Distribution Data for $T = 0^\circ$, $L/r = 2.42$.

which flow, per steradian, through the incremental solid angle $d\omega$ at angle θ . The experimental variable $I(\theta)$, the angular intensity, is the output current of the lock-in amplifier as read on a strip chart recorder; the values have been normalized to $I(\theta) = 1$ (Figure 11) or 100 (Table 1) at $\theta = 0^\circ$.

The measured angular intensity $I(\theta)$ is assumed to be proportional to the number N_d of molecules which enter the detector orifice per second; N_d is just equal to $dN_\theta(L)$ of reference 11 integrated over the detector orifice area, i.e.,

$$N_d = \int_{\text{detector orifice}} dN_\theta(L) = \int \mu_0 Q_N \cos \theta d\omega.$$

At the center of the front plane of the effusion orifice, the detector orifice subtends an angle $\Delta\theta \approx 0.5^\circ$ and a solid angle of $\sim 2 \times 10^{-5}$ steradians. If we now assume $Q_N \cos \theta$ to be constant over $\Delta\theta = \pm 0.25^\circ$, it immediately follows that, for a fixed pressure (i.e., fixed incident density μ_0) and apparatus geometry (i.e., fixed $d\omega$), N_d and therefore $I(\theta)$ are proportional to $Q_N \cos \theta$. Appropriately normalized values of $I(\theta)$ may therefore be compared directly with $Q_N \cos \theta$, as is done in Figure 11.

The results in Table 1 and Figure 11 are reported as evidence of satisfactory performance of the apparatus described in the previous section, and do not represent "best" or "final" values; these studies will continue.

The only other available angular distribution data are those of Adams² and Phipps who used cesium chloride as the effusant and a surface ionization detector. Figure 12 reproduces a plot given in Adams' thesis (his Figure 9) for CsCl effusing at two pressures through a conical orifice with $L/r = 58.8$ and $T = 15.93^\circ$, and also gives the theoretical curve from our analysis (Section II). The variable plotted on the ordinate is $P(\theta)$ as Adams' defined it and is equal to our $Q_N \cos \theta$ divided by πG (G is the transmission probability of the orifice).

Points to be especially noted in Figure 12 are: (1) the agreement between the general shape of the theoretical curve and Adams' curve for 6.07 millitorr (820°K), particularly in the region in which the slope is discontinuous; (2) the disagreement between theoretical and experimental

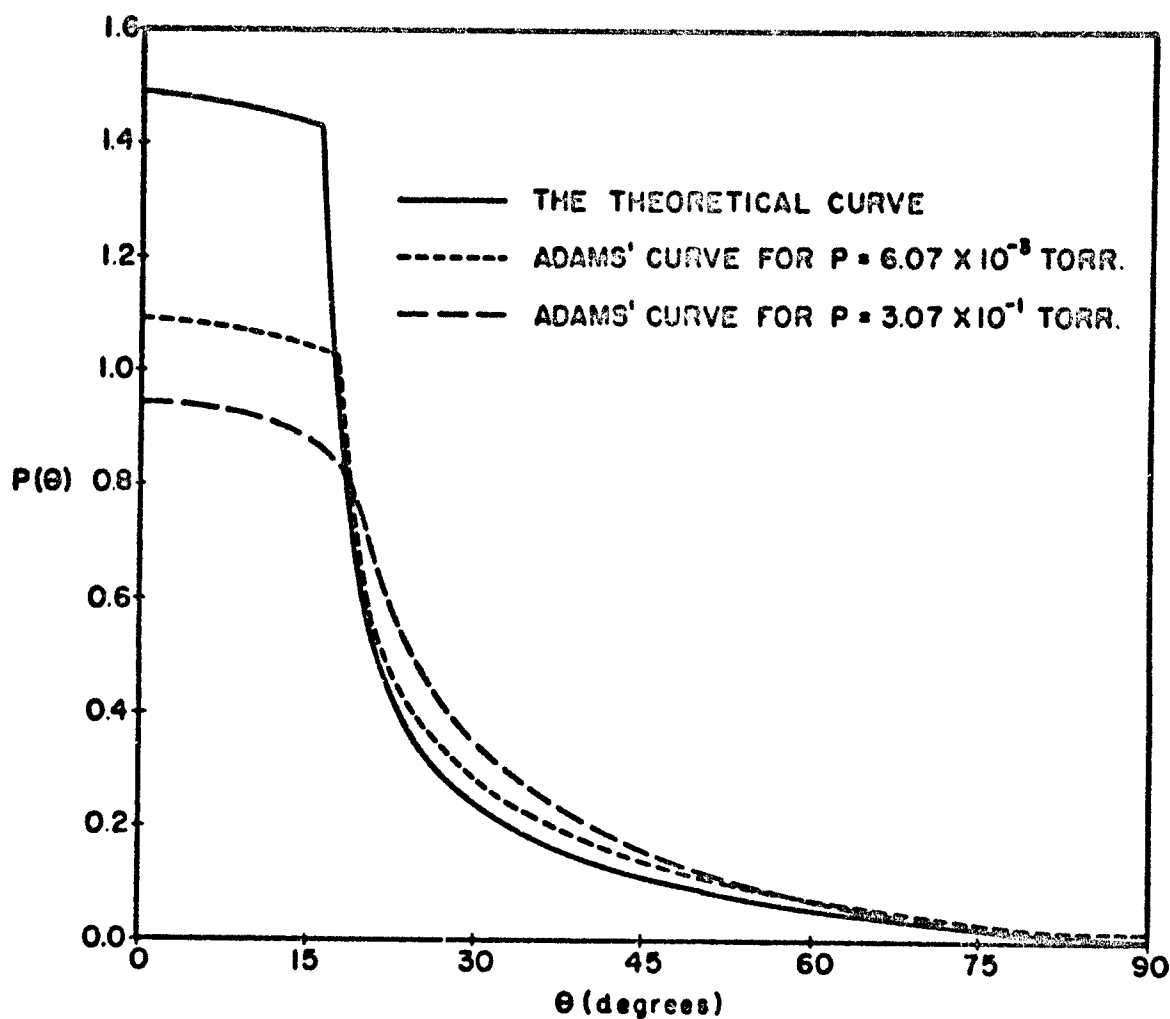


Figure 12. Comparison of the Experimental Results of Adams and the Theoretical Results from This Work for the Angular Distribution of Molecules Effusing from a Conical Orifice With $T = 15.93^\circ$ and $L/r_m = 58.8$.

curves in values of $\underline{P}(\underline{\theta})$, particularly for $0 \leq \underline{\theta} \leq 18^\circ$; (3) the lack of a discontinuity in slope for Adams' curve for 0.307 Torr (960°K), which could be interpreted as indicating lack of molecular flow conditions.

SECTION V

THE MULTICELL TECHNIQUE FOR EXPERIMENTAL DETERMINATION OF TRANSMISSION PROBABILITIES FOR MOLECULAR FLOW THROUGH CONICAL ORIFICES

Part I of ASD TDR 63-754¹⁴ described in detail the Multicell Technique. The essence of the technique is that several (6 to 10) Knudsen effusion cells, which are "identical" in every respect except for differing orifice lengths and which contain "identical" samples, are simultaneously heated in vacuum with all cells continuously exposed to "identical" environments. Variation among the cells of rate-of-effusion, and of total weight loss over a given time, should then depend only on the relative lengths of the orifices, or on the ratio of length of orifice to radius of orifice. A rather simple and straightforward analysis (see Part I) of the weight losses leads to experimental values for the transmission probabilities of the various orifices.

Undesirably large probable errors were associated with the preliminary results, which were obtained with the Multicell Technique and reported in Part I. The wide scatter of the data apparently was caused primarily by slight but non-reproducible oxidation of the surface of the cadmium samples during a run. Despite various leak-hunting techniques and the use of various bakeable vacuum seals, the vacuum system was never sufficiently tight to eliminate completely the oxidation.

We have designed and constructed a new stainless steel vacuum system in which there are no heated vacuum seals. The system performs quite satisfactorily; cadmium samples have been heated to 250°C for several hours with no evidence of oxidation. Currently, new effusion cells and a new copper cell holder are being fabricated.

SECTION VI

THE MIKER TECHNIQUE

In Part I of this report¹⁴ the rationale of the Microbalance-Inverted Knudsen Effusion-Recoil (MIKER) technique was discussed in detail and a brief description of the pertinent apparatus was given. In this section a more detailed description of the apparatus and the technique is given and various results are reported.

A. DESCRIPTION OF THE TECHNIQUE

The principal innovation of the Miker technique is the inverted effusion cell shown in Figure 13. The cell is suspended from a microbalance into a suitable furnace and effusion occurs only in the downward ($-z$) direction, away from the microbalance. The conservation of momentum requires that the cell receive, in the $+z$ direction (upward), momentum identical in magnitude to the momentum possessed by the effusing molecules in the $-z$ direction. The rate of change with time of this momentum is defined as the recoil force. At a constant temperature the recoil force is constant and the variation of the weight of the cell with time yields the rate of effusion. After the rate of effusion has been established at a particular temperature, the power to the furnace is suddenly reduced to zero, and the cell allowed to cool rapidly so as to minimize further effusion. The cell immediately appears "heavier" to the microbalance due to the rapid disappearance of the recoil force. Both this apparent gain in mass by the cell and the rate of effusion data can yield information regarding vapor and/or decomposition pressures within the cell, and combination of the recoil data with rate of effusion data can give an average molecular weight for the effusing species.

1. Theoretical Analysis: In the equations which describe the effusion and the recoil processes it is desirable to distinguish three symbols for

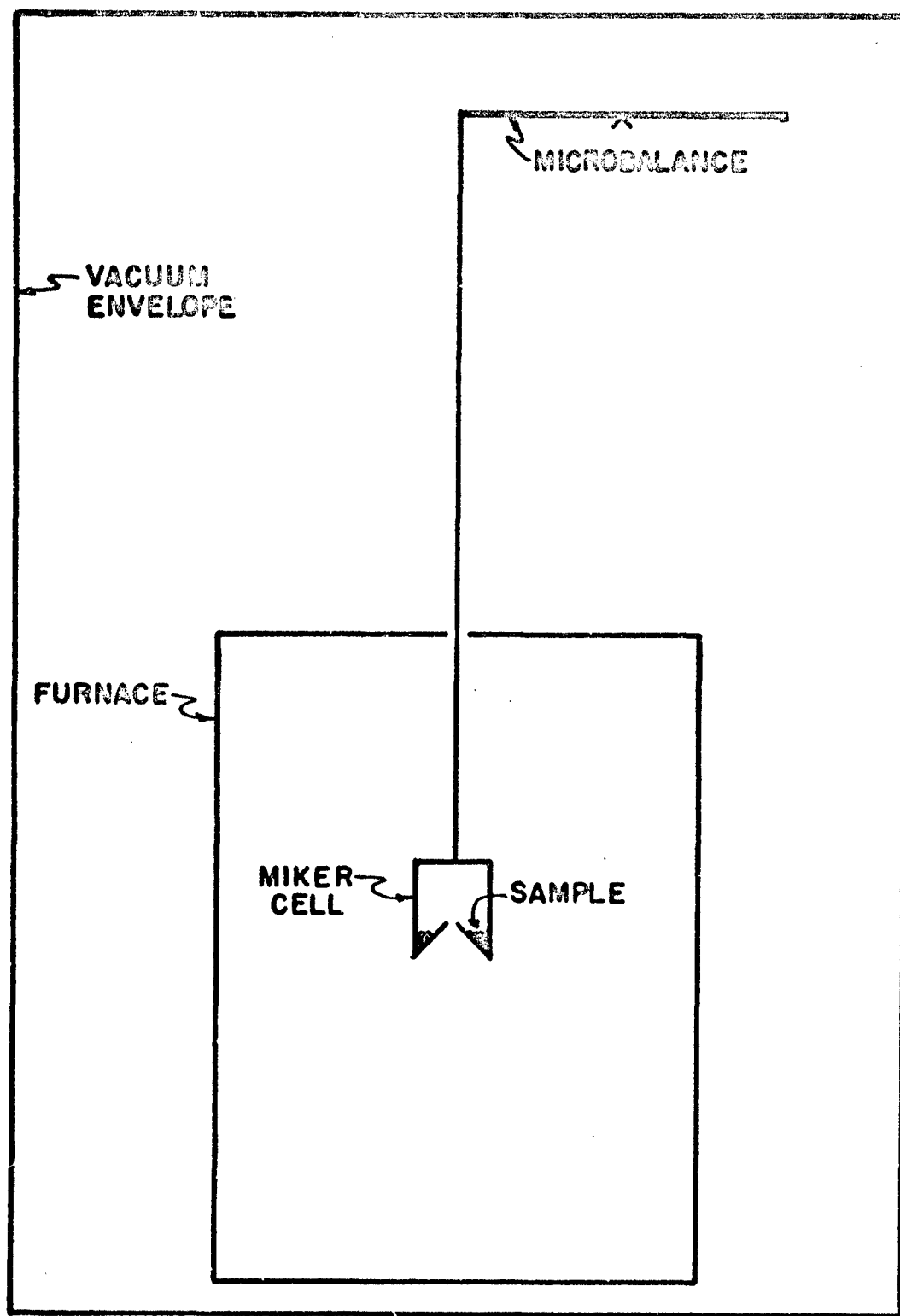


Figure 13. Schematic Representation of Apparatus for Mikker Technique.

pressure: \underline{P} shall designate the actual pressure within the cell; \underline{P}_K , the pressure calculated from Knudsen (i.e., rate of effusion) data for which calculation a molar mass \underline{M}_K is assumed for the effusing species; and \underline{P}_R , the pressure calculated from recoil force data. The modified Knudsen effusion equation, which relates the pressure within the cell at temperature \underline{T} to the rate of effusion \dot{w} (g/sec) through an orifice with area \underline{a} and transmission probability¹¹ \underline{W} , is

$$\underline{P}_K = (\dot{w}/aW)(2\pi RT/\underline{M}_K)^{1/2}. \quad (1)$$

Freeman and Searcy¹⁵ have noted, and Edwards¹¹ and Freeman and Edwards¹⁶ have given a detailed derivation, that the recoil force \underline{F} is related to the pressure within the cell by

$$\underline{P}_R = 2F/af \quad (2)$$

in which \underline{f} is the recoil-force correction for a non-ideal orifice (see Part I¹⁴).

It is obvious from equation (1) that $\underline{P}_K = \underline{P}$ only if the correct value of \underline{M}_K is known; on the other hand, if the factor \underline{f} is valid, there is no known reason, other than experimental errors and perhaps a small cell-geometry correction²⁹, why \underline{P}_R should not equal \underline{P} . Therefore, if \underline{M}_K^* is the value of \underline{M}_K which makes $\underline{P}_K^* = \underline{P} = \underline{P}_R$, one may write

$$\underline{P}_R = 2F/af = (\dot{w}/aW)(2\pi RT/\underline{M}_K^*)^{1/2}. \quad (3)$$

Rather than use rate of effusion data and recoil force data in equation (3) to find \underline{M}_K^* directly, it is often convenient to calculate \underline{P}_R and \underline{P}_K via equations (1) and (2) with an assumed value for \underline{M}_K (e.g., in the vaporization of sulfur one might logically assume for \underline{M}_K the molar mass of S_8 ; in some instances it might be desirable to set arbitrarily $\underline{M}_K = 1$) and then obtain \underline{M}_K^* from combination of equations (1) and (3):

$$\underline{M}_K^* = \underline{M}_K (\underline{P}_K/\underline{P}_R)^2. \quad (4)$$

Searcy and Freeman³⁶ have previously given equation (4) and have noted that \underline{M}_K^* is an averaged molar mass which is related to the molar masses \underline{M}_i and mass fractions ω_i of the various effusing species by

$$\underline{M}_K^* = (\sum \omega_i \underline{M}_i^{-1/2})^{-2}. \quad (5)$$

It may be useful to note the result of equation (5): suppose only monomer ($\underline{M}_1 = 100$) and dimer ($\underline{M}_2 = 200$) are present in the effusing vapor; if mass fractions are equal ($\omega_1 = \omega_2 = 1/2$), $\underline{M}_K^* \cong 137$; if mole fractions are equal ($\omega_1 = 1/3$; $\omega_2 = 2/3$), $\underline{M}_K^* \cong 154$.

2. Effusion During the Cooling Period: Ideally, after the rate of effusion has been established at a particular temperature and the furnace has been suddenly de-energized, effusion ceases immediately, and the recoil force F is obtained from the (ideal) recoil mass \underline{m}_i , i.e., the apparent increase in mass of the cell (Figure 14), and gravitational acceleration g :

$$F = \underline{m}_i g. \quad (6)$$

For any real system, however, cooling is not instantaneous and effusion will occur during the cooling period. This effusion during cooling results in a decrease \underline{m}_c in mass of the cell, while the disappearance of the recoil force constitutes an apparent increase \underline{m}_i . The microbalance senses the resultant of these two effects (Figure 14): the measured recoil mass \underline{m} is $\underline{m} = \underline{m}_i - \underline{m}_c$. It then follows immediately from equations (2) and (6) that

$$P_R = 2g(\underline{m} + \underline{m}_c)/af. \quad (7)$$

Obviously, if $\underline{m}_c \geq 0.01\underline{m}$, \underline{m}_c must be determined and incorporated into the calculation of P_R . There appear to be at least three approaches to this problem: (1) eliminate the problem by achieving such rapid cooling that \underline{m}_c is insignificant; (2) determine \underline{m}_c with cells which have orifices in the side only and hence produce no recoil force detectable by the microbalance; (3) compute \underline{m}_c from knowledge of the rate of cooling of the cell. The first of these would require a cooling rate of several hundred degrees per second in a system in which temperature uniformity and stability are required until the instant the furnace is de-energized, and in which energy loss by the cell is almost entirely by radiation; the conflicting requirements appear unresolvable at present. The second approach should give reliable data and is relatively easy to execute, but has not yet actually been tried. The third approach has received considerable attention and is discussed in detail in subsection VI. D.

B. DESIGN AND CONSTRUCTION OF THE APPARATUS

1. The Microbalance: Effusion from a cell in which the pressure is 10^{-3} to 10^{-6} atm produces recoil forces in the range 1 to 10^{-3} dynes, or 10^{+2} to 1 microgram weight. To measure these forces with a precision

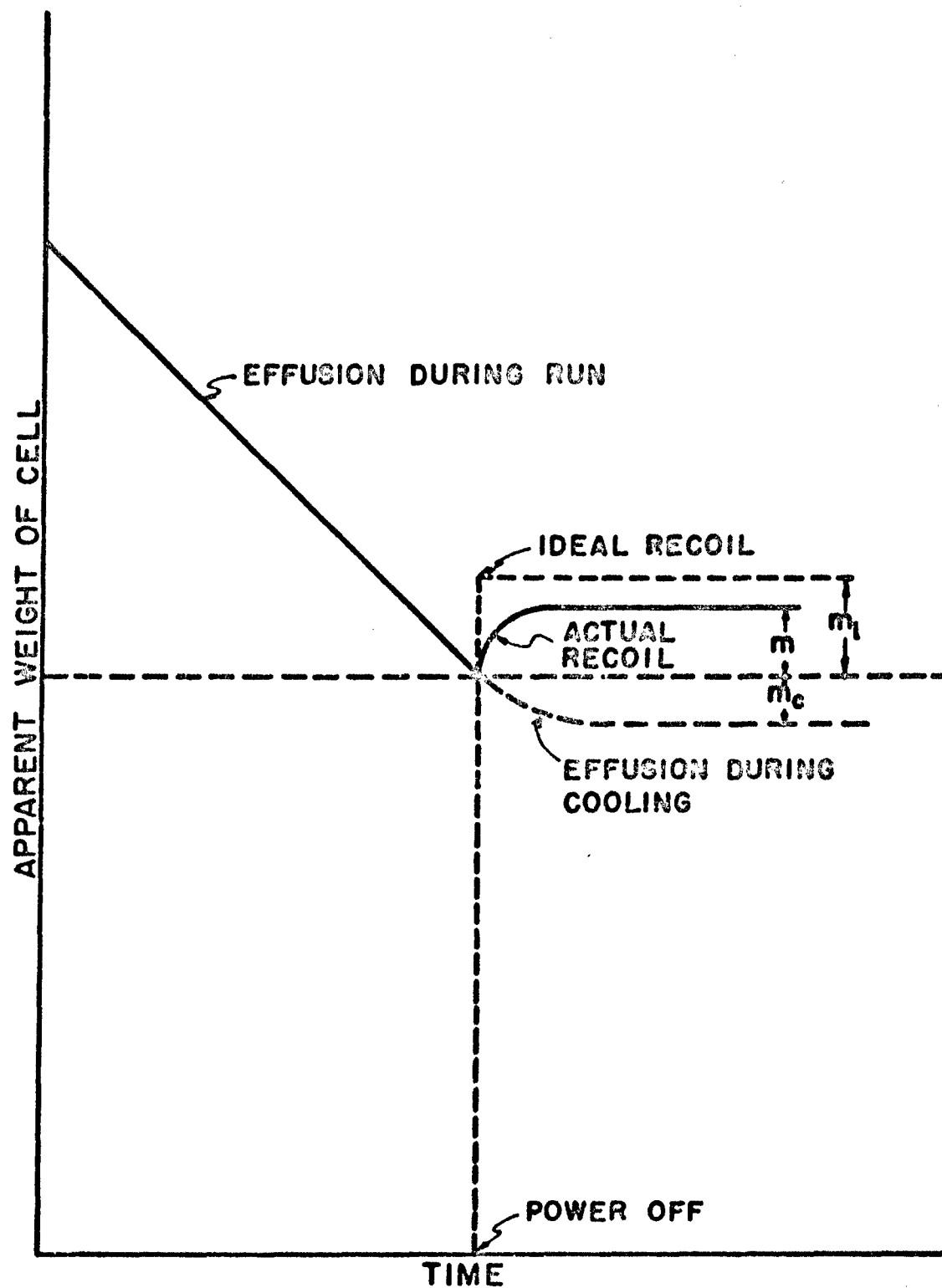


Figure 14. The Effect on the Recoil Mass of Effusion which Occurs During the Cooling Period.

of one per cent a balance is needed with a sensitivity of at least 10^{-6} g, and preferably 10^{-7} g. A rather small Miker cell will have a mass of 2-5 g. Therefore a balance suitable for the Miker technique must have the characteristics: (1) operable in vacuum; (2) sensitivity of about 10^{-7} g; (3) load capacity of at least 5 g. No restrictions need be imposed because of high temperatures; with suitable shielding the balance itself can be operated at room temperature.

The pivotal-type vacuum microbalance constructed for this research is depicted in Figure 15; it bears the laboratory designation VMB-1. Several new features have been introduced. The balance beam (A) is a 6.3-in. length of stainless steel tubing with 0.094-in. i.d. and 0.120-in. o.d. Two polished diamond points (tip radius 0.001 in.) mounted on small jewel screws (C) serve as center pivots. Holes in an aluminum mounting block (B) accomodate the jewel screws so that the pivot tips are 0.5000 ± 0.0005 in. apart. The mounting block is attached to the beam with epoxy adhesive. Polished-sapphire cups (S), also mounted on jewel screws, serve as bearing surfaces for the diamond pivots. The cups, or vees, are mounted in a block so that their minima are separated by 0.5000 ± 0.0005 in. in the horizontal plane. Point and vee alignment is fixed by lock screws (D and U).

Supports typically used at the ends of the beam are the hook type⁸, the quartz-on-tungsten-wire type²⁴, or the two-pivot type³⁴. To minimize friction and to simplify the problem of adjusting all bearing surfaces to be in a common plane, VMB-1 has a single pivot (H) mounted, tip upward, at each end of the beam; these pivot tips and the center ones are adjusted so that they are in a common plane within 0.0005 in. With only one pivot at each end of the beam, this adjustment is relatively simple. The surface which bears on the end diamond pivots is again a sapphire cup (L) (inset, Figure 15--only one is shown). A stirrup (P) is attached by thin aluminum strips (M) to the sapphire cup at two points in a horizontal plane slightly below the point of contact between the tip of the pivot and inverted sapphire cup. Loads are suspended from the cross-piece of the stirrups. The aluminum mounting blocks (F) for the diamond end-pivots are sealed in the ends of the hollow beam with epoxy adhesive. An opening is provided at each end for evacuation of the hollow beam.

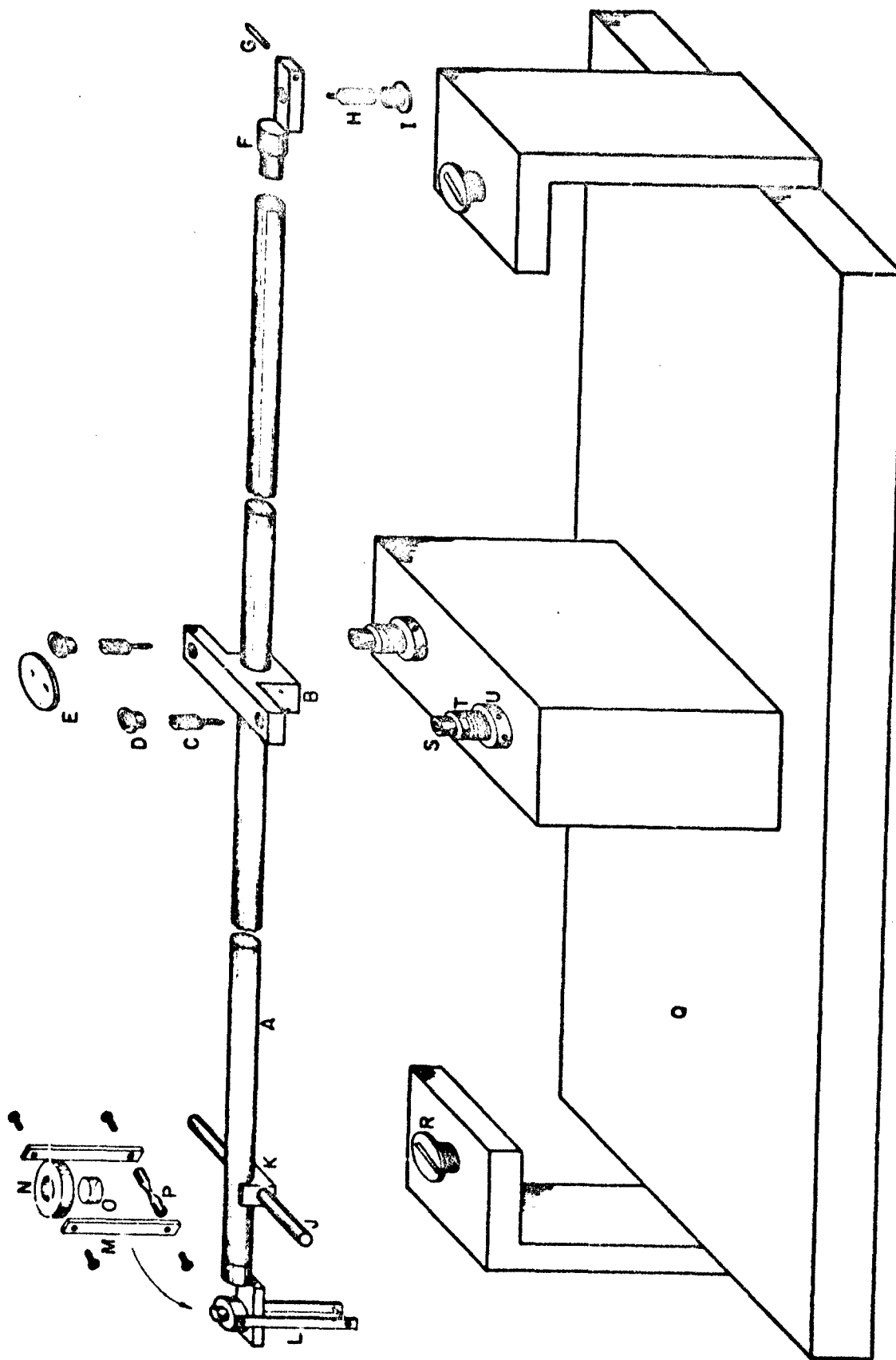


Figure 15. The Vacuum Microbalance, VNB-1.

A thin front-surface mirror (E) with 0.25-in. diameter is mounted on top of the center aluminum block and midway between the center pivots. About 0.5 in. from one end of the beam, a small aluminum block (K) is attached by epoxy adhesive to the bottom of the beam. This serves as a mount for a 0.062-in.-diameter Cunife wire magnet (J). The magnet is held in the mounting block by a tight frictional fit, which permits interchange of magnets with various lengths. When properly installed, a given magnet is perpendicular to the beam and protrudes equal distances on each side of the beam.

The base (Figure 16) for the balance was constructed from 0.25-in. brass plate. The sapphire cups (F) for the center pivots are mounted on adjustable screws which are accommodated by a brass block attached to the base plate (E). The base plate has in the bottom three V-grooves which rest on ball bearings (D) mounted in fixed sockets of a second brass plate (C). This is to ensure that the balance and base plate can be removed and later returned precisely to the original position. Two adjustable knife-edge beam stops (R, Figure 15; G, Figure 16) are attached to the base plate. The second plate (C) rests on four sharply-pointed screws (B) which serve as a leveling device.

2. Magnetic Balancing System: The method for achieving magnetic coupling for control of the balance beam position is a modification of methods employed by Simon, Shierrer, and Ritter³⁸, and by Gerritsen and Damon¹⁷. Each end of the Cunife magnet (J, Figure 15) extends halfway into the gap between a pair of hemicylindrical coils (H, Figure 16). Each coil has approximately 2000 turns of A.W.G. No. 30 copper wire on a solid copper core. The gap between the flat sides of a pair of coils is 0.25 in. Control of the position of the balance beam is achieved by varying the current through the four coils which are wired in series. A reversing switch in the circuit makes it possible to drive either downward or upward the end of the beam to which the magnet is attached.

To minimize problems arising from poor heat dissipation in vacuum, the coils are mounted on a copper block which is in good thermal contact with the brass vacuum envelope and which therefore serves as a good heat sink. Difficulty from overheating (and from consequent variation of the coil resistance) was experienced in earlier models in which about 3500 turns per coil of A.W.G. No. 36 copper wire were wound on four Lucite cores.

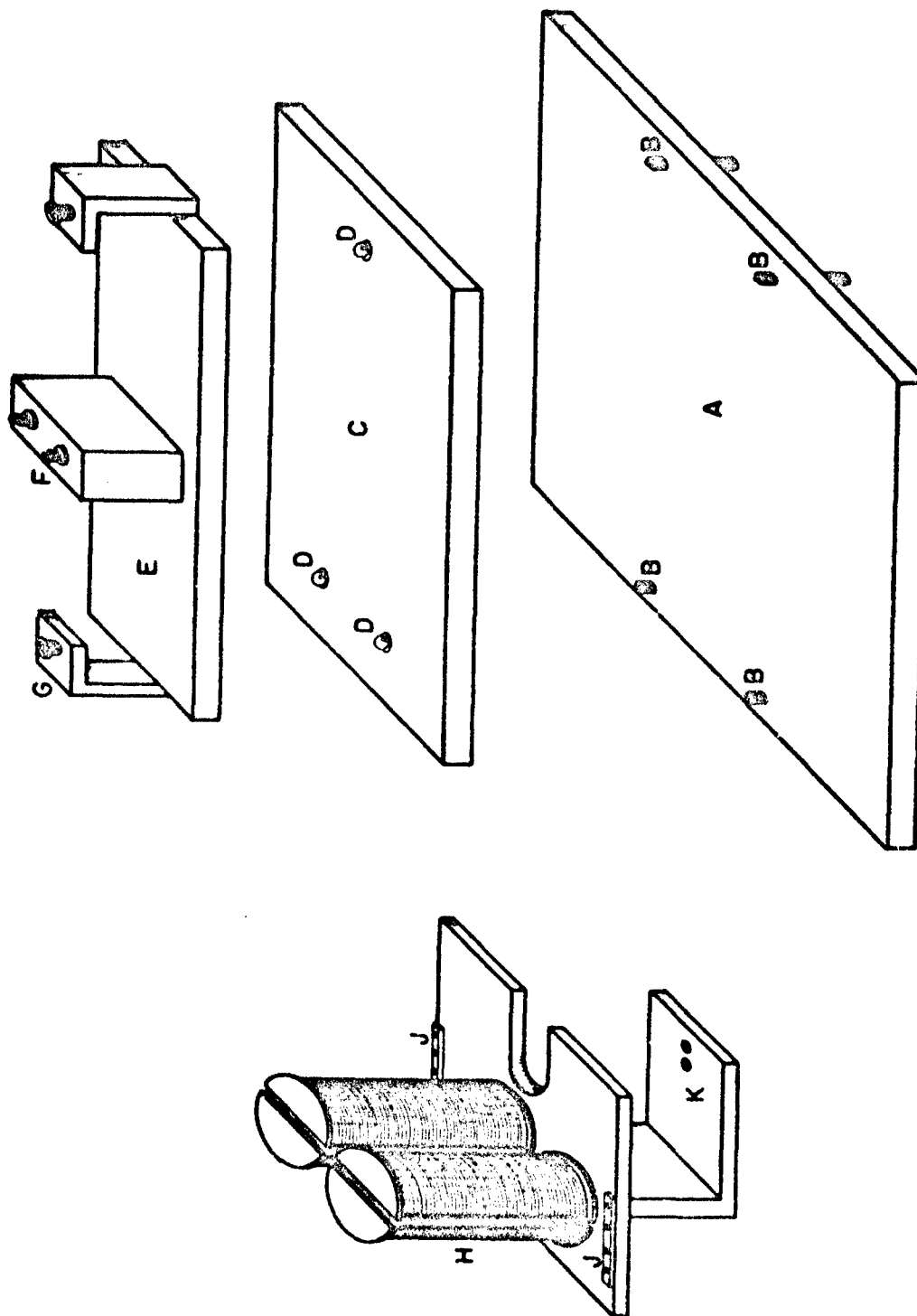


Figure 16. The Base Assembly for Supporting, Leveling, and Providing Kinematic Alignment of the Microbalance.

The magnet is mounted on the end of the beam from which the Miker cell is suspended; this results in a constant-load balance.

3. Sensitivity of VMB-1: Theoretical analysis^{19,41} of the simple equal-arm beam balance gives for the sensitivity $d\theta/dz$ of the balance

$$d\theta/dz = b/(Gs + 2Qa); \quad (8)$$

all symbols are defined and illustrated in Figure 17. Beam arm-length (b) is typically³¹ 6-7.5 cm (b for VMB-1 is 8.5 cm); beam load is fixed by the application of the balance (for VMB-1, $5 \leq Q \leq 10$ grams); and the beam mass G (for VMB-1, 4.3 g), which for maximum sensitivity should be as low as possible consistent with rigidity (see below), is determined by choice of beam design and material.

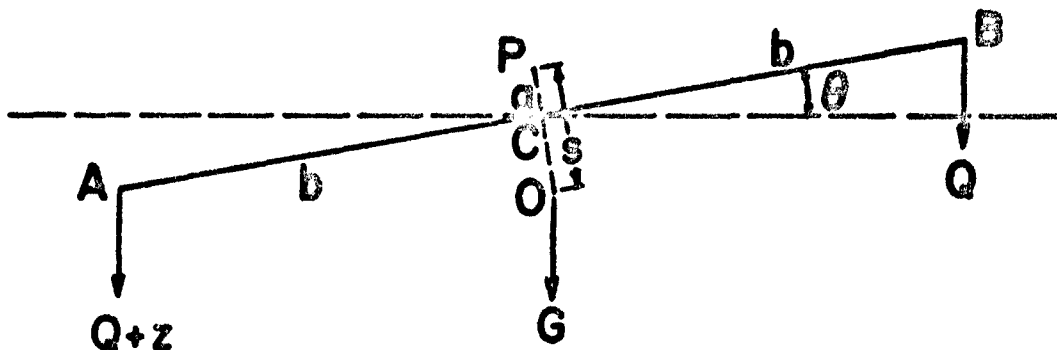
The two parameters a and s which are fixed during construction are available for optimization of the sensitivity. If the center pivot points are coplanar with the terminal pivot points, $a = 0$, and the quantity $2Qa$ becomes zero. This is the first step toward making the balance sensitivity independent of load. The next is to make certain that s is not a function of the load. Ideally, the points of contact at the center pivots and those at the end pivots should be in a common horizontal plane. If the beam bends under load, the center of gravity (O, Figure 17) shifts downward, s increases and the sensitivity decreases. Hence, if s is to be independent of load, the balance beam must not flex under load.

It was noted above that the four point contacts on VMB-1 were adjusted to within 0.0005 in. of the plane which bisects the beam; therefore, $a = 0 \pm 0.0013$ cm. The stainless steel tubing from which the beam was cut was tested for bending under load by fastening it securely at a point 8-10 cm from one end and suspending rather large masses from the free end. With a mass of 50 g, the deflection was 0 ± 0.0005 in. This result and the fact that in normal use the maximum load suspended from each end of VMB-1 is < 10 g indicate that the balance sensitivity should be virtually independent of beam-bending effects.

It follows from $a \approx 0$ that equation (8) may be simplified to

$$d\theta/dz = b/Gs \quad (9)$$

and the theoretical sensitivity may be calculated from a knowledge of b , G , and s . It is convenient to obtain s from the expression for the period of oscillation of the beam⁴¹; the natural period (τ) of the (unloaded)



- P = fulcrum knife-edge (center diamond pivots)
- A, B = terminal knife-edge (diamond pivot)
- C = midpoint of AB which has length $2b$
- O = center of gravity of beam which has mass G
- Q = load on right side
- $Q + z$ = load on left side
- θ = angular deflection of beam from horizontal
- a = PC
- s = PO

Figure 17. Diagram Illustrating the Simple Theory of the Equal-Arm Balance.

beam oscillating about its center pivots is given by

$$\tau = 2\pi I_B / gGs, \quad (10)$$

where I_B is the moment of inertia of the beam, and g is the gravitational constant.

The period τ of VMB-1 was found to be 4 sec; I_B was calculated to be 90 g cm^2 ; and from above, G is 4.3 g. The value for s calculated from equation (10) is $s = 0.03 \text{ cm}$, which is consistent with s values of other microbalance designs (Walker⁴¹, $s \approx 0.01 \text{ cm}$; Gulbransen¹⁹, $s \approx 0.04 \text{ cm}$).

The sensitivity may now be calculated from equation (9): $d\theta/dz = 66 \text{ radians/g}$. This means that for $L = 8.5 \text{ cm}$, a change in load of $1 \mu\text{g}$ should result in a deflection of the end of the beam by approximately $8.5 \times 66 \times 10^{-6} \text{ cm}$ or about 6μ . If it is assumed for the moment that deflections of 1μ can be detected, the balance sensitivity appears to be well within the desired limits which were quoted earlier.

4. Choice of Materials: Stainless steel tubing was chosen as the beam material for VMB-1 because of its lightness, strength, resistance to corrosion, the precision which is attainable in machining it and attaching components to it, and ready availability. Quartz is undoubtedly superior as a beam material in some respects, e.g., it is chemically inert, has low coefficient of thermal expansion, and is non-magnetic. Any future versions of VMB-1 will probably have a beam of precision quartz tubing. The mounting blocks attached to the beam could still be aluminum, thereby retaining the advantage of relatively easy constructional precision.

Invar tubing was also considered as a beam material. Gulbransen and Andrew²⁰ employed this material to construct a simple (solid) beam balance for the study of fast chemical reactions. Because of its low coefficient of thermal expansion, Invar should be given serious consideration as a beam material if the balance is to be subjected to appreciable temperature changes. However, VMB-1 operates at a relatively constant temperature and Invar offers no special advantage. Furthermore, its ferromagnetism eliminates Invar as the beam material in a balance which employs a magnetic field to compensate for weight changes.

Contrary to manufacturer's claims, the stainless steel tubing was slightly ferromagnetic. As a result, some "sticking" of the beam to the original steel knife-edge stops (R, Figure 15) was experienced; brass stops eliminated this problem.

There are several reasons for the selection of diamond pivots and sapphire vees. The most important factors which determine the feasibility of any pivot-vee combination are friction, pivot load, and vibrations. Theoretically, friction is minimized by minimizing the contact area between the pivot and the vee, which suggests the use of infinitely sharp points. In practice pivot points must be rounded because exceptionally sharp points deform under load. This factor obviously limits the ultimate ratio of load capacity to sensitivity in microbalance design. Optimum design requires use of that material which yields the largest number for the ratio: (load at which pivot distortion occurs)/(pivot radius). Diamond appears a clear choice. Stott³⁹ has determined empirically that the minimum radius for no distortion in a steel pivot subjected to a 10-g load is about 0.004 cm or 0.0016 in. The minimum radius for a diamond pivot should then be smaller by the ratio of the compressive strength (~500,000 pounds per square inch) for steel to the compressive strength (~2,000,000 pounds per square inch) for diamond, or about 0.0003 in. The pivots which were used (radius \cong 0.0010 in.) had the smallest radius of pivots which were readily available at the time of construction; pivots with 0.0007-in. radius are now commercially available.

Once the pivot dimensions are selected, it is a rather simple matter to select the vee. The vee radius should be 2 to 3 times the pivot radius to balance the necessity for minimum contact area with the need to avoid excessive lateral play between the pivot and vee. The depth and angle of the vee are important when vibrations are likely to exist. Deep vees with relatively steep angles are considered superior to shallow or wide-angle vees when vibrations must be accommodated. The vees on VMB-1 have a radius of 0.0045 in., an included angle of 65° , and a depth of 0.035 in.

The hardness, ready availability, and easy adaptability of sapphire vees make them an excellent choice for the diamond pivots. Another reason for choosing the diamond-sapphire combination is that, in spite of their apparent advantages, we find no previous workers who have tried these materials as microbalance components, though Honig²⁴ suggested the possible use of diamond pivots, and Cochran⁹ used a sapphire vee-tungsten pivot combination.

5. Automatic Control System: The control system described in Part I never performed satisfactorily in automatic mode. There were two principal difficulties: the cadmium sulfide crystals which served as light-beam sensors had an illuminated/dark resistance ratio which was too high; and the servo motor-driven potentiometer did not have sufficiently rapid response. An all-electronic control system has now been assembled; the major units in the system are available commercially.

The new control system also employs optical detection of beam motion; the detector is a Photopot which is a light-actuated electrical potentiometer. It consists of two parallel strips of metal (vacuum-deposited) on a photoconductor. One strip (R_1 , Figure 18) is so thin that its electrical resistance is high (e.g., 20 kilohm). The other strip (R_0) has extremely low resistance. The familiar brush or contact wiper of the ordinary potentiometer is replaced by a spot of light which illuminates the photoconductor between R_1 and R_0 . The equivalent circuit of the Photopot is shown in Figure 18(b); the resistance of the spot-illuminated photoconductor is represented by R_2 . In Figure 19(a) and (b) are shown a typical Wheatstone bridge arrangement and its equivalent circuit.

Since the Photopot is a relatively new device (ours bears serial number "7"), some additional comments are perhaps in order. The sensitivity of the Photopot varies directly with light intensity if the output load impedance is low; if output load impedance is high (> 1 megohm), the sensitivity is virtually independent of light intensity. To achieve maximum sensitivity consistent with freedom from noise and drift, it is advisable for bridge-circuit applications to have the light intensity as low as practical and to have high output load impedance. It is rather obvious that, for null-seeking applications, linearity of the Photopot is of little consequence; however, if linearity is desired, it can be obtained with relatively high light intensity and, of course, high load impedance.

The manufacturer claims that in null-seeking applications the Photopot is capable of stable zero readings with a dead band corresponding to movement of the light spot less than 1 micron. This sensitivity is readily credible: with only 1 volt across the ~2-cm-long high-resistance element of the Photopot, a movement of the light spot by 1μ produces an output voltage change of 50 μ v which is easily detectable. We have not yet had

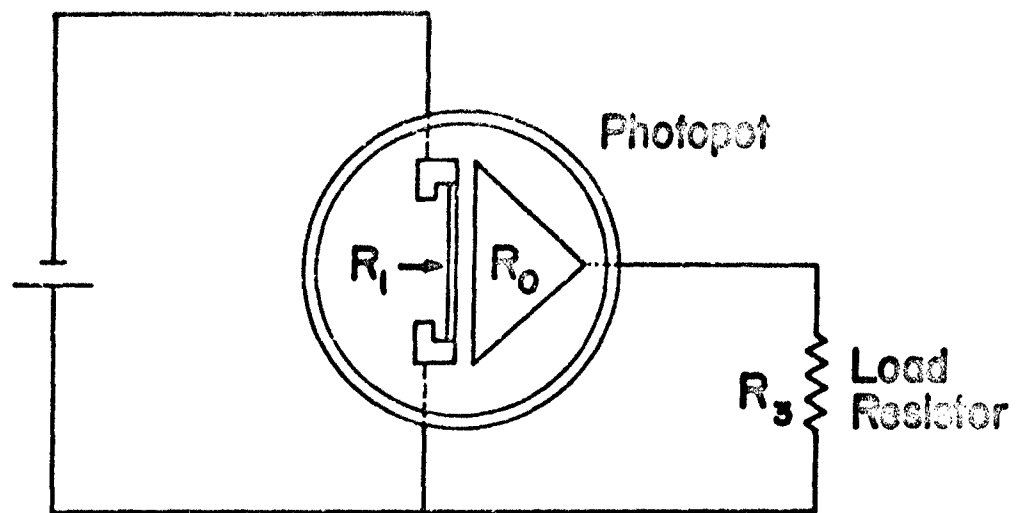
5. Automatic Control System: The control system described in Part I never performed satisfactorily in automatic mode. There were two principal difficulties: the cadmium sulfide crystals which served as light beam sensors had an illuminated/dark resistance ratio which was too high; and the servo motor-driven potentiometer did not have sufficiently rapid response. An all-electronic control system has now been assembled; the major units in the system are available commercially.

The new control system also employs optical detection of beam motion; the detector is a Photopot which is a light-actuated electrical potentiometer. It consists of two parallel strips of metal (vacuum-deposited) on a photoconductor. One strip (R_1 , Figure 18) is so thin that its electrical resistance is high (e.g., 20 kilohm). The other strip (R_0) has extremely low resistance. The familiar brush or contact wiper of the ordinary potentiometer is replaced by a spot of light which illuminates the photoconductor between R_1 and R_0 . The equivalent circuit of the Photopot is shown in Figure 18(b); the resistance of the spot-illuminated photoconductor is represented by R_2 . In Figure 19(a) and (b) are shown a typical Wheatstone bridge arrangement and its equivalent circuit.

Since the Photopot is a relatively new device (ours bears serial number "7"), some additional comments are perhaps in order. The sensitivity of the Photopot varies directly with light intensity if the output load impedance is low; if output load impedance is high (> 1 megohm), the sensitivity is virtually independent of light intensity. To achieve maximum sensitivity consistent with freedom from noise and drift, it is advisable for bridge-circuit applications to have the light intensity as low as practical and to have high output load impedance. It is rather obvious that, for null-seeking applications, linearity of the Photopot is of little consequence; however, if linearity is desired, it can be obtained with relatively high light intensity and, of course, high load impedance.

The manufacturer claims that in null-seeking applications the Photopot is capable of stable zero readings with a dead band corresponding to movement of the light spot less than 1 micron. This sensitivity is readily credible: with only 1 volt across the 2-cm-long high-resistance element of the Photopot, a movement of the light spot by 1μ produces an output voltage change of $50 \mu\text{v}$ which is easily detectable. We have not yet had

(a)



(b)

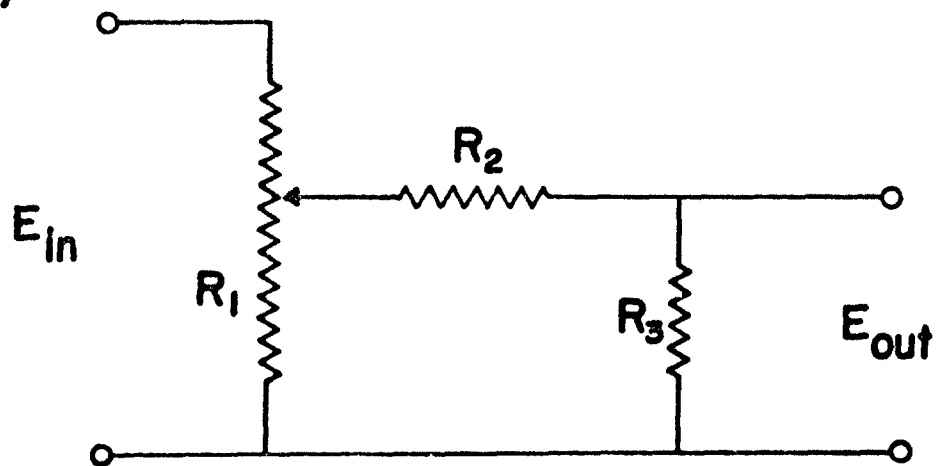


Figure 18. Photopot in Unipolar Circuit

- (a) Electrical Wiring
- (b) Equivalent Circuit

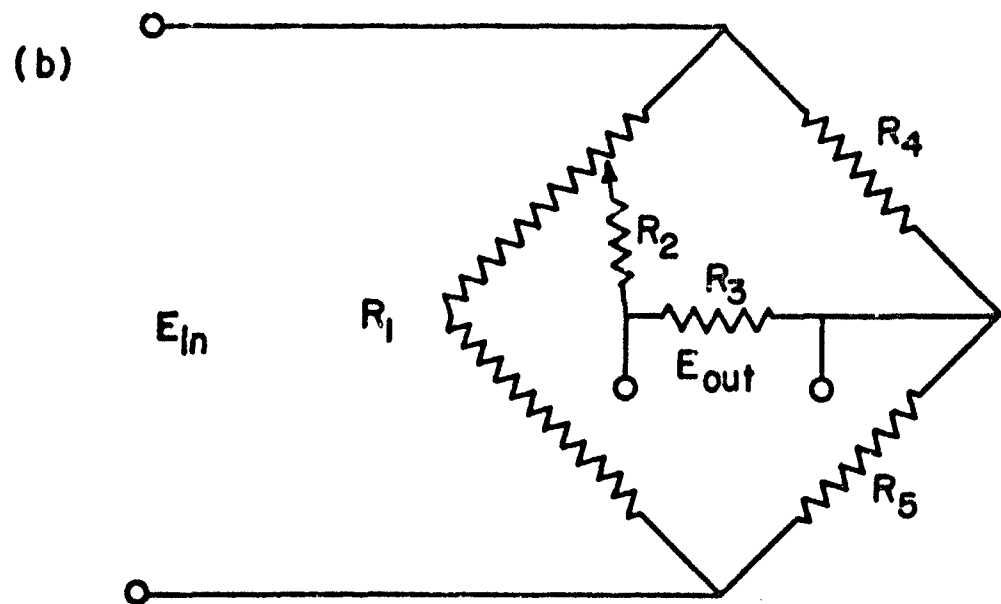
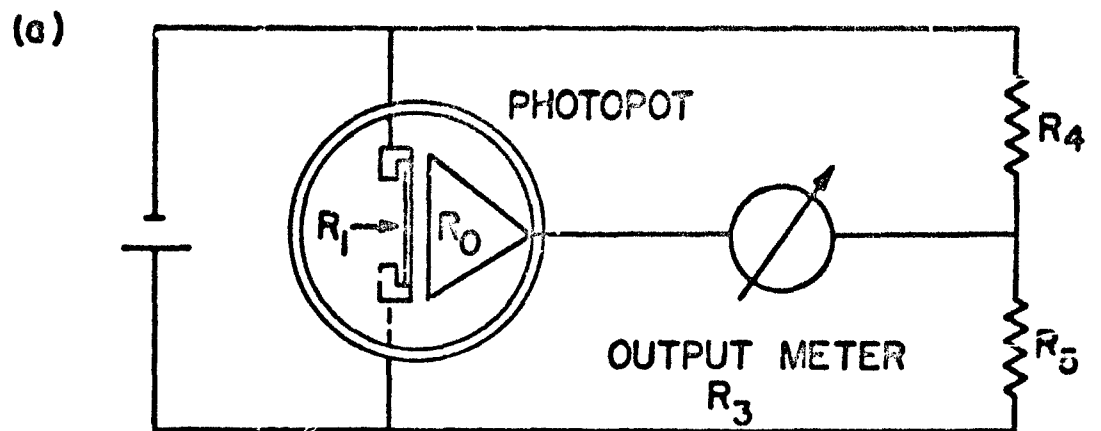


Figure 19. Photopot in Bipolar Circuit

- (a) Electrical Wiring
- (b) Equivalent Circuit

sufficient experience with the Photopot to comment in detail on the stability and drift characteristics.

In the Wheatstone bridge circuit of our control system (Figures 20 and 21), traverse of the light spot along the Photopot produces an output voltage which varies from negative through null to positive; the instantaneous position of the spot, and hence the balance beam, is indicated by an output "error" voltage which is characterized by a polarity and a magnitude. Output from the Photopot bridge (i.e., error signal representing motion of balance beam) is amplified by a dc null detector (L & N 9834-2) and fed to a current-adjusting-type (CAT) controller (L & N 10877), which provides proportional, rate, and reset control actions. Output from the CAT unit controls a magnetic amplifier the rectified and filtered output of which goes to the solenoids which control the balance beam position. Manual control of the solenoid current may be accomplished with the 10-turn potentiometer in the solenoid circuit or with the manual control feature of the CAT controller.

6. Miker Cells: The majority of the experimental work was performed with Miker cells (Figure 22) which were constructed from 0.5 in.-diameter graphite (type AUC) rod. The cell lid is threaded and screws into the cell body as indicated. No special difficulty was encountered in the construction of cells, but "good" threads were required as a safeguard against the possibility of leaks. The cell is attached to the balance suspension by a molybdenum hook which fits closely in the slotted section of the lid and engages a molybdenum pin inserted through the hole in the slotted section.

7. The Furnace: The heating element (Figure 23) is a modification of one employed by Blakelock and Machin⁶; it is a hollow graphite (type AUC) cylinder with 4-in. length, 1.5-in. o.d., and 1.1-in. i.d. Longitudinal slots which extend to within 0.25 in. of the top and bottom of the element are spaced at 45° intervals around the element to produce the desired electrical resistance. The current flows through a graphite section approximately 0.2 in. thick and 0.4 in. wide except at the ends, where the section is about 0.25 in. wide. This construction provides increased resistance, and therefore increased power input per unit length

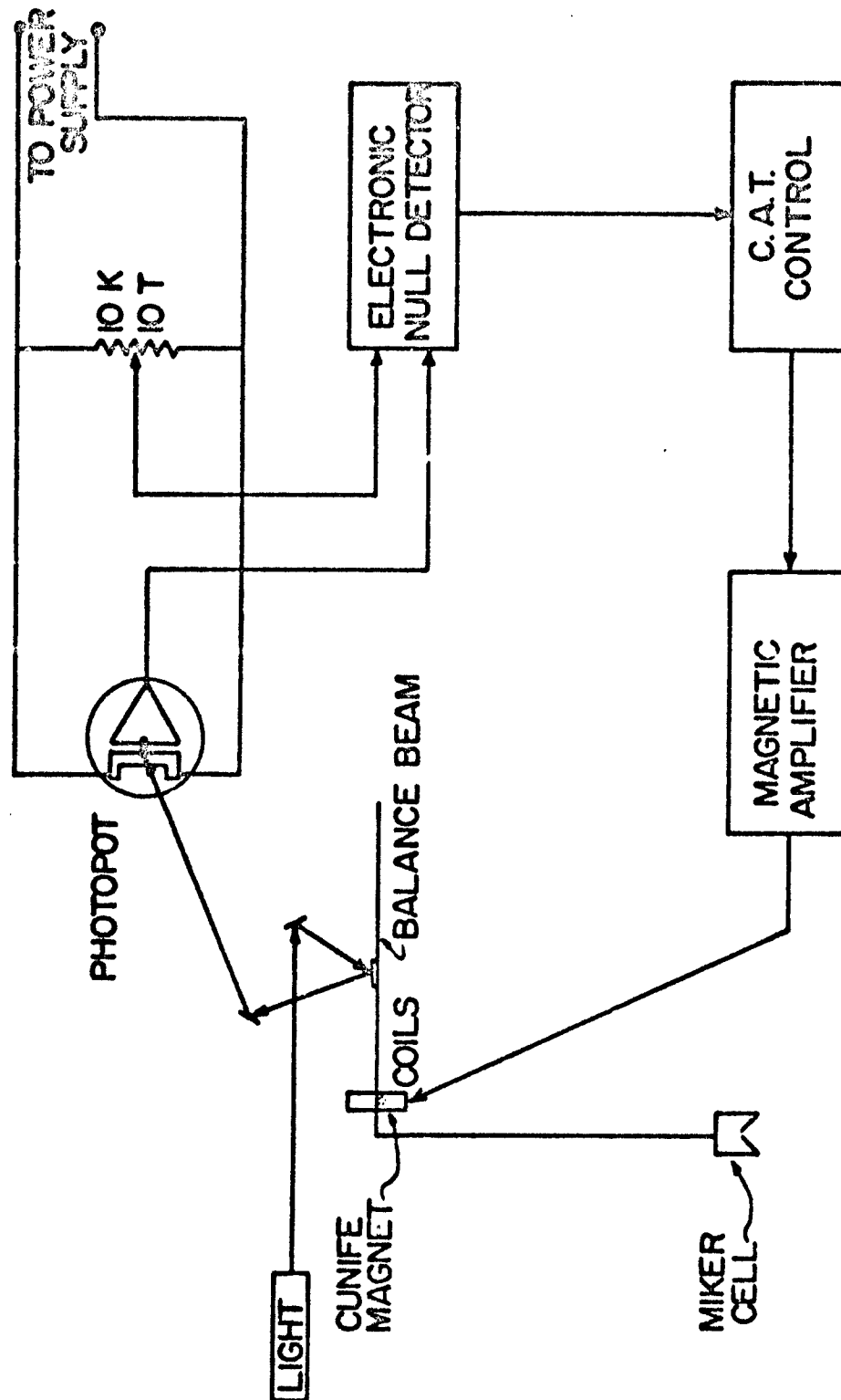


Figure 20. Automatic Control System (Diagrammatic).

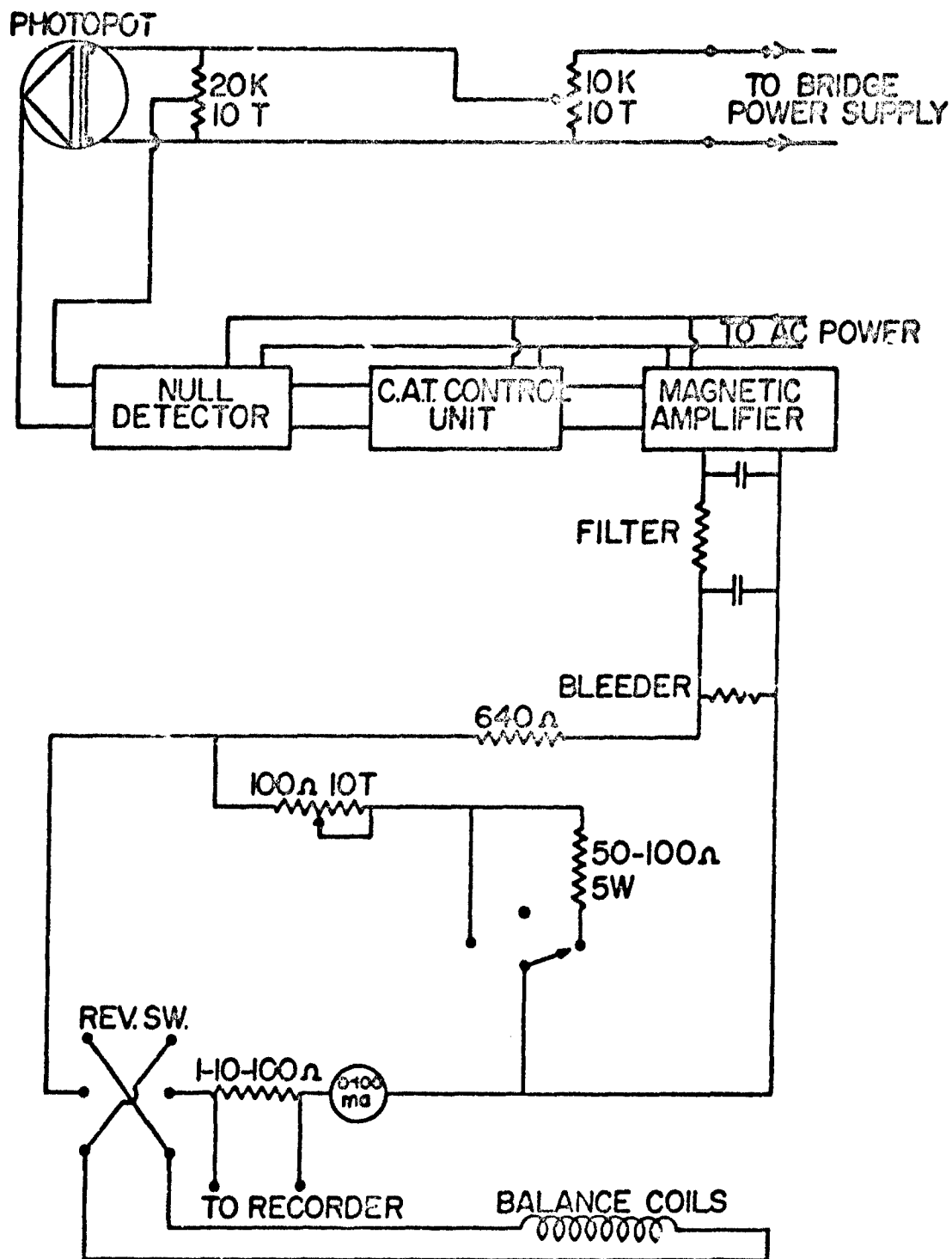


Figure 21. Schematic Diagram of Control System.

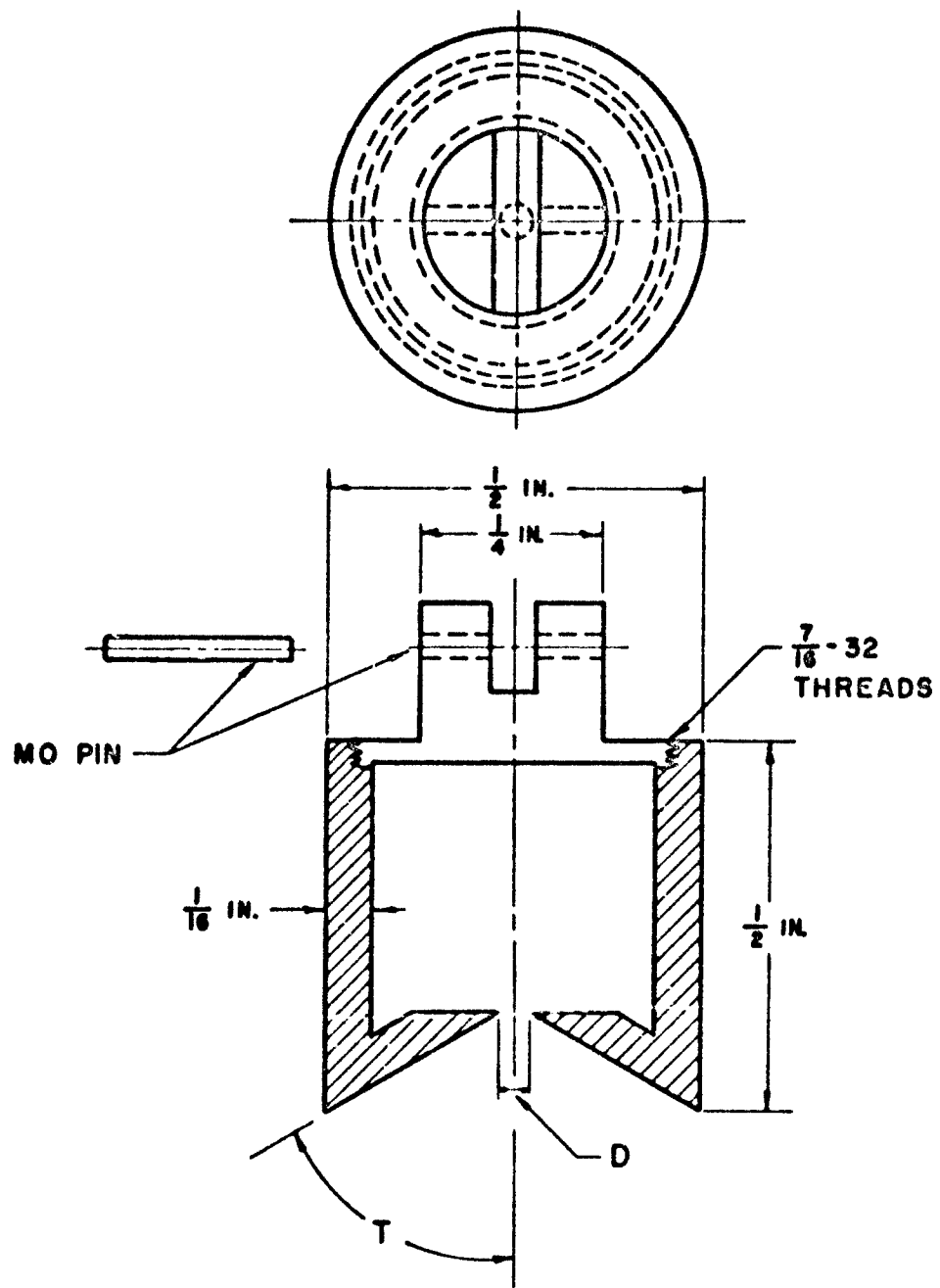


Figure 22. The Miker Cell.

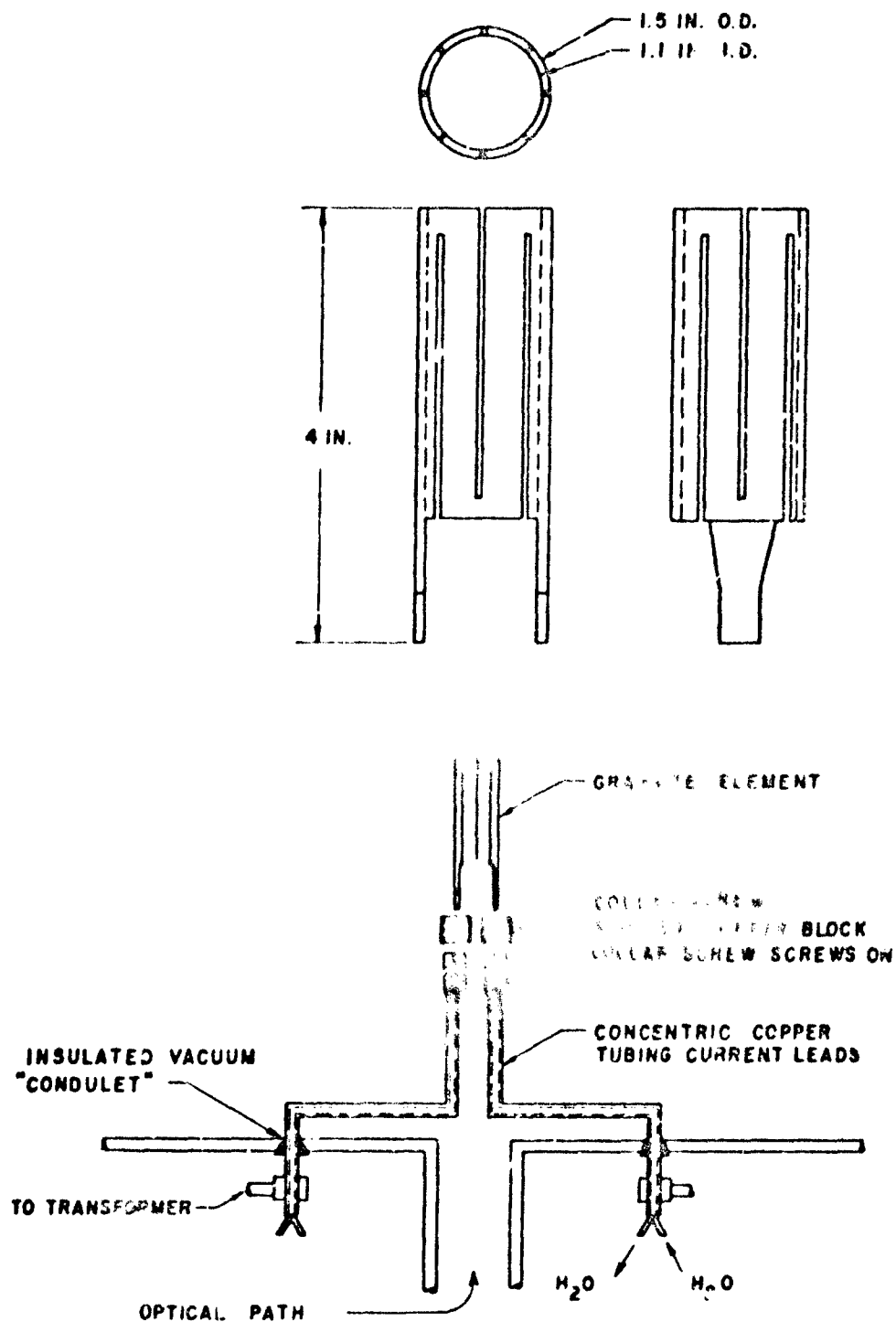


Figure 23. The Heating Element.

of current path, thereby compensating somewhat for the greater heat dissipation from the end regions. The resulting thermal profile (temperature vs. position on heating element axis) will therefore have a flatter maximum, i.e., a longer isothermal region, than it would without this compensation. The heating element is surrounded by a single-thickness, cylindrical radiation shield (not shown). Both molybdenum and tantalum were employed as shielding materials.

The slots in the heating element are spaced so that the current path through the heating element is approximately noninductive; hence, any possible inductive interaction with the Miker cell is made quite small.

The two legs of the heating element fit tightly into rectangular slots milled in solid copper cylinders. The cylinders rest on threaded brass plugs and are firmly held by threaded collars which screw onto the brass plugs. This arrangement allows small "x-y" adjustments of alignment of the heating element. Each brass plug is silver-soldered to a 0.5-in.-diameter copper tube, through which cooling water flows to the plug; the cooling water flows out through an 0.25-in. copper tube which is inside the 0.5-in. tube. The water-cooled copper tubes also serve as electrical lead-ins through which low-voltage ac power is supplied.

Electrically insulated connections through the vacuum chamber wall are achieved with Condulet connectors (Figure 23). The Condulet connectors also allow radial and vertical adjustment of the heating element. Outside the vacuum chamber insulated copper cable connects the copper tubes with the transformer; polyethylene tubing is attached to the copper tubes to achieve electrical insulation from the water and drain lines.

Power to the furnace is adjusted by a 220v Variac which controls the input to the 4 kv-a, 10v transformer. No special regulation or control has been employed. The heating element has been operated for a total of several hundred hours at temperatures up to 1500°C; there is no discernible deterioration in any furnace component.

8. The Vacuum System: The main features of the vacuum system appear in Figure 24. Basically the system consists of a furnace chamber, a

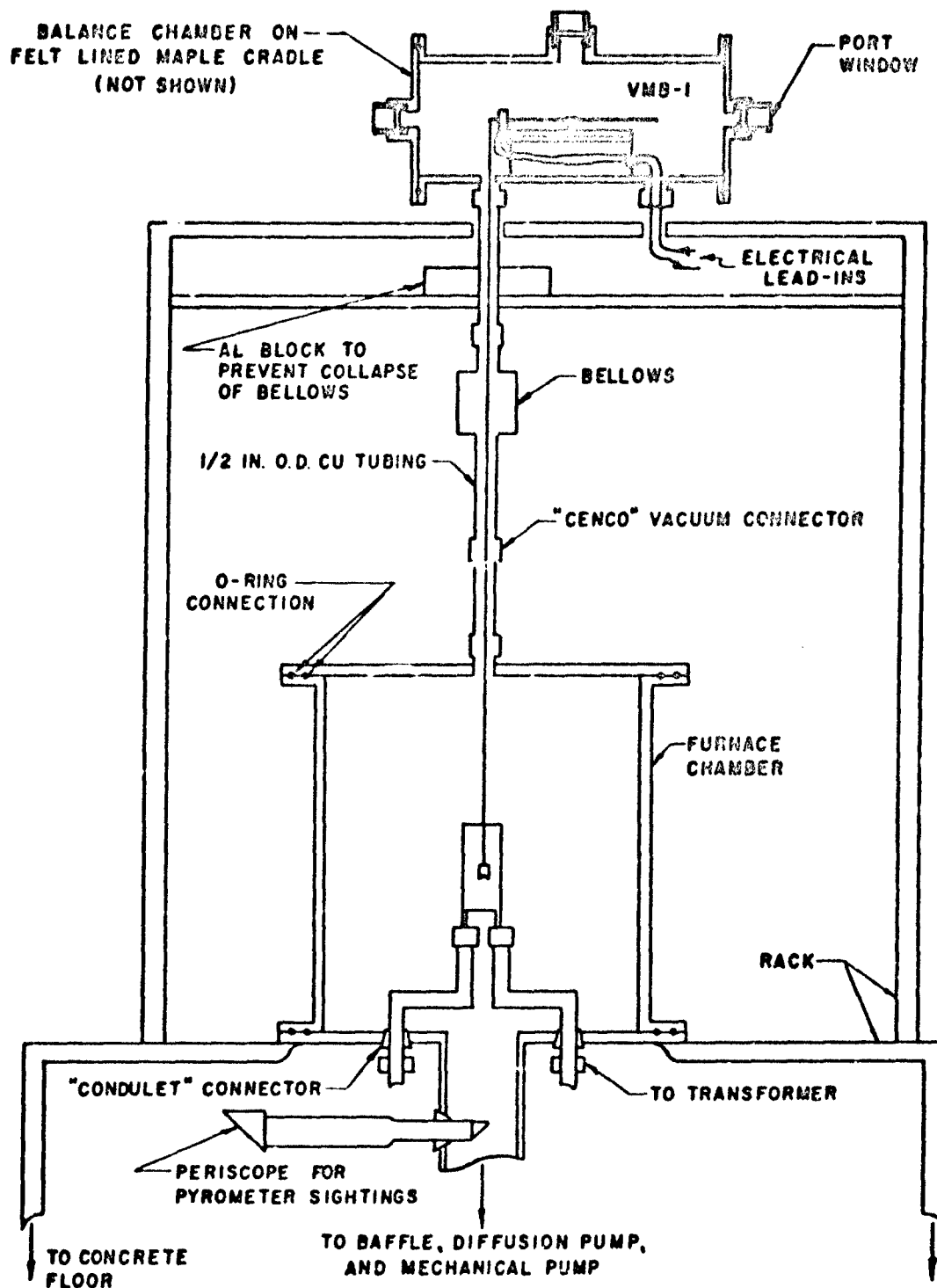


Figure 24. The Vacuum System.

balance chamber, and connecting tubing. The position of the heating element is shown for clarity. The balance chamber was constructed from brass tubing 12 in. in length, 6 in. i.d., and 6.5 in. o.d.; flanges with O-ring grooves are silver soldered to each end. The ends are 0.38 in. brass plates and are secured to the balance chamber flanges by bolts. Each end plate has a window of rather common design--a quartz disc, 2 in. in diameter and 0.25 in. thick, is pressed against a rubber O-ring mounted in an O-ring groove. There is a similar window in the top of the chamber. The windows at the ends permit observation of the balance. The one at the top transmits a light beam to and from the mirror on the balance beam. The balance chamber is seated in a felt-lined maple cradle, which rests on a table constructed from angle iron and 0.75-in. plywood.

The vacuum connection between the two vacuum chambers consists of three sections which are coupled with Cenco vacuum connectors. The middle section is a flexible brass bellows which not only absorbs vibrations but also provides an entrance to the furnace chamber for transferring cells. Disconnection of the Cenco connector which couples the furnace chamber lid to the connecting tube permits the bellows to be collapsed, which provides working room to make or break the hook connection in the balance suspension.

The steel furnace chamber is 12 in. high and 12 in. in diameter. A 4-in. diameter outlet at the center of the base plate makes connection to the pumping system, which consists of a water-cooled baffle and a MCF-300 oil diffusion pump backed by a Welch Duo Seal mechanical pump. The mechanical pump was connected to the diffusion pump by 2-in. diameter rubber tubing which was found to be an excellent vibration absorber. A stout cord connected tautly from the middle of the rubber tubing to the steel frame which supports the entire system improved the damping of vibrations from the mechanical pump.

9. Temperature Measurement: Pyrometer sightings directly into the bottom of the Miker cell are highly desirable since the Miker cell is an excellent approximation to a black body and emissivity corrections are then unnecessary.

The periscope arrangement which was constructed to permit pyrometer

sightings directly into the Miker cell is depicted in Figure 25. A right-angle prism is attached by epoxy adhesive to each end of a Pyrex tube. The vacuum connection is a large Condulet connector. The inner prism is protected from effusing vapors, except during pyrometer sightings, by a cylindrical shield fashioned from 0.001-in. thick tantalum sheet. The shield is attached to beryllium-copper tubing which has a Cunife magnet soldered to one end. The tubing is contained in the Pyrex tube and can be moved by means of the external magnet as indicated. This device operates satisfactorily.

A Model 8622-C optical pyrometer has been used. This instrument was compared frequently via a tungsten strip lamp with a similar instrument which has been certified by the National Bureau of Standards.

C. EXPERIMENTAL RESULTS

The automatic control system for VMB-1 described in the preceding subsection is a recent modification and vaporization data have not yet been obtained with it. We report here data which were obtained with visual observation through a telemicroscope of the balance beam position and manual adjustment of the coil current.

1. Microbalance Calibration: The microbalance was calibrated with a set of weights which were made by cutting suitable lengths of small-diameter tungsten wire. The mass of the individual calibrating weights was determined (± 0.02 mg) with a Sartorius-Werke semi-microbalance. The calibration procedure consisted of adjusting the current through the coils to bring the balance beam to null position, adding a calibrating weight, and readjusting the current to return the beam to null. The coil current was adjusted manually; balance beam position was observed with the telemicroscope.

The anticipated source of largest error was possibly unknown shifts of null point, which might be caused by inadvertent mechanical disturbance of the balance during addition or removal of a weight. It was therefore required, as a condition for satisfactory calibration, that the initial null point be reproduced after each weight had been added to the beam and subsequently removed.

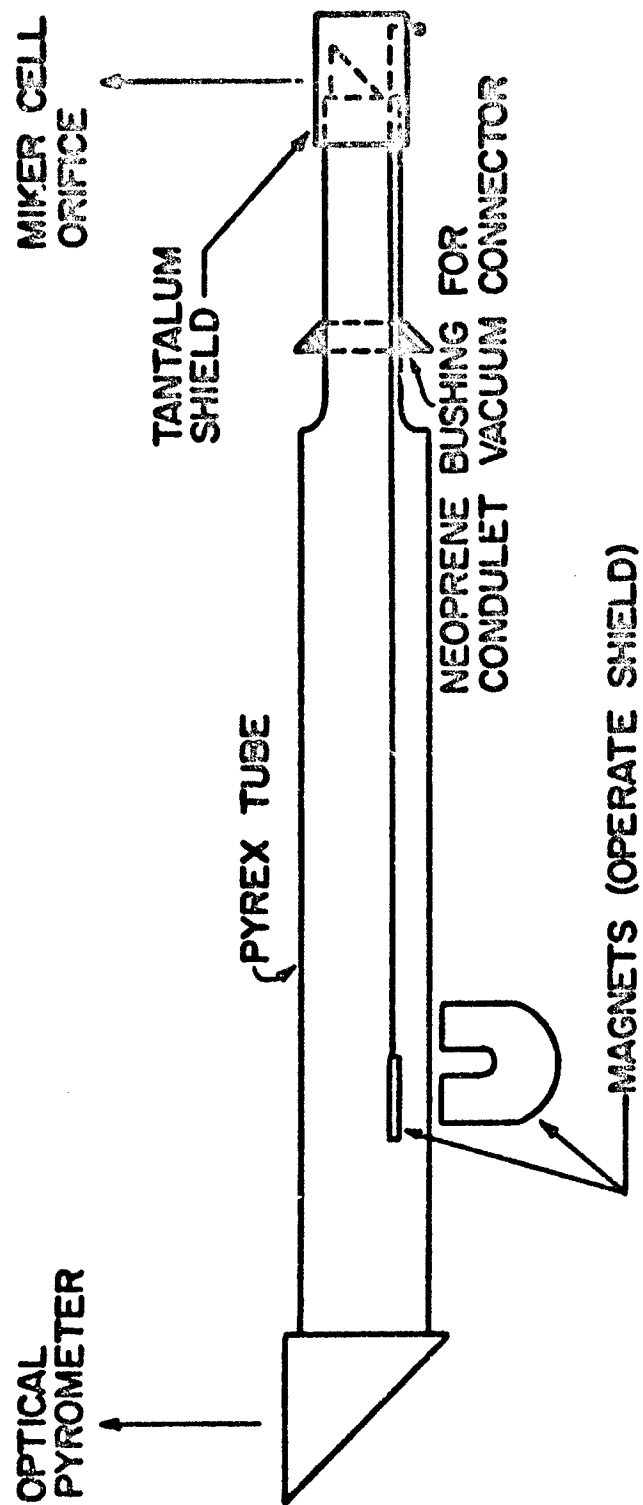


Figure 25. Prism Arrangement for Pyrometric Sightings into the Miker Cell Orifice.

The results of the calibration are given in Table 2; a plot of these data in Figure 26 shows the relation between suspended mass and coil current to be linear over the available current range. The slope of the calibration curve in Figure 26 is 0.289 mg/ma. A least squares determination of the slope from the data in Table 2 gives a value of 0.2883 mg/ma. The solid circles in Figure 26 were determined after the microbalance had been in operation for eleven months.

A graduated reticle in the eyepiece of the telemicroscope was calibrated with the result: 1 scale division = $120 \mu a \times 0.2883 \mu g/\mu a = 34.6 \mu g$. The smallest beam displacement readily detectable with the telemicroscope corresponds to about 0.1 scale division or about $3.5 \mu g$. The resolution of the balance in the measurements reported here must therefore be considered as about $\pm 4 \mu g$, but it should be emphasized that this figure is a direct result of the use of a rather low-powered (approx. 30x) telemicroscope, and that photo-detection of beam motion should improve the resolution by at least a factor of ten.

2. Buoyancy Effects: The effect of buoyancy is readily calculated. The desired result of the calibration is a value for the constant c in the equation

$$dm = c dI \quad (11)$$

in which I is the coil current which compensates for the absolute mass m of the wire weight. The apparent mass m' in air is related to the absolute mass m by

$$m' = m - m (\rho_a / \rho_w)$$

or, with negligible error,

$$m = m' + m' (\rho_a / \rho_w), \quad (12)$$

in which ρ_a is the density of air (0.0012 g/cm^3 at 25°C and 1 atm) and ρ_w is the density of the wire weight (19.3 g/cm^3 for tungsten).

TABLE 2
CALIBRATION DATA FOR MICROBALANCE

Mass of Wire Weight, mg	Compensating Current Through Coils, ma
0.40	1.983
0.87	3.530
1.13	4.438
2.01	7.680
3.64	12.502
5.09	18.600
6.20	22.180
7.49	26.516
8.89	31.940
9.41	34.044
15.83	56.25
18.02	63.12
19.85	69.20
21.66	75.26

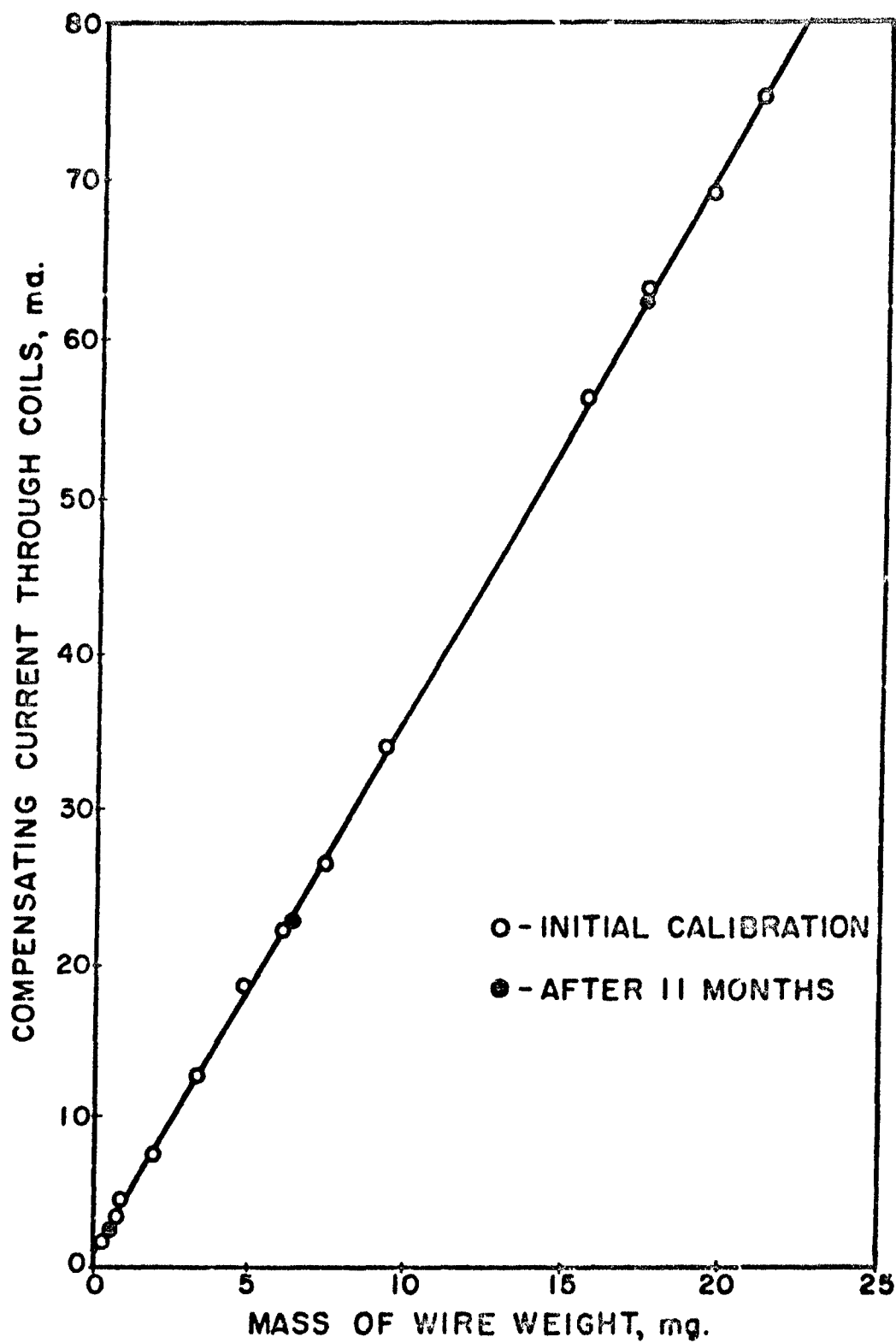


Figure 26. Microbalance Calibration Curve.

Substitution of equation (12) into (11) yields

$$c = (dm'/dI)(1 + \rho_a/\rho_w) \quad (13)$$

From the data given above the term ρ_a/ρ_w has the value 6.2×10^{-5} and is completely negligible in the evaluation of c . It follows that buoyancy effects are negligible. Furthermore, any constant asymmetric buoyancy effects which are present during calibration in air and which are then removed during operation in vacuum do not influence the calibration, but merely shift the zero-point of the mass vs current curve.

3. Weighing Range of VMB-1: From the available current range of about 80 ma, it is apparent that mass changes totaling about 23 mg can be determined. The available range, however, is actually twice this value, or about 46 mg, because the direction of the coil current can be reversed. It is possible to begin a series of runs with maximum current, say +80 ma, so that loss of mass by the cell requires a decrease in the coil current; then, when the coil current is decreased to zero, the current direction is reversed and the series of runs continued until the other end of the current range (approx -80 ma) is exhausted. After the full range of about 160 ma is exhausted, the balance is retared by opening the off-sample side of the balance chamber and adding or subtracting tare wires as necessary. This simple operation makes the entire current range available again, and determinations may be continued without disturbing the cell.

4. General Operating Procedure. All Miker cells, before being charged with sample, were heated to constant weight at about 1500°C. The pressure of the furnace chamber was usually about 1×10^{-6} torr during heating. No heating was performed if the furnace pressure rose above 5×10^{-5} torr. Simultaneous determination of the pressure in the balance chamber showed that in the early stages of pumping it lagged about one order of magnitude behind the pressure in the furnace chamber and on extended pumping slowly approached that of the furnace chamber.

After the preliminary heating, the empty cell was removed from the vacuum system, charged with sample material, and returned to the vacuum system. The balance tare was then adjusted to provide an adequate current range. Each new sample was heated for a short period at temperatures higher than the experimental range of interest.

No special treatment was given the various samples; the following specifications are given by the suppliers:

Sn 99.99% Lot No. 1537 (J. T. Baker, Phillipsburg,
New Jersey)

Ag 99.99% Lot No. 791231 (Fisher Scientific Company,
2920 Shotts St., Ft. Worth,
Texas 76101)

Au 99.95(+) (J. Bishop & Co., Platinum Works, Malvern,
Pennsylvania)

CaF₂ 99.994% Lot No. 771004 (Fisher Scientific Company,
2920 Shotts St., Ft. Worth,
Texas 76101)

The coil current was recorded continuously with a Model MR Recorder. To obtain a null reading, the coil current was adjusted in a direction which caused the beam to approach null as effusion occurred. At the instant the beam was at null, the standardization button on the recorder was depressed. This produced a spike on the recorder tracing, and, since the chart speed was known, recorded both the current and the time of the null. Some minutes later, the coil current was again adjusted as before and the procedure repeated. In this manner there were obtained for each run a series of spikes which provide data for a plot of current vs. time and therefore of mass vs. time. During the entire procedure the balance beam never touched the rest stops.

Optical pyrometer readings were taken intermittently during a run. At no time was the temperature observed to fluctuate from its initial steady state value; the straight lines obtained from a plot of coil current vs. time give direct confirmation of constant temperature conditions.

At the instant of recording the last null determination, a switch was thrown which de-energized the heating element. After the disappearance of the recoil effect, the coil current was adjusted to return

the beam to null and was recorded on the recorder chart paper along with the other data.

The various parameters of the Miker cells used for the data reported below are given in Table 3.

5. Empty Cell Behavior. Initial testing of the apparatus and the Miker technique was made with a graphite cell containing silver. The values obtained in the first five runs for the molecular weight of silver were: 6.8, 2.5, 22, 146, 104. When an empty cell was substituted for the one containing silver, the apparent recoil forces, as measured by the apparent difference in weight of the cell when hot (1200°C) and when cool (400°C), were quite erratic, but did exhibit a trend with temperature. These apparent recoil forces for empty cells were eliminated by removing a molybdenum disc (radiation shield) which had been attached to the balance suspension wire about 2 in. above the heating element. The spurious recoil forces for empty cells apparently resulted from a radiometer-type effect (the bottom of the molybdenum disc was exposed to radiation from the furnace and was therefore hotter than the top surface), or from a larger number of molecules, with a higher average speed, arriving at the bottom of the disc from the furnace volume as compared with those arriving at the top of the disc from the cool walls of the vacuum chamber.

After the molybdenum disc was removed from the suspension wire, an empty cell was again tested for a recoil effect. Within the resolution of the telemicroscope ($\pm 4 \mu\text{g}$), no recoil force was detected. This observation was repeated with other cells at temperatures up to about 1500°C . Furthermore, no observable balance motion occurred during the sequence: (1) balance initially at the null point with a degassed, empty cell suspended into the furnace at a temperature of 1300°C ; (2) switch thrown to de-energize the furnace; (3) furnace and cell cooled for several minutes; (4) switch operated to re-energize the furnace; (5) furnace and cell return to the original temperature. It therefore appears that the spurious recoil forces have indeed been eliminated, and that interactions

TABLE 3
PARAMETERS OF MIKER CELLS

Cell	Used For	Orifice Parameters ^a			Correction Factors ^b	
		L, in.	D, in.	T, deg	W	F
1	Ag	0.127	0.0509	60	0.996	1.12
2	Sn	0.209	0.082	45	0.975	1.16
3	CaP ₂	0.127	0.0635	60	0.996	1.12
5	Au	0.120	0.064	60	0.996	1.11

^aL = length, D = smallest diameter, T = off-axis angle.

^bInterpolated from Table V, Part I of this report¹⁴.

between the cell and the heating element, as reported by Searcy and Freeman³⁶, Sheer³⁷, and Bader³, are not present in this apparatus.

6. Typical Run. Typical of the majority of determinations is CaF_2 Run No. 9, data for which appear in Figure 27. Each point on the curve represents a null determination. In this case, as for most, the rate of effusion can be obtained precisely from only the initial and final null determinations; however, as a safeguard against possible erroneous null determinations and temperature fluctuations, several null determinations were performed in all runs.

From the slope of the curve in Figure 27 the rate of effusion is $6.127 \mu\text{g/sec}$ and since this is a typical result, no special comment applies. In some runs which were begun before a constant temperature was attained, the early part of the current vs. time curve shows clearly the change in the rate of effusion with temperature.

7. Rapid Effusion. At pressures approaching the transition region, i.e., near or above the upper pressure limit of validity of the Knudsen equation, difficulty might be expected in adjusting the compensating current rapidly enough to monitor the effusion and yet retain accurate null determinations. This would be of particular concern for manual control. Often the problem of rapid effusion is eliminated in conventional Knudsen determinations by employing cells with appropriately smaller orifices for the higher temperature ranges. But the convenience and superior experimental technique of using one cell for an uninterrupted series of runs which spans the entire Knudsen range is very appealing. For this reason some runs were made to determine approximately the maximum rate ($\mu\text{g/sec}$) accessible under manual control. Figure 28 shows the results for Ag Run No. 14 at 1458°K ; the rate of effusion ($32.2 \mu\text{g/sec}$) corresponds to a vapor pressure of 2.1×10^{-4} atm, which approaches the transition region. With the same cell, an effusion rate of $0.051 \mu\text{g/sec}$ was measured for Ag at 1150°K . The latter rate corresponds to a pressure of 2.8×10^{-7} atm.

Though reliable rates of effusion can be determined for the rapid effusion, a rather serious error arises for the measurement of

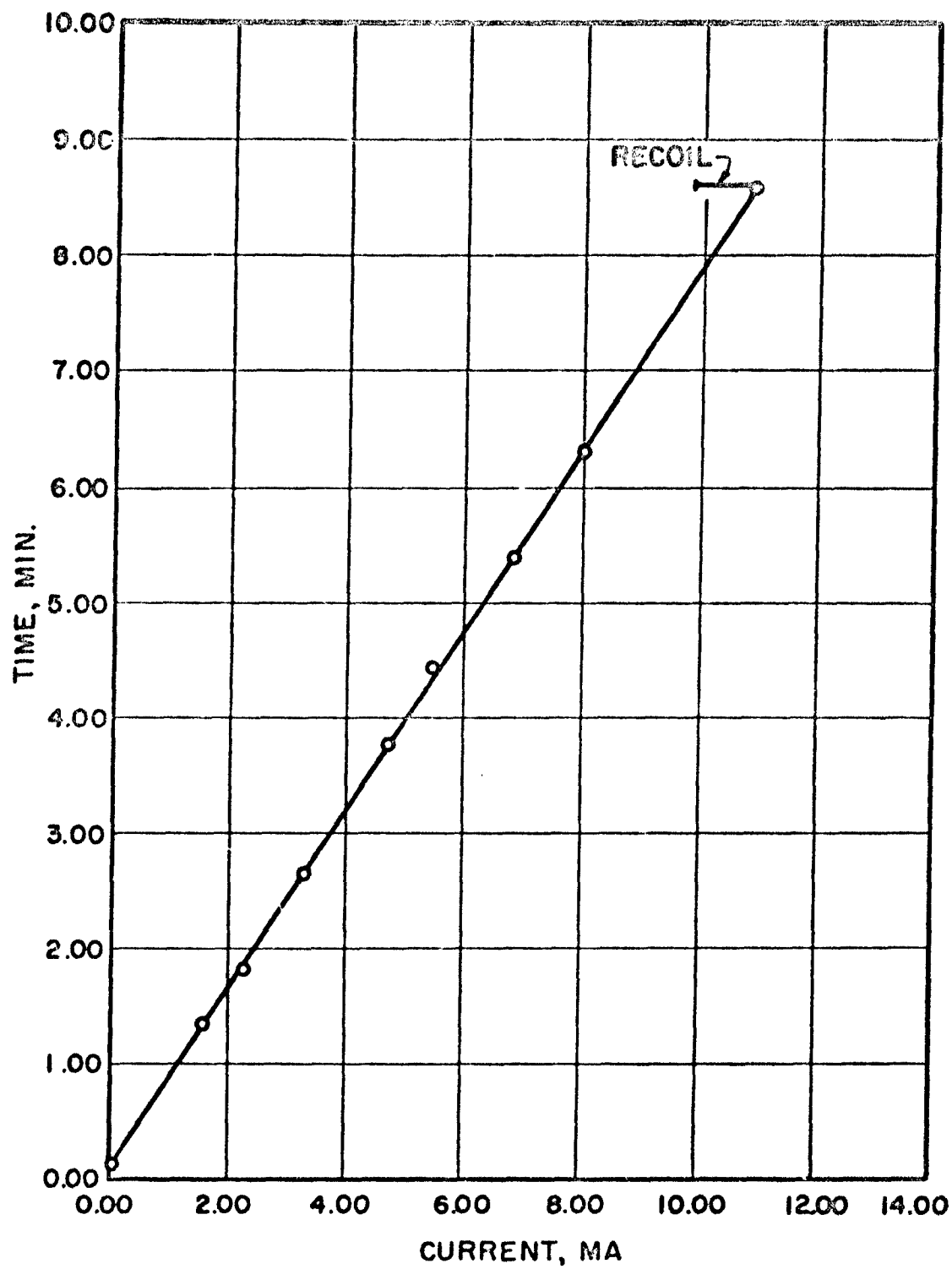


Figure 27. Typical Experimental Data-Calcium Fluoride, Run 9.

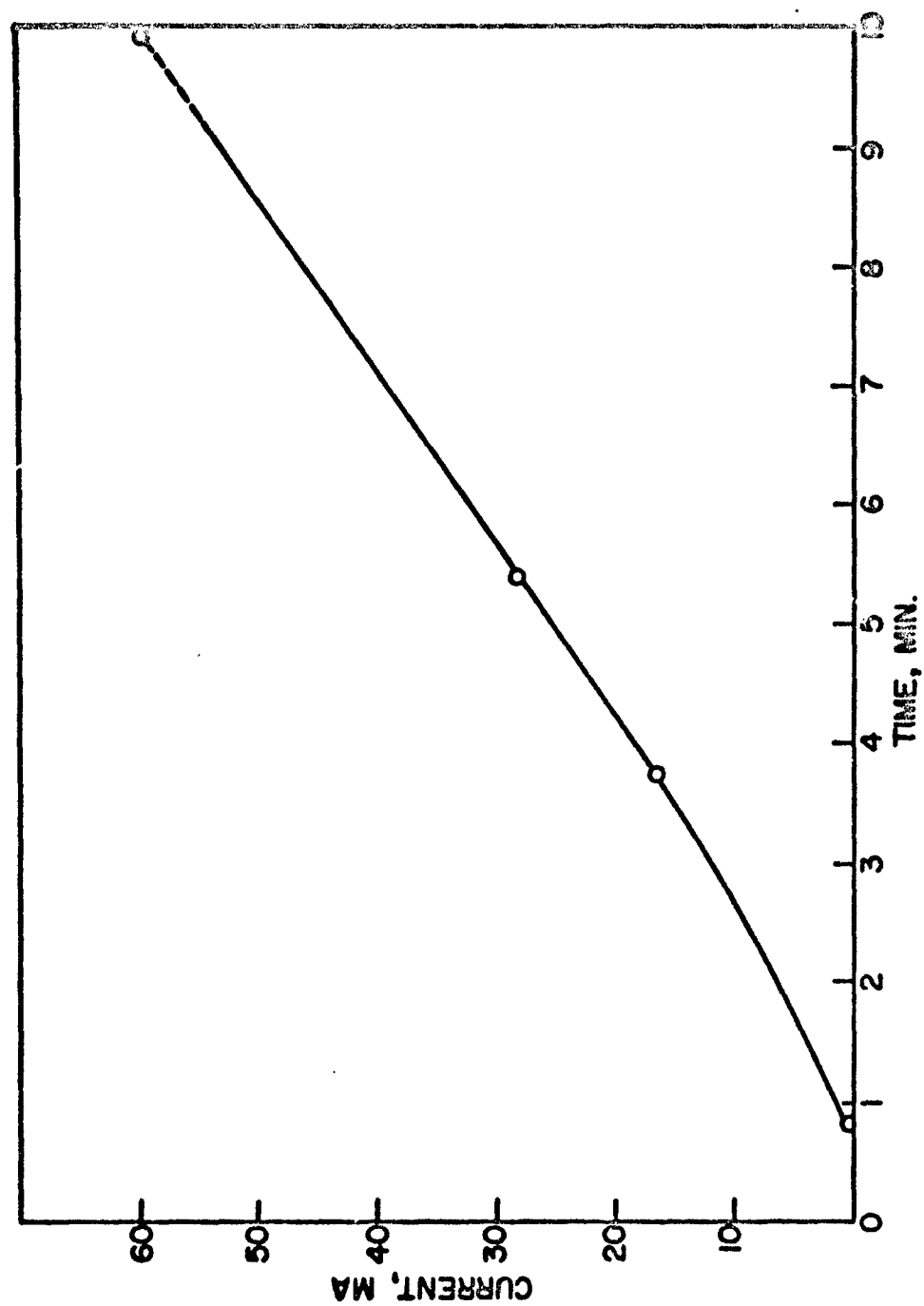


Figure 28. Rapid Effusion - Silver, Run 14.

the recoil force. The null determinations may be described as "running" nulls because the instant at which the balance beam passes through null is recorded. Consequently, if the balance is moving rapidly, as it does for rapid effusion, an appreciable overshoot of the null results. This is not objectionable for the rate of effusion determination; no error is introduced by the overshoot if each null is determined in the same manner. But the last null determination is accompanied by de-energizing of the heating element and the recoil force is measured by the current required to return the balance to null. Thus the overshoot occurs in a direction which reduces the observed recoil force. For slower effusion the balance either approaches null very slowly, or can be impeded by adjusting the compensating current, and no such problem arises. But for rapid effusion under manual control, precise determination of the recoil force becomes a question of the skill of the operator and his ability to impede the rate of approach to null so as to eliminate or minimize the final overshoot.

8. Effect of Sample Surface Area. The effect on the rate of effusion of diminishing surface area of sample is shown in Figure 29; the data for CaF_2 and Au were obtained when the surface area of each sample was about the same as the area of the cell orifice. It is of course desirable to have a large value for the ratio: sample-surface-area to orifice-area. The minimum value of this ratio which assures a constant, steady-state (not necessarily equilibrium) pressure depends on the condensation coefficient of the sample substance¹¹. For similar surface areas, the rate of effusion of gold remains at a constant value while that of calcium fluoride decreases with decreasing sample size; this indicates the condensation coefficient of gold to be nearer unity than that of calcium fluoride, and provides no direct information about the evaporation coefficients.

9. Permeation of Graphite Walls by Gold and Silver Vapors. Other workers have noted that silver vapor¹² and perhaps tin vapor²² permeate some types of graphite. The present experimental system is ideally suited for measuring such permeation. Closed¹⁸ Miker cells were constructed

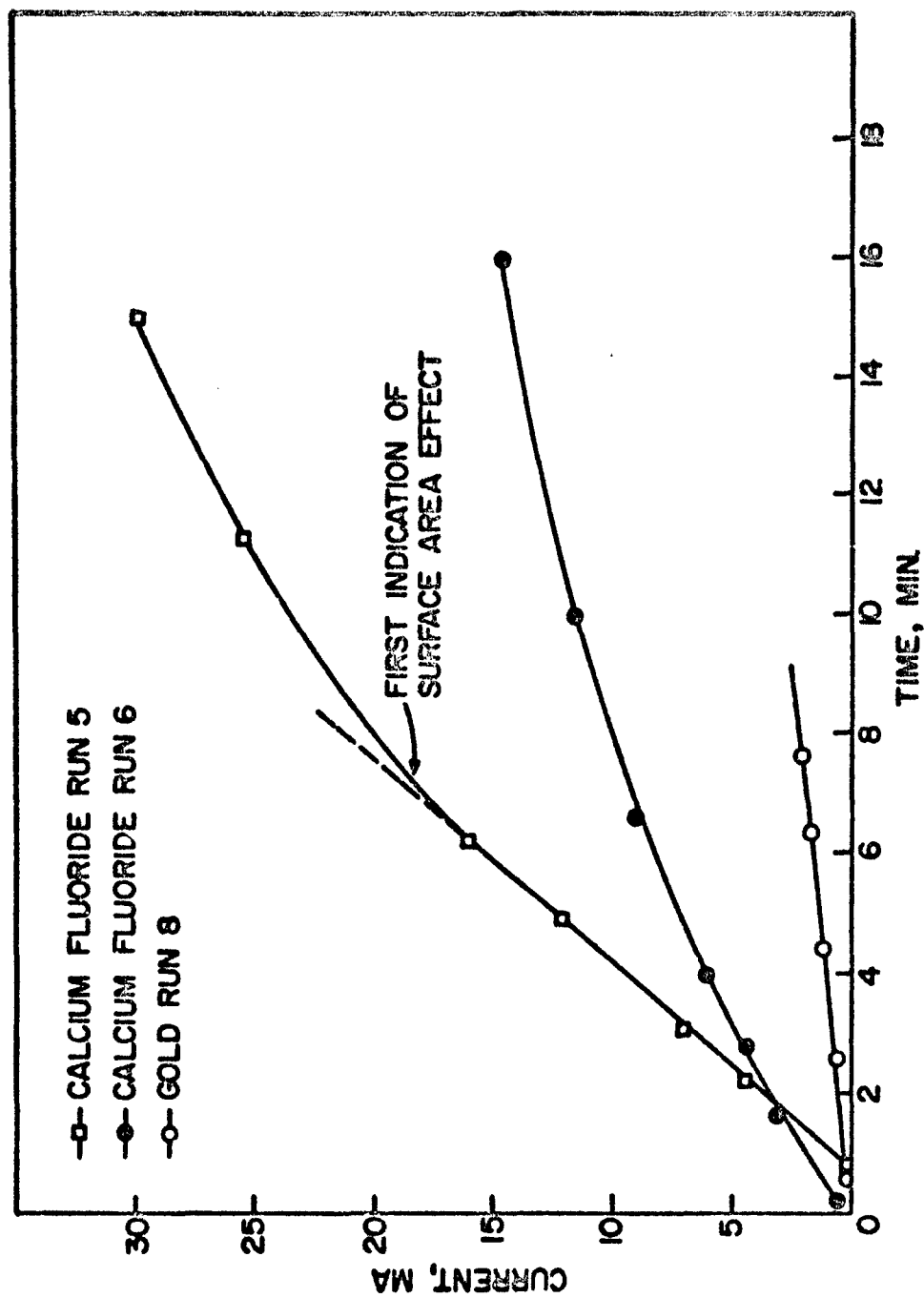


Figure 29. The Effect of Diminishing Sample-Surface-Area on the Rate of Effusion.

to be identical to the normal cell (Figure 22) except that the orifice is replaced by a flat, closed bottom.

The rate of permeation of silver and of gold vapors through the walls of a closed cell was measured and is given in Table 4. At a given temperature the rate of permeation for both silver and gold is (on the average) about 3% of their normal effusion rate at that temperature. The fact that permeation does occur, however, implies that "normal" effusion contains a contribution from permeation. Edwards and Downing¹² have studied this phenomenon and have demonstrated that at least two mechanisms exist by which metal vapors can permeate graphite walls. The vapors may undergo capillary effusion which obeys the Knudsen equation (except that the orifice area is ambiguous), or activated diffusion may occur^{25,4}. The simplest method for distinguishing these mechanisms appears to be to make a Knudsen-type calculation on the permeation data and to compare the results to normal effusion data; if a significant difference is observed in the slopes of $\log \underline{P}_K$ vs. $1/T$ curves, for example, then the permeation occurs by a non-effusion mechanism. If the slopes agree, permeation results from capillary effusion with zero energy of activation.

The workers mentioned above concur that capillary effusion obeys the Knudsen equation except that a simple parameter, usually assumed to be negligibly dependent on temperature, appears in place of the orifice area. If this is true, then permeation data can be tested by applying the Knudsen equation directly, with an arbitrary constant for the unknown parameter. The \underline{P}_K values so calculated bear no necessary relation to actual pressures, but the $\log \underline{P}_K$ vs. $1/T$ plot will have the correct slope. To show this let a' be the unknown parameter for the Knudsen equation. Then from equation (1) and the above discussion we have $a' \underline{P}_K = \dot{w}(2\pi RT/M_K)^{1/2}$; the product $a' \underline{P}_K$ can obviously be calculated from the permeation data. If capillary effusion occurs, we expect a straight line for $\log (a' \underline{P}_K)$ vs. $1/T$, i.e.,

$$\log (a' \underline{P}_K) = A/T + B,$$

or

$$\log \underline{P}_K = A/T + (B - \log a'),$$

TABLE 4
PERMEATION OF CLOSED GRAPHITE CELLS BY GOLD AND SILVER VAPORS

Gold		
Run	Temp., °K	μg/sec
1	1685	0.187
2	1653	0.105
3	1628	0.059
4	1590	0.006
Silver		
Run	Temp., °K	μg/sec
1	1393	0.413
2	1577	11.1
3	1476	2.50
4	1420	1.07
5	1367	0.470
6	1647	22.4

in which the slope is identical to that for normal Knudsen effusion data.

Calculations were performed for the permeation data of Table 4. For convenience a' was assigned numerical values: for the silver closed - cell data a' was assumed to be the orifice area of the Miker cell used with silver; for the gold closed - cell data a' was assumed to be the orifice area (Table 3) of the Miker cell used with gold. Results of these calculations appear as $\log \frac{P}{K}$ vs. $1/T$ plots in Figures (30) and (31).

The permeation data in Figure 30 yield a slope of -15900; the slope from the Miker cell data is -15000. The difference in slope of 900 is insufficient to warrant proposal of a permeation mechanism other than effusion. Edwards and Downing¹² also interpreted slope agreement within 700 to indicate no new mechanism for silver permeation.

The significance of the one anomalous point in Figure 30 is not understood. It is not attributed to scatter in the data. The possibility of a discontinuous change in mechanism exists. This is especially interesting because the same behavior is exhibited by gold (Figure 31). The gold permeation data yield a slope of -24850, and the slope from the Miker data is -19960. The difference of almost 5000 is interpreted as the appearance of a diffusion mechanism, rather than just capillary-effusion.

The slopes given above correspond to $\Delta H_{\text{vap}}/2.303R$; therefore, a value for ΔH_{vap} can be calculated both for diffusion-permeation and for normal effusion. The difference between the ΔH_{vap} values is attributed to the energy of activation for permeation by gold of the graphite cells. The resulting value for gold, 22.5 kcal/mole, is comparable to values usually found for the diffusion of gases through metals and solids^{25,4}.

Edwards and Downing have pointed out that their results on copper permeation of graphite walls by activated diffusion imply that copper must be to some extent soluble in the graphite. The same comments appear applicable to the present work with gold, especially in light of previous observations on the gold-graphite interaction⁵.

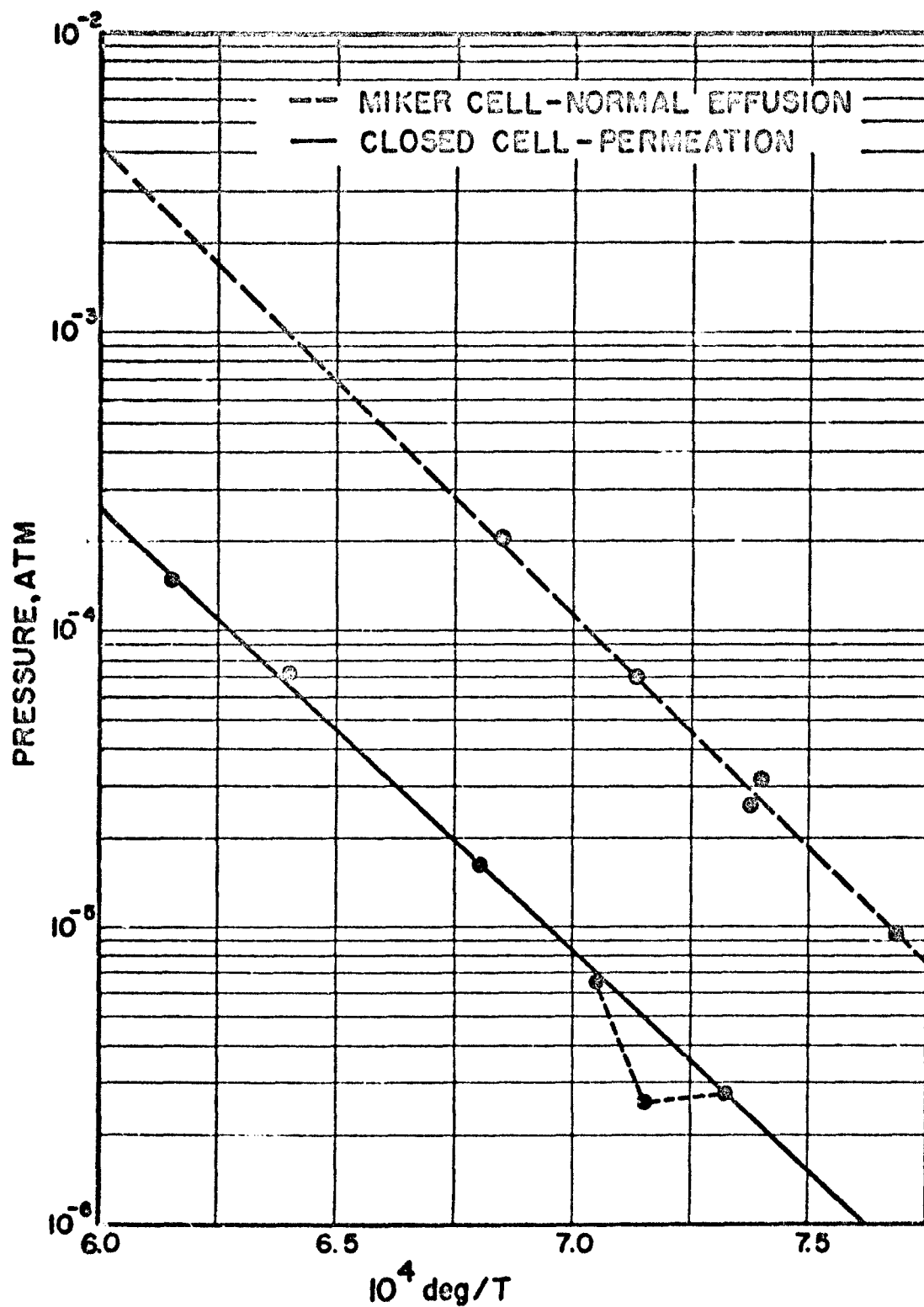


Figure 30. Normal Effusion and Closed-Cell Permeation, Silver.

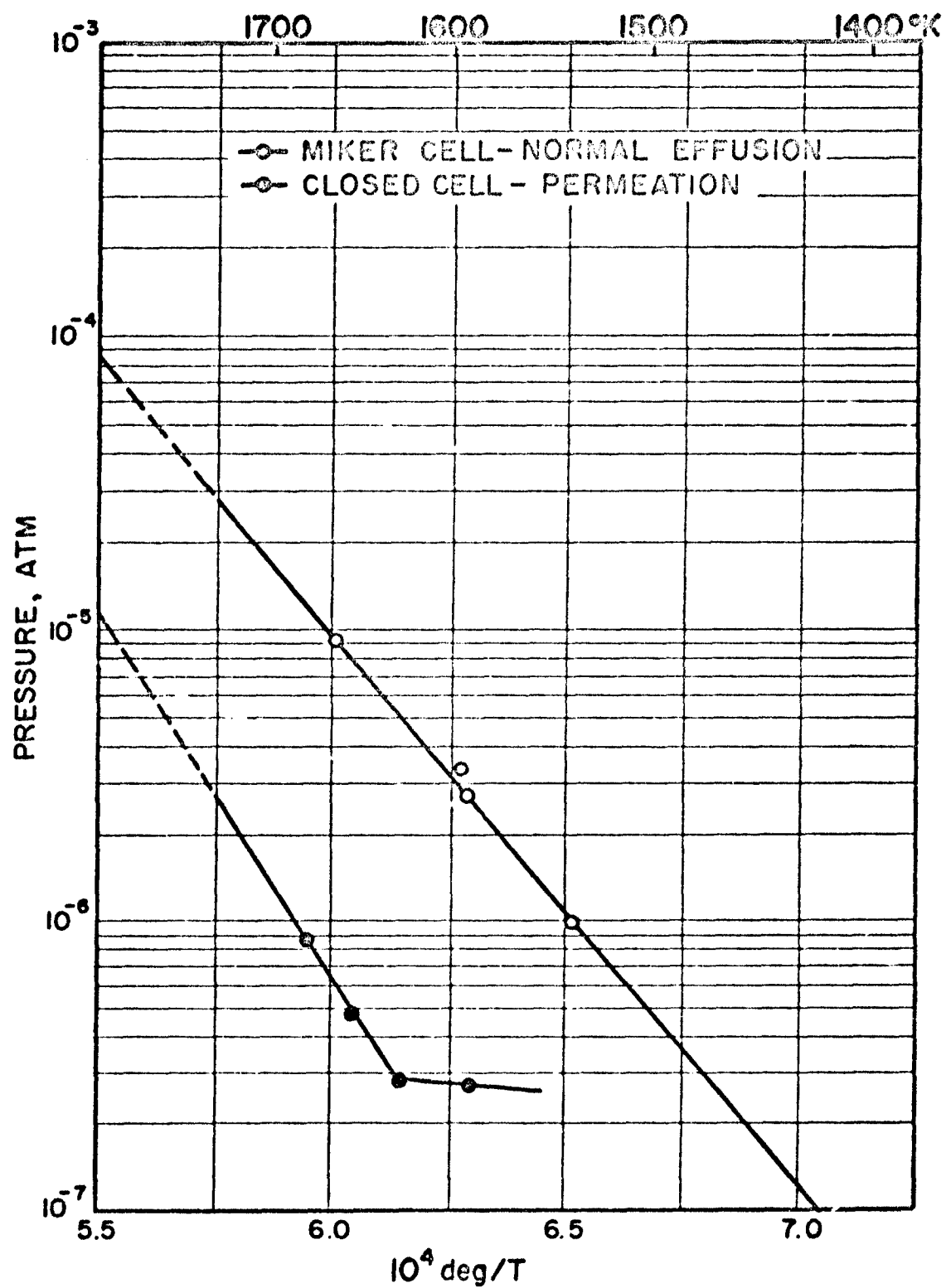


Figure 31. Normal Effusion and Closed-Cell Permeation, Gold.

10. Experimental Cooling Data. Application of the results of subsection VI. D. to correction of recoil force data requires knowledge of the rate of cooling of the cell after the furnace is de-energized. Therefore, cooling data were obtained for a typical cell. Temperature measurements were made with a manually-operated optical pyrometer: the results must be considered as good approximations rather than precise determinations. The data, which are given in Table 5, were plotted as (see subsection D): $\ln T$ vs. t ; $\ln(T - T_f)$ vs. t ; and T^{-3} vs. t . As expected, the experimental points lie nearest the theoretical straight line in the T^{-3} plot, which, of course, indicates that cooling occurs primarily by radiation. From the slope of the "best" straight line through the experimental points, the cooling constant k_r of equation (30) was found to be $1.04 \times 10^{-12} \text{ degree}^{-3} \text{ sec}^{-1}$.

11. Vapor Pressures from Rate of Effusion. A number of measurements have been made of the rate of effusion of silver, calcium fluoride, and gold vapors from Miker cells; during these measurements no attempt was made to measure recoil force. The observed rates of effusion and the calculated pressures are given in Tables 6, 7, and 8, and the typical $\log P_K$ vs. $1/T$ plots appear in Figures 32, 33, and 34. From the vapor pressure data in Tables 6 and 8, the heats of sublimation of silver and gold have been calculated; the details are given in Tables 9 and 10.

The results for all three materials are in rather good agreement with those of other workers. The heat of sublimation of silver calculated by the third law method (Table 9) shows little, if any, trend with temperature and the average value, 68.50 ± 0.44 (average deviation) kcal/mole, agrees well with selected values given by Hultgren²⁶ 68.10 ± 0.30 , by Nesmeyanov³², 68.1, and by Stull and Sinke⁴⁰, 68.4. The vapor pressures given in Table 7 for calcium fluoride are in fair agreement with those of Schulz and Searcy³⁵ who also used an effusion technique and graphite cells. The discrepancy between the effusion data and the Langmuir data obtained by Blue, et. al.⁷ for calcium fluoride may arise from condensation-evaporation coefficient effects (see Surface Area Effects, above). The data for gold (Table 8, Figure 34) are in reasonable agreement with previous data obtained in our laboratory^{5,21}, but the slope of the log

TABLE 5
EXPERIMENTAL COOLING DATA FOR A TYPICAL MIKER CELL

Trial	T, °K	t, sec
1	1679	0
	1579	17
	1453	40
	1162	127
2	1677	0
	1577	17
	1487	31
3	1676	0
	1323	68
	1243	96

TABLE 6
VAPOR PRESSURE OF SILVER FROM RATE OF EFFUSION

Run	Temp., °K	Rate of Effusion, \dot{w} , $\mu\text{g}/\text{sec}$	Pressure*, $P_K/10^{-6}\text{atm}$
10	1378	9.62	58.7
11	1325	2.94	17.6
12	1293	1.94	11.5
13	1228	0.301	1.74
14	1458	32.5	203.
15	1298	16.4	9.15
16	1345	5.15	31.0
17	1255	0.953	5.55
18	1395	10.9	68.0
19	1248	0.558	3.26
20	1223	0.348	2.00
21	1185	0.157	0.892
22	1150	0.051	0.284
23	1350	4.22	25.0
24	1323	2.52	15.2
25	1290	1.47	8.70
26	1240	0.511	2.97
27	1200	0.207	1.18

*Calculated via equation (1) with cell parameters from Table 3
and with $\bar{M}_K = 107.88$.

TABLE 7
VAPOR PRESSURE OF CALCIUM FLUORIDE FROM RATE OF EFFUSION

Run	Temp., °K	Rate of Effusion, \dot{w} , $\mu\text{g/sec}$	Pressure*, $P_K/10^{-6}\text{atm}$
1	1668	9.20	47.5
2	1648	5.92	30.4
3	1600	3.26	16.5
4	1568	1.73	8.65
5	1535	1.07	5.30
6	1520	0.68	3.35
7	1503	0.45	2.20
8	1488	0.25	1.22
9	1463	0.18	0.87

*Calculated via equation (1) with cell parameters from Table 3
and with $\bar{M}_K = 78.1$.

TABLE 8
VAPOR PRESSURE OF GOLD FROM RATE OF EFFUSION

Run	Temp., °K	Rate of Effusion, \dot{w} , $\mu\text{g/sec}$	Pressure*, $P_K/10^{-6}\text{atm}$
26	1673	3.72	12.5
27	1652	2.82	9.44
28	1625	1.72	5.68
29	1597	1.07	3.50
30	1585	0.89	2.91
31	1569	0.70	2.30
32	1563	0.56	1.83
33	1548	0.42	1.36
34	1533	0.32	0.98

*Calculated via equation (1) with cell parameters from Table 3
and with $\underline{M}_K = 197.2$.

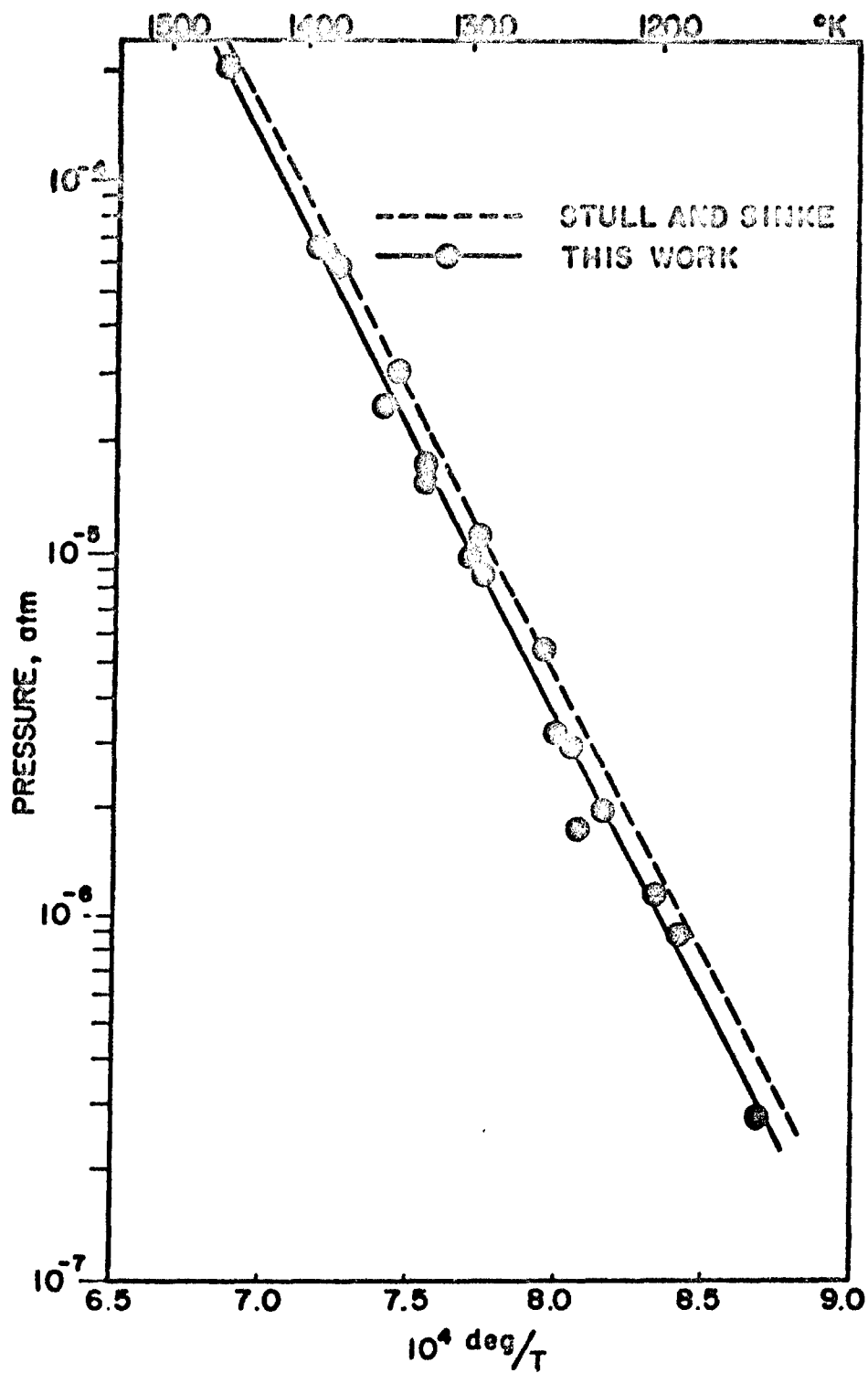


Figure 32. Vapor Pressure of Silver.

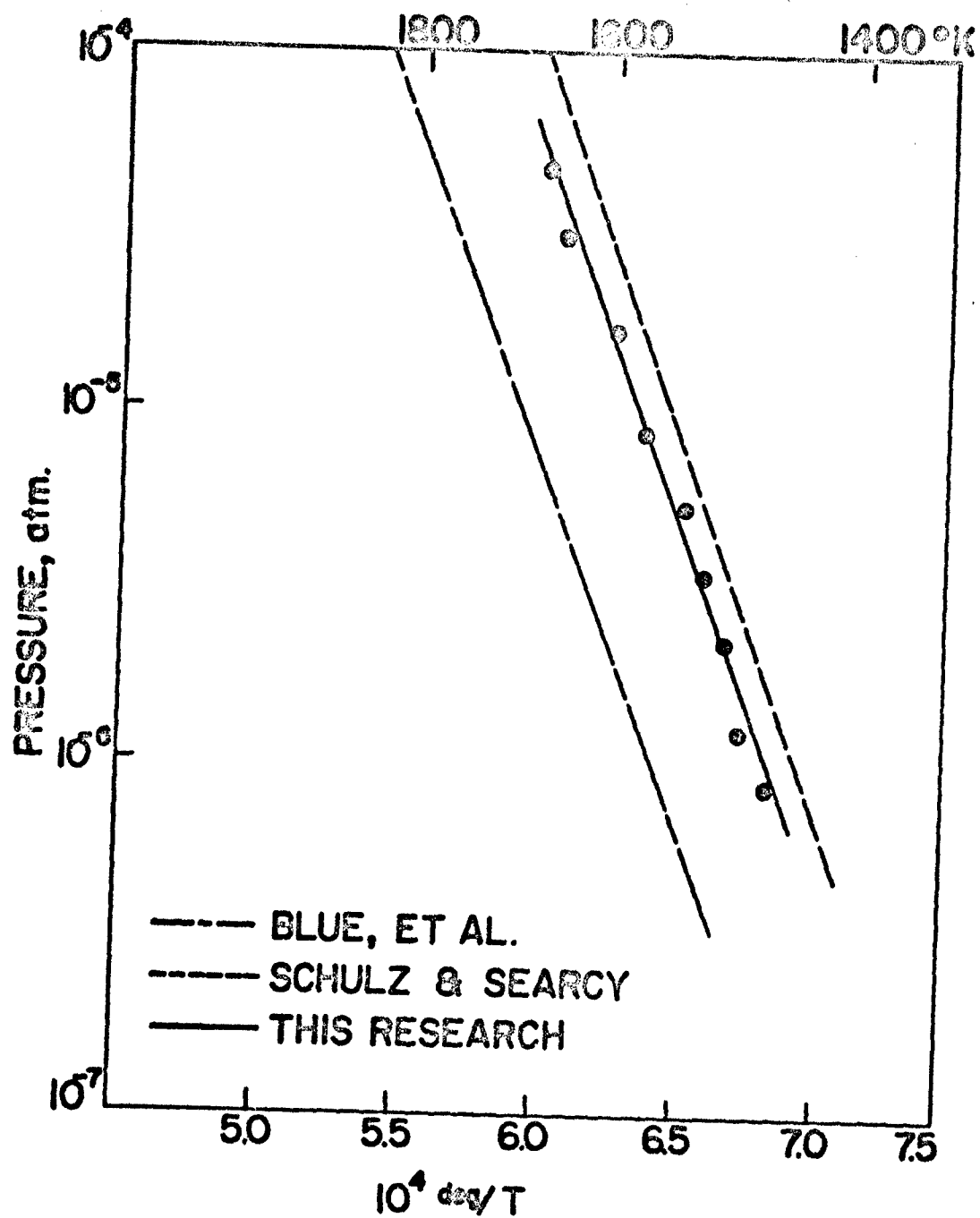


Figure 33. Vapor Pressure of Calcium Fluoride.

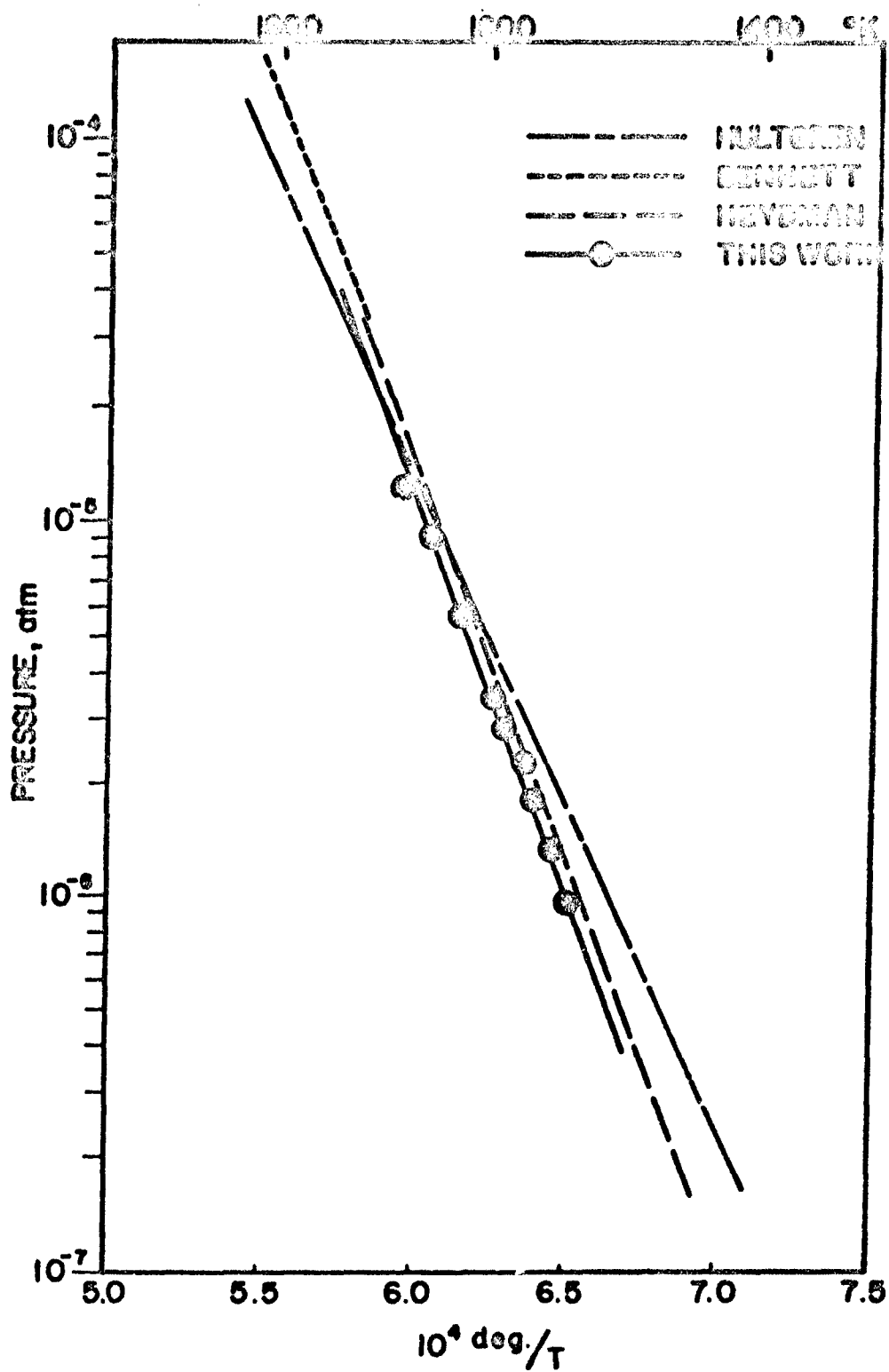


Figure 34. Vapor Pressure of Gold.

TABLE 9

HEAT OF SUBLIMATION OF SILVER FROM RATE OF EFFUSION

T	$\Delta F^{\circ}/T$	$-fef(g)$	$-fef(l)$	$\Delta H_{298}^{\circ}/T$	ΔH_{298}°
$^{\circ}K$		cal deg ⁻¹ mole ⁻¹			kcal mole ⁻¹
1378	19.36	45.05	15.27	49.14	67.72
1325	21.75	44.90	14.96	51.70	68.50
1293	22.60	44.81	14.80	52.61	68.03
1228	26.35	44.60	14.46	56.49	69.37
1458	16.89	45.23	15.66	56.50	67.80
1298	22.92	44.82	14.83	52.92	68.69
1345	20.73	44.95	15.07	50.51	67.94
1255	24.04	44.68	14.59	54.14	67.95
1395	19.06	45.08	15.35	48.80	68.08
1248	25.10	44.66	14.56	55.21	68.90
1223	26.07	44.59	14.43	56.24	68.78
1185	27.68	44.46	14.26	57.88	68.59
1150	29.95	44.35	14.08	60.23	69.26
1350	21.05	44.96	15.10	50.92	68.74
1323	22.04	44.90	14.96	51.99	68.78
1290	23.15	44.79	14.91	53.04	68.42
1240	25.29	44.63	14.51	55.42	68.72
1200	27.12	44.51	14.30	57.33	68.80
Average					68.50
					± 0.44

$$-fef(g) = [- (F_T^{\circ} - H_{298}^{\circ})/T]_g$$

$$-fef(l) = [- (F_T^{\circ} - H_{298}^{\circ})/T]_l$$

TABLE 10

HEAT OF SUBLIMATION OF GOLD FROM RATE OF EFFUSION

T	$\Delta F^{\circ}/T$	-fef(g)	-fef(l)	$\Delta H_{298}^{\circ}/T$	ΔH_{298}°
$^{\circ}\text{K}$		cal deg ⁻¹	mole ⁻¹		kcal mole ⁻¹
1673	22.43	47.62	17.57	52.48	87.80
1652	22.99	47.56	17.46	53.09	87.70
1625	24.00	47.50	17.35	54.15	88.01
1597	24.96	47.42	17.23	55.15	88.06
1585	25.33	47.39	17.17	55.55	88.04
1569	25.79	47.35	14.10	56.06	87.96
1563	26.25	47.34	17.08	56.51	88.35
1548	26.84	47.30	17.01	57.13	88.44
1533	27.59	47.25	16.91	57.93	<u>88.81</u>
Average					88.13
					± 0.27

$$-\text{fef}(\text{g}) = [-(F_T^{\circ} - H_{298}^{\circ})/T]_{\text{g}}$$

$$-\text{fef}(\text{l}) = [-(F_T^{\circ} - H_{298}^{\circ})/T]_{\text{l}}$$

\underline{P} vs. $1/T$ plot is appreciably greater than that of the data selected by Hultgren²⁶; furthermore, the calculated heats of sublimation (Table 10) exhibit a definite, though slight, trend with temperature. The average value for the heat of sublimation of gold is 88.1 ± 0.3 kcal/mole which is to be compared with 87.3 selected by Hultgren²⁶, 87.7 by Nesmeyanov³², and 88.3 determined by Hildenbrand and Hall²³.

It would appear from the above results that the microbalance - inverted Knudsen effusion technique (i.e., without recoil force measurement) is capable of providing high temperature vapor pressure data which are at least as reliable as those determined by any other technique. One might also note the wide pressure range (3×10^{-7} to 2×10^{-4} atm) which may be investigated with a single Miker cell (Table 6).

12. Molecular Weights from Recoil Force and Rate of Effusion Data.

The capability of the Miker technique to produce valid values for the molecular weight of vapor effusing from a cell has been examined by obtaining both rate of effusion and recoil force data for tin and calcium fluoride. The data are summarized in Tables 11 and 12 wherein: the recoil mass \underline{m} is the uncorrected experimental value (equation 7); \underline{P}_R is calculated directly from \underline{m} (equation 7 with \underline{m}_c assumed to be zero); \underline{P}_K is calculated with equation (1) with $\underline{M}_K(\text{Sn}) = 118.7$ and $\underline{M}_K(\text{CaF}_2) = 78.1$; $\underline{M}_K^*(\text{uncorrected})$ is obtained with equation (4); and $\underline{M}_K^*(\text{corrected})$ is obtained from equation (41) in which \underline{k}_r has the value $1.04 \times 10^{-12} \text{ deg}^{-3} \text{ sec}^{-1}$ (see subsection 10 above). The uncertainty given for the average value of \underline{M}_K^* is the average deviation.

The values obtained for \underline{P}_R are consistently lower than those for \underline{P}_K , which is to be expected from the omission of the cooling correction \underline{m}_c in calculating \underline{P}_R . This correction \underline{m}_c (equation 38) is typically one-third to one-half as large as the measured recoil mass \underline{m} , and therefore the corrected value of \underline{P}_R is 1.3 - 1.5 times that given in Tables 11 and 12.

The magnitude of \underline{m}_c in comparison with \underline{m} appears to be the major difficulty in the Miker technique. Calculations of \underline{m}_c may be made with considerable precision (subsection D) if the actual rate of cooling of

TABLE 11

VAPOR PRESSURE AND RECOIL FORCE DATA FOR TIN

Run	T, °K	Rate of Effusion, \dot{W} , $\mu\text{g}/\text{sec}$	Recoil Mass \bar{m} , μg	Pressure, dynes/cm ²		Molecular Weight \bar{M}	
				P_K	P_R	\bar{M}_K uncorrected	$\bar{M}_K^{\#}$ corrected
2	1504	5.03	191.	12.2	9.41	197	75
3	1393	1.07	36.5	2.49	1.80	226	93
4	1332	1.51	61.3	3.54	3.08	157	120
6	1386	5.60	210.	13.0	10.4	186	147
7	1434	6.26	239.	14.9	11.8	189	125
8	1384	3.26	149.	7.61	7.33	124	97
9	1408	2.88	123.	6.75	6.10	141	66
10	1393	0.94	36.7	2.18	1.83	172	70
11	1393	0.98	31.8	2.28	1.65	226	85
12	1418	1.32	44.8	3.10	2.21	234	77
13	1418	1.54	49.7	3.62	2.44	261	89
14	1418	1.58	51.1	3.72	2.52	259	90
15	1418	1.75	60.0	4.12	2.96	230	90
16	1466	10.1	377.	23.6	18.5	199	124
17	1456	9.90	350.	23.6	18.2	200	137
18	1334	0.58	21.1	1.32	1.04	192	95
19	1334	0.63	20.2	1.44	0.995	249	114
20	1334	0.70	23.8	1.60	1.17	223	113
Average						100	±20

[#] Recoil mass \bar{m} , is the mass which, under the acceleration of gravity, counterbalances the recoil force acting on the cell.

* See first paragraph of subsection VI. C. 12.

TABLE 12

VAPOR PRESSURE AND RECOIL FORCE DATA FOR CALCIUM FLUORIDE

Run	T, °K	Rate of Effusion, \dot{W} , $\mu\text{g}/\text{sec}$	Recoil Mass \ddagger , m , μg	Pressure, dynes/cm ²		Molecular Weight \ddagger	
				P_K	P_R	M_K^* uncorrected	M_N^* corrected
1	1605	4.07	241.	20.7	20.7	78	56.9
3	1568	1.75	102.	8.83	8.75	80	55.4
4	1577	2.00	111.	10.1	9.52	88	58.4
8	1676	8.06	455.	42.0	39.0	91	57.0
9	1646	6.27	327.	32.3	28.0	104	66.7
10	1631	3.02	156.	15.5	13.4	104	55.5
11	1682	9.95	528.	51.9	45.3	102	64.5
12	1584	2.23	115.	11.3	9.86	101	65.0
13	1581	1.86	90.	9.35	7.72	114	66.6
14	1521	0.75	36.	3.75	3.09	115	70.6
15	1650	3.63	184.	18.8	15.8	111	54.8
16	1707	12.5	685.	65.6	58.7	98	60.0
35	1579	1.40	66.3	7.01	5.69	119	61.2
36	1571	1.08	49.0	5.42	4.20	130	60.7
37	1570	1.07	54.8	5.36	4.70	101	53.4
38	1611	2.76	132.	13.9	11.3	118	64.3
39	1626	2.76	143.	14.2	12.3	104	54.9
40	1610	2.44	118.	12.5	10.1	119	62.5
41	1618	2.42	125.	12.3	10.7	103	54.5
42	1619	2.42	114.	12.3	9.78	121	59.9
Average						60.4	±4.1

the cell is known with appropriate precision and if the assumption of equilibrium between vapor and solid during cooling is valid.

It may well be noted, however, that in spite of these current difficulties in precise determination of recoil force, the present agreement between vapor pressures calculated from rate of effusion data and from recoil force data is at least as good as that typically found between values obtained in different laboratories by workers using effusion techniques.

The distribution of molecular weight values \bar{M}_K^* for both tin (Table 11) and calcium fluoride (Table 12) are rather similar to distributions obtained for various substances with the torsion-effusion technique^{36,37} i.e., the average deviation is large and the average value of \bar{M}_K^* is impossibly low; similar discrepancies in the torsion-effusion technique are also not well understood. From Tables 11 and 12 it is obvious that the Miker technique provides molecular weight data which are not entirely unreasonable. Whether various refinements can improve the technique to the point of providing reliable data remains to be determined.

D. RATE OF EFFUSION FROM A COOLING KNUDSEN CELL

1. Introduction. The difficulties which arise in the Miker technique as a result of effusion while the cell is cooling were discussed in subsection VI. A. 2. There it was also noted that one possible resolution of the difficulties is the accurate and precise evaluation of the mass of vapor which effuses from the Miker cell while the cell cools. In this subsection we report the approach we have taken toward achieving this evaluation.

2. General Equations: In the usual Knudsen effusion equation which we write in differential form,

$$dw = aW(M/2\pi R)^{1/2} P T^{-1/2} dt, \quad (14)$$

dw is the mass of vapor (molecular weight M) which effuses in time dt from a Knudsen cell which has an orifice with area a and transmission probability W , and in which the vapor is at pressure P and temperature T . While the cell is cooling, the temperature T is, of course, a function of

the time: $\underline{T} = \underline{g}(\underline{t})$; conversely, this relation may be expressed by $\underline{t} = \underline{f}(\underline{T})$, from which

$$dt = f'(T)dT. \quad (1)$$

If we assume that equilibrium between vapor and condensed phase is maintained during cooling, the vapor/dissociation pressure \underline{P} is conveniently related to the temperature by the integrated Clausius-Clapeyron equation, $\ln \underline{P} = \underline{C} - (\underline{B}/\underline{T})$, which we write in exponential form

$$\underline{P} = \underline{A}e^{-\underline{B}/\underline{T}}. \quad (2)$$

Substituting equations (15) and (16) into (14), we obtain

$$d\underline{w} = \underline{a}W(\underline{H}/2\pi R)^{\frac{1}{2}}\underline{A}e^{-\underline{B}/\underline{T}}\underline{T}^{-\frac{3}{2}}f'(T)dT. \quad (3)$$

Unfortunately, a simple, general expression for $\underline{f}'(\underline{T})$ is not available; the rate of cooling of an effusion cell depends upon many configurations and environmental factors which vary widely among various furnaces. However, in a vacuum furnace, cooling occurs through conduction and/or radiation; we shall consider the two mechanisms separately.

3. Cooling by Conduction. First, then, we assume that cooling occurs by conduction only and that Newton's "law of cooling" is obeyed, i.e., that

$$\underline{T} - \underline{T}_f = (\underline{T}_i - \underline{T}_f)e^{-\underline{k}_c \underline{t}}, \quad (4)$$

in which \underline{T}_i and \underline{T}_f are the initial and final temperatures, time \underline{t} is measured from the initiation of cooling from \underline{T}_i , and \underline{k}_c is to be evaluated from a plot of $\ln(\underline{T} - \underline{T}_f)$ vs. \underline{t} . Differentiation of equation (18) yields $dt = -dT/k_c(T - T_f)$, which is combined with equation (15) and the result substituted into equation (17) to obtain

$$\Delta \underline{w} = -(aWA/k_c)(M/2\pi R)^{\frac{1}{2}} \int_{\underline{T}_i}^{\underline{T}_f} \underline{T}^{-\frac{3}{2}}(\underline{T} - \underline{T}_f)^{-1} e^{-\underline{B}/\underline{T}} dT, \quad (5)$$

in which $\Delta \underline{w}$ is the mass of vapor which effuses from a cell while the cell cools from \underline{T}_i to \underline{T}_f at a rate described by equation (18). With the transformation $\underline{B}/\underline{T} = \underline{u}^2/2$ and the substitution $\underline{Q} = aWA(M/2\pi R)^{\frac{1}{2}}$, equation (19) becomes

$$\Delta \underline{w} = (2/\pi)^{\frac{1}{2}}(Q/k_c) \int_{\underline{u}_i}^{\underline{u}_f} (1 - \underline{u}_f^{-2}\underline{u}^2)^{-1} e^{-\underline{u}^2/2} d\underline{u} \quad (6)$$

or, if $(1 - \underline{u}_f^{-2}\underline{u}^2)^{-1}$ is replaced by the equivalent series,

$$\Delta \underline{w} = (2/\pi)^{\frac{1}{2}}(Q/k_c) \int_{\underline{u}_i}^{\underline{u}_f} [1 + \underline{u}_f^{-2}\underline{u}^2 + \underline{u}_f^{-4}\underline{u}^4 + \dots] e^{-\underline{u}^2/2} d\underline{u}. \quad (7)$$

Upon multiplying the exponential term through the series, we find that the first term to be integrated is just the integrand of the normal probability function³⁰

$$\varphi(u) = \int_u^\infty e^{-u^2/2} du; \quad (22)$$

hence, we may write

$$\int_{u_i}^{u_f} e^{-u^2/2} du = \varphi(u_i) - \varphi(u_f) \equiv \Delta\varphi. \quad (23)$$

We also note that each term after the first has the form $\int u^{2n} e^{-u^2/2} du$, $n = 1, 2, 3, \dots$, which can for every n be integrated by parts to obtain a function of u plus the next lower member of the series, $\int u^{2(n-1)} e^{-u^2/2} du$; the general solution is, with $\beta \equiv (2n)!/2^n(n!)$, $\gamma_j \equiv 2^{(j+1)/2} [(j+1)/2]!/(j+1)!$, and $j = 1, 3, 5, \dots$,

$$\int_{u_i}^{u_f} u^{2n} e^{-u^2/2} du = \beta \Delta\varphi - [e^{-u^2/2} \sum_{j=1}^{2n-1} \beta \gamma_j u^j]_{u_i}^{u_f}. \quad (24)$$

The solution for equation (21) then is, with $j = \text{odd only}$,

$$\Delta w = (2/\pi)^{1/2} (Q/k_c) \left\{ \Delta\varphi + \sum_{n=1}^{\infty} u_f^{-2n} \left(\beta \Delta\varphi - [e^{-u^2/2} \sum_{j=1}^{2n-1} \beta \gamma_j u^j]_{u_i}^{u_f} \right) \right\}. \quad (25)$$

In order to determine which, if any, terms in equation (25) may be negligible in a typical case we now find the range of typical values of u_i and u_f . From the original transformation we have $u = \sqrt{2B/T}$, and from equation (16) it follows that $B = \Delta H_v/R$; the enthalpy of vaporization/sublimation ΔH_v is assumed to be constant. If ΔH_v and R are expressed in cal mole⁻¹ and cal deg⁻¹ mole⁻¹, respectively, we may write $u \approx \sqrt{\Delta H_v/T}$; this approximation (the value of u is too high by 0.3%) is more precise than is the usual knowledge of ΔH_v and T for high temperature systems. We assume that $1000 \leq T_i \leq 3000^\circ\text{K}$ and that $T_f \approx 300^\circ\text{K}$. Systems typically studied by effusion techniques at 1000-3000^oK have enthalpies of vaporization/sublimation in the range 20-200 kcal/mole; those with higher values must necessarily be studied at higher temperatures, i.e., at larger T_i . Hence, values of u_i seldom fall outside the range $4 \leq u_i \leq 10$, the corresponding range of u_f is $8 \leq u_f \leq 26$, and $1.7 \leq u_f/u_i \leq 3.2$.

Using tabulated values³⁰ for $\varphi(u)$ and $e^{-u^2/2}$, we find that for $u_f/u_i > 1.7$, $\varphi(u_f)/\varphi(u_i) < 10^{-6}$; hence, $\Delta\varphi$ may be replaced by $\varphi(u_i)$ with error less than 1 ppm. With $u_f > 8$, the term $u_f^{-2n} \beta \Delta\varphi$ ($\approx u_f^{-2n} \beta \varphi(u_i)$) is negligible in comparison with $\varphi(u_i)$ for $n > 2$. We note that $e^{-u_f^2/2}$ is

of the same order of magnitude as $\varphi(u_f)$, and that when the summation over j with $\underline{u} = \underline{u}_f$ is multiplied by \underline{u}_f^{-2n} , the result is less than one; consequently, the entire series resulting from substitution of the upper limit of integration \underline{u}_f in equation (25) may be neglected in comparison with $\Delta\varphi \approx \varphi(\underline{u}_i)$. In the series resulting from substitution of the lower limit \underline{u}_i , the largest term for each value of \underline{n} is $\underline{u}_f^{-1}(\underline{u}_i/\underline{u}_f)^{2n-1}e^{-\underline{u}_i^2/2}$; if $\underline{u}_f/\underline{u}_i > 1.7$, this quantity becomes negligible ($< 0.1\%$) in comparison to $\varphi(\underline{u}_i)$ for $\underline{n} > 5$.

With the foregoing approximations and the definitions³⁰

$$\Phi(v) = (2/\pi)^{1/2}\varphi(v), \text{ and } \theta(v) = (2\pi)^{-1/2}e^{-v^2/2}, \quad (26)$$

equation (25) may now be written as

$$\Delta w = (Q/k_c)\{\Phi(\underline{u}_i)[1 + \underline{u}_f^{-2} + 3\underline{u}_f^{-4}] + 2\theta(\underline{u}_i) \sum_{n=1}^5 \underline{u}_f^{-2n} \sum_{j=1}^{2n-1} \beta_{\gamma_j} \underline{u}_i^j\}; j = 1, 3, 5, \dots \quad (27)$$

One final approximation may be noted: if $\underline{u}_f \gg \underline{u}_i$, the terms in \underline{u}_f in equation (27) make very small contribution to Δw and in the limit $\underline{u}_f \rightarrow \infty$, i.e., $\underline{T}_f \rightarrow 0$, equation (27) reduces to

$$\Delta w = (Q/k_c) \Phi(\underline{u}_i), \quad (28)$$

which could have been obtained directly from equations (19) and (20) with $\underline{T}_f = 0$ and $\underline{u}_f = \infty$. Experimentally, the approximation $\underline{T}_f = 0$ is equivalent to assuming that over the temperature range in which effusion during cooling is significant, i.e., over \underline{T}_i to $\underline{T}_i - (400 \pm 100)$, the rate of cooling would be the same for $\underline{T}_f = 0$ as it is for the actual value of \underline{T}_f ; this is not an unreasonable assumption if $\underline{T}_i \gg \underline{T}_f$.

4. Cooling by Radiation. We now assume that cooling occurs by radiation only and that the cooling rate is determined by the familiar \underline{T}^4 relation:

$$dT/dt = -k_r(T^4 - T_f^4). \quad (29)$$

Integration of equation (29) produces

$$k_r t + c = (3T^3)^{-1}[1 + (3/7)(T_f/T)^4 + (3/11)(T_f/T)^8 + \dots]. \quad (30)$$

For high temperature work ($T > 1000$, $T_f \approx 300^\circ\text{K}$) an adequate approximation is $k_r t + c = (3T^3)^{-1}$, and k_r may be evaluated from a plot of $(3T^3)^{-1}$ vs. t (c is an integration constant). From equations (29) and

(15) it follows that $f'(T) = -1/k_r (T^4 - T_f^4)$ which is substituted into equation (17) to obtain

$$\Delta w_r = -(sWA/k_r) (M/2\pi R)^{1/2} \int_{T_i}^{T_f} [1 - (T_f/T)^4]^{-1} T^{-9/2} e^{-B/T} dT.$$

Using the transformation and substitution which preceded equation (20), we obtain

$$\Delta w_r = (2/\pi)^{1/2} (Q/8B^3 k_r) \int_{u_i}^{u_f} (1 + u_f^{-8} u^8 + u_f^{-16} u^{16} + \dots) u^6 e^{-u^2/2} du. \quad (31)$$

If again T_f is assumed to be $\sim 300^\circ K$, terms in the series above $\frac{u_f^{-8} u^8}{u_i^{-8} u^8} = (T_f/T)^4$ make negligible contribution ($< 0.1\%$) for $T > 700^\circ K$; the term $\frac{u_f^{-8} u^8}{u_i^{-8} u^8} = (T_f/T)^4$ contributes less than 1 per cent for $T > 950^\circ K$ and less than 0.1 per cent for $T > 1700^\circ K$. For the moment we assume $\frac{u_f^{-8} u^8}{u_i^{-8} u^8}$ and higher terms to be negligible; if they were not, the appropriate integrals, e.g., of $\frac{u_f^{-8} u^{14}}{u_i^{-8} u^8} e^{-u^2/2} du$, can be readily evaluated with equation (24).

With the above approximations equation (31) may be reduced to

$$\Delta w_r = (2/\pi)^{1/2} (Q/8B^3 k_r) \int_{u_i}^{u_f} u^6 e^{-u^2/2} du \quad (32)$$

which may be readily integrated (equation (24) with $n = 3$) to obtain

$$\Delta w_r = (2/\pi)^{1/2} (Q/8B^3 k_r) \{ 15\Delta\varphi - [e^{-u^2/2} (15u + 5u^3 + u^5)]_{u_i}^{u_f} \} \quad (33)$$

We again replace $\Delta\varphi$ with $\varphi(u_i)$, note that for $u_f > 8$ the terms in u_f are negligible, and write

$$\Delta w_r = (Q/8B^3 k_r) \{ 15\frac{1}{2}(u_i) + 2\theta(u_i) [15u_i + 5u_i^3 + u_i^5] \}. \quad (34)$$

If we note that $15\frac{1}{2}(u_i)/2\theta(u_i) \cong 2$, it immediately follows that for $u_i > 5$ the $\frac{1}{2}(u_i)$ term contributes less than 0.1% to the value of Δw_r ; for $4 \leq u_i \leq 5$ the contribution is 0.1-0.2%. Hence, the $\frac{1}{2}(u_i)$ term may be omitted and equation (34) becomes

$$\Delta w_r = (Q/8B^3 k_r) \{ 2\theta(u_i) [15u_i + 5u_i^3 + u_i^5] \}. \quad (35)$$

If the second term $(\frac{u_f^{-8} u^8}{u_i^{-8} u^8})$ in equation (31) is evaluated via equation (24), one finds that only the terms in u_i with $j = 13$ and 11 make significant contribution to Δw_r . These two terms may be incorporated into the bracketed expressions of equations (34) and (35) to obtain, respectively,

$$\Delta w_r = (Q/8B^3 k_r) \{ 15\frac{1}{2}(u_i) + 2\theta(u_i) [15u_i + 5u_i^3 + u_i^5 + u_f^{-8} (13u_i^{11} + u_i^{13})] \} \quad (36)$$

and

$$\Delta w_r = (Q/8B^3 k_r) \{ 2\theta(u_i) [15u_i + 5u_i^3 + u_i^5 + u_f^{-8} (13u_i^{11} + u_i^{13})] \}. \quad (37)$$

The validity of these approximations has been checked by comparing computed values of the bracketed expressions in equations (34-37) with $(2/\pi)^{1/2}$ times the value of the integral in equations (31 and 32); the value of the integral was obtained with 6-7-figure accuracy on a digital computer. Typical values of u_f (15.433) and u_i (7.1700) from our Miker measurements for tin were used. The results were:

Computed value for integral in equation (22)	0.114504×10^{-6}
Bracketed expression, equation (34)	0.114506
Bracketed expression, equation (35)	0.114495
Computed value for integral in equation (31)	0.114801
Bracketed expression, equation (36)	0.114788
Bracketed expression, equation (37)	0.114777

One further approximation in computing Δw_r might be noted. We have not yet checked this rigorously, but the logarithm of the bracketed expressions in equations (34-37) appears to be a very-nearly-linear function of $1/T$. If Q and k_r are constant from experiment-to experiment, $\log \Delta w_r$ is also a linear function of $1/T$. Therefore, a few appropriately spaced values of Δw_r can be computed via equations (34-37), and additional values obtained by interpolation from a plot of $\log \Delta w_r$ vs. $1/T$.

5. Application to Recoil Force Data. The quantity Δw in the above equations corresponds precisely to the quantity m_c of equation (7) and Figure 14, and may be substituted directly for m_c . We first simplify the notation: $I(u)$ represents the bracketed expressions in equations (34-37) and $K M_K^{*1/2} = (Q/8B^3 k_r)$, i.e., $M_K^{*1/2}$ is removed from Q and K represents the remainder of the coefficient of the bracketed expressions; now we may write

$$m_c = K M_K^{*1/2} I(u) \quad (38)$$

and substitute into equation (7) to obtain

$$P_R = 2g[m + K I(u) M_K^{*1/2}] / af. \quad (39)$$

Equation (39) is then combined with equations (3) and (4) to obtain, respectively,

$$M_K^* + m_K^{*\frac{1}{2}}/KI(u) - \omega f(2\pi RT)^{\frac{1}{2}}/2gWKI(u) = 0 \quad (40)$$

and

$$M_K^* + m_K^{*\frac{1}{2}}/KI(u) - afP_K M_K^{\frac{1}{2}}/2gKI(u) = 0, \quad (41)$$

which are quadratics in $M_K^{*\frac{1}{2}}$ and may be solved for $M_K^{*\frac{1}{2}}$ directly.

TABLE 13

IDENTIFICATION OF MAJOR COMMERCIAL COMPONENTS OF APPARATUS

<u>Item</u>	<u>Supplier</u>
Amplifier, Lock-in PAR JB-5	Princeton Applied Research Corp. Hightstown Rd. Princeton Junction, New Jersey
Amplifier, Magnetic No. 10910	Leeds & Northrup Company 4901 Stenton Avenue Philadelphia 44, Penna.
Cathode, tungsten, impregnated Type B	Philips Metalonics 888 S. Columbus Avenue Yonkers, New York
Condulet connectors, Type CGB	Crouse-Hinds Company Syracuse 1, New York
Control, Recorder Type 1491	Cahn Instrument Company 14511 Paramount Blvd. Paramount, California
Controller, C.A.T. Type 10877	Leeds & Northrup Company 4901 Stenton Avenue Philadelphia 44, Penna.
Couplings, vacuum, Cenco	Central Scientific 1700 Irving Park Rd. Chicago 13, Illinois
Gauge, vacuum, thermocouple Type DV-6M	Hastings-Raydist, Incorporated Hampton, Virginia
Graphite Type AUC	National Carbon Company 270 Park Avenue New York, New York 10017
Heater, tungsten, insulated 6-loop, No. XC1700CL	Electronic Tube Coil Company 557 Eagle Rock Avenue Roseland, New Jersey
Magnet, rod, cunife	Permag Corporation 88-06 Van Wyck Expressway Jamaica 18, New York
Null detector, d.c. Type 9834-2	Leeds & Northrup Company 4901 Stenton Avenue Philadelphia 44, Penna.

<u>Item</u>	<u>Supplier</u>
Octoil pump fluid	Consolidated Vacuum Corporation 1775 Mt. Read Blvd. Rochester 3, New York
Photopot	Giannini Controls Corporation Transducer Division 55 N. Vernon Avenue Pasadena, California
Pivots, diamond and sapphire cups	Moser Jewel Company 544 Fayette Street Perth Amboy, New Jersey
Pressure Meter, Equibar Type 120	Trans-Sonics, Incorporated P. O. Box 328 Lexington 73, Massachusetts
Pressure regulator Type 10	Lexington Controls, Incorporated P. O. Box 132 Burlington, Massachusetts
Pump, diffusion, oil, 4 in., PMC-720	Consolidated Vacuum Corporation 1775 Mt. Read Blvd. Rochester 3, New York
4 in., MCF-300	Consolidated Vacuum Corporation 1775 Mt. Read Blvd. Rochester 3, New York
4 in., MB-100	Consolidated Vacuum Corporation 1775 Mt. Read Blvd. Rochester 3, New York
2 in., PMC-100	Consolidated Vacuum Corporation 1775 Mt. Read Blvd. Rochester 3, New York
Pump, vacuum, mechanical Type 1402-B Duo-Seal	Welch Scientific Company 1515 Sedgwick Street Chicago 10, Illinois
Pyrometer, optical Model 8622-C	Leeds & Northrup Company 4901 Stenton Avenue Philadelphia 44, Penna.
Recorder, potentiometric Model MR	E. H. Sargent & Company 5919 Peeler Street Dallas 35, Texas

<u>Item</u>	<u>Supplier</u>
Recorder, potentiometric Brown 10-MV	Minneapolis-Honeywell Regulator Co. Industrial Division Philadelphia, Penna.
Valve, vacuum, variable leak Cat. No. 9101-M	Granville-Phillips Company 5675 E. Arapahoe Avenue Boulder, Colorado 80301

REFERENCES

1. Aberth, W., Rev. Sci. Instr. 34, 928 (1963).
2. Adams, J. Q., Ph.D. Thesis, University of Illinois (1961).
3. Bader, M., Ph.D. Thesis, Indiana University (1961).
4. Barrer, R. M., "Diffusion in and Through Solids," Cambridge University Press, Cambridge, England (1941).
5. Bennett, J. E., M.S. Thesis, Oklahoma State University, Stillwater (1962).
6. Blakelock, H. D., and Machin, C. F., Engineer 196, 83 (1953).
7. Blue, G. D., et.al., J. Phys. Chem. 67, 877 (1963).
8. Cahn, L., and Shultz, H. R., In "Vacuum Microbalance Techniques," Vol. 2 (R. F. Walker, Ed.) Plenum Press, New York (1962).
9. Cochran, C. N., In "Vacuum Microbalance Techniques," Vol. 1, (M. J. Katz, ed.) Plenum Press, New York (1961).
10. Coenraads, C. N., and Laveille, J. E., Rev. Sci. Instr. 33, 879 (1962).
11. Edwards, J. G., Ph.D. Thesis, Oklahoma State University, Stillwater (1964). Available through University Microfilms.
12. Edwards, R. K., and Downing, J. H., J. Phys. Chem. 59, 1079 (1955).
13. Fite, W. L., and Brackman, R. T., Physical Review 112, 1141 (1958).
14. Freeman, R. D., "Molecular Flow and the Effusion Process in the Measurement of Vapor Pressures", Technical Report ASD-TDR-63-754, Part I, under Contract AF 33(657)-8767 between Oklahoma State University and Aeronautical Systems Division, AFSC, USAF, Wright-Patterson Air Force Base, Ohio (1963).
15. Freeman, R. D., and Searcy, A. W., J. Chem. Phys. 22, 762, 1137 (1954).
16. Freeman, R. D., and Edwards, J. G., In "The Characterization of High Temperature Vapors", (J. L. Margrave, Ed.) to be published.
17. Gerritsen, A. N., and Damon, D. H., Rev. Sci. Instr. 33, 301 (1962).
18. Gilles, P. W., Cater, E. D., and Plante, E. R., J. Chem. Phys. 32, 1269 (1960).
19. Gulbransen, E. A., In "Surface Studies with the Vacuum Microbalance: High Temperature Reactions," Advances in Catalysis, Vol. V (W. G. Frankenburg, et. al., ed.) Academic Press, New York (1953). pp. 119-175.

20. Gulbransen, E. A., and Andrew, K. F., Vacuum Microbalance Techniques, Vol. 2 (R. F. Walker, Ed.) Plenum Press, New York (1962).
21. Heydman, W. F., M. S. Thesis, Oklahoma State University, Stillwater (1959).
22. Hildenbrand, D. L., Private Communication.
23. Hildenbrand, D. L., and Hall, W. F., J. Phys. Chem. 66, 754 (1962).
24. Honig, J. M., and Czanderna, A. W., Anal. Chem. 29, 1206 (1957).
25. Jost, W., "Diffusion in Solids, Liquids, Gases," Academic Press, New York (1952).
26. Hultgren, Orr, Anderson, and Kelley, "Selected Values of Thermodynamic Properties of Metals and Alloys", John Wiley and Sons, New York (1963).
27. Knudsen, M., "The Kinetic Theory of Gases", Methuen and Company, London (1950).
28. Margrave, J. L., In "Physiochemical Measurements at High Temperatures", (J. O'M. Bockris, J. L. White, and J. D. Mackenzie, editors), Butterworth Scientific Publications, London (1959), Ch. 10.
29. Motzfeldt, K., J. Phys. Chem. 59, 139 (1955).
30. National Bureau of Standards Applied Mathematics Series 23, U. S. Government Printing Office, Washington (1953).
31. National Physical Laboratory, "Balances, Weights, and Precise Laboratory Weighing", Notes on Applied Science No. 7, H. M. Stationery Office, London (1954).
32. Nesmeyanov, An. N., "Vapor Pressures of the Elements", Academic Press, New York (1963).
33. Ramsey, N. F., "Molecular Beams", Oxford University Press (1956).
34. Sandstede, G., and Robens, E., Chemie-Ingenieur Technik. 32, 6, 413 (1960); Translated in "Technical Bulletin No. 12," Brinkman Instruments, Inc., Great Neck, N. Y.
35. Schulz, D. A., and Searcy, A. W., J. Phys. Chem. 67, 103 (1963).
36. Searcy, A. W., and Freeman, R. D., J. Am. Chem. Soc. 76, 5229 (1954); J. Chem. Phys. 23, 88 (1955).
37. Sheer, M. D., J. Phys. Chem. 61, 1184 (1957).

38. Simons, Shierrer, and Ritter, Rev. Sci. Instr. 24, 36 (1953).
39. Stott, V., "Collected Researches," Vol. XXIV, Standards of the National Physical Laboratory, London.
40. Stull, D. R., and Sinke, G. C., "Thermodynamic Properties of the Elements," American Chemical Society Advances in Chemistry Series No. 18, Washington (1956).
41. Walker, R. F., In "Vacuum Microbalance Techniques," Vol. 1 (M. J. Katz, ed.) Plenum Press, New York (1961).